

UNIVERSITÀ
DI PAVIA

Department of Physics “Alessandro Volta”

Master’s Degree Programme in Physical Sciences

Non-Hermitian Photonics and Exceptional Points in Planar Optical Waveguides

Master’s Thesis submitted by:
Serena Maria Palmieri

Supervisor:
Prof. Lucio Claudio Andreani

Academic Year 2025 – 2026

A mio papà

Abstract

Non-Hermitian photonics studies optical systems whose effective dynamics are governed by a non-Hermitian operator, as happens in open systems that exchange energy with their environment. In this context, radiative losses provide a source of non-Hermiticity that gives rise to phenomena absent from closed conservative systems, such as dissipative coupling and exceptional points (EPs), where the eigenvalues are degenerate and the eigenvectors coalesce.

This thesis aims to search for exceptional points in a system of two coupled planar waveguides, which are intentionally asymmetric, with different refractive indices and thicknesses. To model electromagnetic propagation, a code based on the transfer matrix method (TMM) was developed, with a root-searching algorithm that operates on the real frequency axis for guided modes and in the complex plane for leaky modes (quasinormal modes, QNMs).

Chapter 3 analyzes the purely guided regime, where the coherent interaction between the two waveguides is modeled with a Hermitian effective Hamiltonian. The coupling coefficient decays exponentially with the gap thickness, consistent with the evanescent nature of the fields: the fitted decay length, 149.9 ± 0.7 nm, agrees within 1% with the evanescent decay length in the gap.

Chapter 4 extends the analysis to the leaky regime, which requires a non-Hermitian effective Hamiltonian that includes the radiative decay rates and both coherent and dissipative coupling. The transition between strong and weak coupling occurs when the coherent coupling, decreasing with the gap, falls below half the difference of the radiative decay rates. Within the fitted two-mode model, an exceptional point is located at a gap thickness $d^* = 758 \pm 3$ nm, at a wavevector that differs from the reference point by less than 1% of the half-width of the fitted window. It is thus reached by varying two parameters: the gap and the in-plane wavevector. At this point, the discriminant vanishes, the phase rigidity falls below 10^{-3}, and the eigenvalue splitting follows the square-root law expected at a second-order exceptional point.

These results show that two homogeneous dielectric waveguides, without gain, absorption, or periodic patterning, can host a radiation-induced exceptional point.

Contents

1 Introduction **8**
- 1.1 Non-Hermitian Photonics 8
- 1.2 Radiative Losses as a Non-Hermitian Resource 10
- 1.3 Scope and Outline of This Work 11

2 Theoretical Background **13**
- 2.1 Planar Optical Waveguides 13
  - 2.1.1 Maxwell's Equations and Boundary Conditions 14
  - 2.1.2 Wave Equation and Mode Classification (TE and TM) . . 15
  - 2.1.3 Confinement and Dispersion 16
  - 2.1.4 Transition from Guided to Leaky Modes 17
- 2.2 Coupled Mode Theory and Effective Hamiltonian 17
  - 2.2.1 The 2×2 Hamiltonian Formulation 18
  - 2.2.2 Supermodes and Eigenvalue Splitting 19
  - 2.2.3 Anticrossing in the Hermitian Regime 20
- 2.3 Open Systems and Quasinormal Modes (QNMs) 21
  - 2.3.1 Quasinormal Modes 21
  - 2.3.2 Effective Non-Hermitian Hamiltonian 22
- 2.4 Exceptional Points in the Two-Mode Model 24
  - 2.4.1 Non-Hermitian Two-Mode Model 24
  - 2.4.2 Coalescence Condition 25
  - 2.4.3 Strong and Weak Coupling Regimes 25
  - 2.4.4 Exceptional Point in the Present Two-Waveguide System 27
  - 2.4.5 Jordan Block Structure and Transformation Matrix 27

3 Guided Modes in Coupled Waveguides **30**
- 3.1 System Geometry 30
- 3.2 Transfer Matrix Method 31
  - 3.2.1 Transfer Matrix Formulation 31
  - 3.2.2 Modal Condition 33
  - 3.2.3 Root Searching Algorithm 33

3.2.4 TMM Validation 34
3.3 Numerical Results 37
3.3.1 Dispersion Relations 37
3.3.2 Supermode Formation 38
3.3.3 Coherent Coupling and Hamiltonian Fitting 39
3.3.4 Dependence on Gap Thickness 41
3.4 Discussion 45

4 Leaky Modes in Coupled Waveguides 47
4.1 Structure and Method 47
4.1.1 Modified Geometry 47
4.1.2 Complex-Frequency Solver 49
4.2 Non-Hermitian Effective Hamiltonian 49
4.2.1 Parametric Model 49
4.2.2 Model Comparison 51
4.3 Numerical Results 55
4.3.1 Complex Dispersion and Field Profiles 55
4.3.2 Coherent Coupling 57
4.3.3 Dissipative Coupling 59
4.3.4 From Strong to Weak Coupling 62
4.4 Localization of the Exceptional Point 64
4.4.1 Discriminant at the Reference Point 64
4.4.2 q-Dependent Correction 65
4.4.3 Signature of the Degeneracy 69
4.5 Discussion 71

5 Conclusions 73

A EP Condition and Jordan Block Structure 75
A.1 Eigenvalues of the Parametric Hamiltonian 75
A.2 The Exceptional Point Condition 76
A.3 Specialization to the Two-Waveguide System 77
A.4 Verification of the Jordan Block Structure 77

B Implementation of the Numerical Solver 79
B.1 Overview and Structure 79
B.2 Transfer Matrix Construction 80
B.3 Guided Modes: Real Root Search 83
B.4 Leaky Modes: Complex Root Search 84
B.4.1 Complex Newton–Raphson Iteration 85
B.4.2 Initialization and Continuation 86

B.5 Branch Tracking 88
B.6 Hamiltonian Fit and Model Selection 90
B.7 Exceptional Point Search 92
B.8 Numerical Parameters 94

C Fits of the Compared Hamiltonian Models **96**
C.1 Fit Curves at $d = 600$ nm 96

List of Figures

2.1 Schematic representation of a planar dielectric waveguide 14
2.2 Field profiles of the fundamental TE and TM modes 16
2.3 Schematic representation of two coupled planar waveguides separated by a gap d 18
2.4 Phenomenon of eigenvalue anticrossing in a Hermitian coupled system 20
2.5 Physical mechanisms of coherent and dissipative coupling 24
2.6 Eigenvalue evolution across an exceptional point 26

3.1 Asymmetric coupled-waveguide structure 31
3.2 Validation of the TMM solver on a single slab 36
3.3 Dispersion of the coupled waveguides in the guided regime . . . 38
3.4 Supermode field profiles in the guided regime 39
3.5 Hermitian Hamiltonian fit at $d = 200$ nm 41
3.6 Guided dispersion for several gap thicknesses 42
3.7 Hamiltonian fits for different gap thicknesses 43
3.8 Exponential decay of the coherent coupling strength 44

4.1 Refractive-index profile in the leaky regime 48
4.2 Non-Hermitian Hamiltonian fit at $d = 600$ nm 53
4.3 Complex dispersion of the leaky structure 56
4.4 Leaky field profiles 57
4.5 Decay of the coherent coupling in the leaky regime 58
4.6 Comparison of functional forms for the dissipative coupling . . . 60
4.7 Secondary maximum of the dissipative coupling 61
4.8 Gap-dependent evolution of the complex dispersion 63
4.9 Discriminant at the reference wavevector 65
4.10 Two-parameter map of the discriminant 67
4.11 EP condition at the reference wavevector 68
4.12 Phase rigidity across the exceptional point 70

C.1 Fit of the baseline Hamiltonian at $d = 600$ nm 97
C.2 Fit of the $+g_1$ Hamiltonian at $d = 600$ nm 97
C.3 Fit of the $+\alpha$ Hamiltonian at $d = 600$ nm 98
C.4 Fit of the $+q_{\text{ref}}$ Hamiltonian at $d = 600$ nm 98
C.5 Fit of the adopted $+g_1,\ \alpha$ Hamiltonian at $d = 600$ nm 99
C.6 Fit of the $+g_1,\ q_{\text{ref}}$ Hamiltonian at $d = 600$ nm 99
C.7 Fit of the $+\alpha,\ q_{\text{ref}}$ Hamiltonian at $d = 600$ nm 100
C.8 Fit of the full Hamiltonian at $d = 600$ nm 100

List of Tables

3.1 Physical parameters of the coupled-waveguide structure. 30
3.2 Parameters of the reference slab used for validation 35
3.3 Best-fit parameters of the effective Hamiltonian 45

4.1 Physical parameters of the leaky coupled-waveguide structure . 48
4.2 Comparison of Hamiltonian models 52
4.3 Regime-dependent parametrization of the coupling 54
4.4 Fitted couplings at representative separations 62
4.5 Properties of the exceptional point 67

B.1 Numerical parameters of the solver 95

Chapter 1

Introduction

1.1 Non-Hermitian Photonics

Many standard theoretical descriptions begin from closed, conservative systems. A Hamiltonian that conserves energy is Hermitian, its eigenvalues are real, and its eigenvectors can always be chosen orthogonal: this structure underlies the standard description of optical resonators and waveguides, where modes are stationary, orthogonal, and characterized by a real frequency. This description is accurate as long as the system exchanges no energy with its surroundings.

Real optical structures, however, generally exchange energy with their surroundings. A resonator radiates, a waveguide leaks, a material absorbs, and a laser is pumped. For decades, these processes were treated as corrections to an ideal closed problem: losses were quantified through a quality factor and otherwise regarded as an imperfection to be minimized. The perspective changed when open systems were recognized as having their own mathematical structure, described by non-Hermitian effective Hamiltonians with complex eigenvalues. Non-Hermitian photonics treats these open-system effects as part of the physical problem rather than as perturbative corrections [1–3].

A major development in the field came from the observation by Bender and Boettcher [4] that a non-Hermitian Hamiltonian can possess an entirely real spectrum when it is symmetric under combined parity and time reversal and this symmetry is not spontaneously broken. In quantum mechanics, this result raised a question of principle, since Hermiticity had been regarded as a necessary condition for a real spectrum. In optics, it acquired a concrete meaning: within the paraxial approximation, the equation governing beam propagation has the same form as the Schrödinger equation, with the refractive index profile playing the role of the potential. A complex refractive index therefore imple-

ments a complex potential directly, with the real part describing refraction and the imaginary part describing gain or absorption. A structure whose index satisfies $n(-z) = n^*(z)$, that is, a symmetric index profile with an antisymmetric distribution of gain and loss, realizes a $\mathscr{P}\mathscr{T}$-symmetric optical potential [5].

The $\mathscr{P}\mathscr{T}$-symmetry prediction was subsequently confirmed in coupled optical waveguides, first in a passive arrangement [6] and then with gain [7], and the field expanded rapidly. Structures based on this principle have been used to obtain unidirectional invisibility [8], single-mode operation in lasers that would otherwise be multimode [9, 10], and nonreciprocal light transmission in coupled microcavities [11].

A central feature of non-Hermitian systems is the exceptional point, a degeneracy with no Hermitian counterpart. In a Hermitian system, two eigenvalues may coincide while the corresponding eigenvectors remain orthogonal; the degeneracy is a crossing, and the eigenvalues depend analytically on the parameters of the system along any one-parameter path. In a non-Hermitian system, the eigenvectors may coalesce together with the eigenvalues, leaving the matrix defective and non-diagonalizable. This type of degeneracy was identified by Kato in the mathematical theory of linear operators [12] and named an *exceptional point*; its physical consequences were explored much later [13, 14].

At an exceptional point the eigenvalues no longer depend analytically on the parameters. For a second-order degeneracy the two eigenvalues separate as the square root of the distance from the singularity, so that a perturbation ϵ produces a splitting proportional to $\sqrt{\epsilon}$ rather than to ϵ. For sufficiently small perturbations, this square-root dependence produces a larger eigenvalue splitting than a linear response, motivating the proposal of exceptional points as a resource for sensing [15], subsequently demonstrated in coupled microring resonators and in a whispering-gallery microcavity [16, 17]. The same nonanalyticity has a topological counterpart: encircling an exceptional point in parameter space exchanges the two eigenstates, so that the eigenvalues return to their initial values after two loops, while the eigenvectors are restored only up to a sign; four loops are needed to recover them exactly [18]. This property has been used to implement asymmetric mode switching in a waveguide [19] and topological energy transfer in an optomechanical system [20].

Exceptional points have been experimentally observed across a wide range of platforms, from microwave cavities [18] to coupled optical resonators [11, 16, 17] (see Refs. [21, 22] for reviews). A substantial part of this work relies on engineered gain and loss. This approach is powerful, but it carries a cost: gain requires pumping, introduces noise, and constrains the choice of materials. It is therefore worth asking whether the non-Hermiticity required for an exceptional point can instead be supplied by the structure itself.

1.2 Radiative Losses as a Non-Hermitian Resource

Radiative leakage can provide the non-Hermiticity required to describe an open photonic system. An optical mode that radiates into the surrounding space loses energy, its eigenfrequency acquires a negative imaginary part, and the effective Hamiltonian describing the discrete part of the spectrum is no longer Hermitian. Modes of this kind are described by the quasinormal-mode formalism [23, 24], in which the outgoing-wave boundary condition replaces the requirement of square integrability and the eigenfrequencies are complex from the outset.

Radiative losses alone do not produce an exceptional point. Two modes that decay independently give a diagonal non-Hermitian Hamiltonian whose eigenvectors remain orthogonal. In the simplest case of negligible dissipative coupling, an exceptional point requires a coupling between the modes together with phase matching: the coherent coupling g, produced by the overlap of the near fields, must balance half the difference between the radiative decay rates, $\Delta\gamma = (\gamma_1 - \gamma_2)/2$. If the modes also radiate into shared channels, their decay processes interfere and generate an additional, purely imaginary coupling $-i\Gamma_{12}$, which shifts the position of the degeneracy but is not required for it to exist.

A related interference effect gives rise to bound states in the continuum. When the radiation emitted into a shared channel interferes destructively, one of the two modes decouples from the radiation continuum and becomes a bound state in the continuum, a mode that remains confined at a frequency where radiation is allowed [25, 26]. Exceptional points obey a different condition, but the two phenomena can occur in the same structures [27].

Passive implementations of exceptional points have an additional practical advantage. The degeneracy can be approached by varying geometric parameters, or the angle at which the structure is illuminated, rather than by adjusting a pump. Exceptional points have been identified in photonic crystal slabs in precisely this way, where a ring of exceptional points was shown to emerge from a Dirac cone when radiation losses are taken into account [27].

Earlier work on planar optical waveguides introduced non-Hermiticity through engineered gain and loss [28]. More recently, exceptional points have also been experimentally demonstrated in a passive integrated strip-waveguide platform, where grating-mediated coupling through a radiative intermediate mode enables the formation of the degeneracy [29]. The geometry and coupling mechanism of that platform differ from those considered in this thesis: the present work studies two asymmetric homogeneous planar dielectric waveguides coupled across a gap, with the imaginary parts of the eigenfrequencies arising solely from radiation into the claddings.

1.3 Scope and Outline of This Work

This thesis asks whether a pair of coupled planar dielectric waveguides, with no gain and no engineered loss, can be driven to an exceptional point using radiation alone, and what conditions the structure must satisfy for this to happen.

The planar geometry provides a tractable platform for studying the transition from guided to radiative modes. A planar waveguide is the simplest geometry that supports guided modes, and the coupling between two such waveguides is a textbook problem of integrated optics; the physics is therefore well understood in the conservative limit, and departures from this behavior can be attributed to the openness of the system rather than to the complexity of the geometry. The stratified structure also admits a semi-analytical solution through the transfer matrix method, which gives direct access to the complex eigenfrequencies without the discretization and absorbing boundaries required by a full numerical solution. The price of this simplicity is that the structure is one-dimensional, so the results describe the underlying leaky modes rather than a specific device.

For the passive mechanism investigated here, three conditions must be present. The two modes must retain an evanescent overlap across the gap, which sustains the coherent coupling; they must radiate into the claddings, which makes the system open; and they must decay at different rates, which requires the two waveguides to be asymmetric. Identical waveguides have equal decay rates, so the condition $g = \pm\Delta\gamma$ could only be met at $g = 0$. For the first two conditions to coexist, the effective index must lie within a window bounded below by the gap index and above by the cladding index, a range that is not provided by the conventional geometry of a high-index core in a low-index cladding.

The work proceeds in three stages. First, a solver based on the transfer matrix method is developed, with a root-searching algorithm that operates on the real axis for guided modes and in the complex plane for leaky ones. Second, the purely guided regime is analyzed as a baseline, and the coherent coupling is extracted by fitting the numerical dispersion to a Hermitian two-mode Hamiltonian. Finally, the structure is modified so that both coherent and radiative mechanisms are active, and the complex eigenfrequencies are fitted to a non-Hermitian Hamiltonian containing both coherent and dissipative coupling.

The analysis shows that the coherent coupling decays exponentially with the separation, over a length close to the evanescent decay length in the gap. As the gap increases, the coherent coupling falls below half the difference of the two radiative decay rates, and the system crosses from strong to weak coupling. The resulting exceptional point is located in the plane defined by

the gap thickness and the in-plane wavevector.

The thesis is organized as follows. Chapter 2 develops the theoretical framework, including the description of planar waveguides and their guided and leaky modes, the Hermitian coupled-mode picture, the non-Hermitian extension through the quasinormal-mode formalism, and the exceptional point condition together with the associated Jordan-block structure. Chapter 3 presents the transfer matrix solver, its validation, and the analysis of the purely guided regime. Chapter 4 extends the analysis to the leaky regime, separates the two coupling mechanisms, and localizes the exceptional point. Chapter 5 summarizes the results and discusses their limitations. Appendix A derives the exceptional point condition and the Jordan-block structure in full, Appendix B documents the implementation of the solver and Appendix C collects the complete set of fits for the Hamiltonian models compared in Chapter 4.

Chapter 2

Theoretical Background

This chapter develops the theoretical framework used to describe the coupled-waveguide system studied in this thesis. Section 2.1 reviews the closed description of planar dielectric waveguides. Section 2.2 introduces the Hermitian coupled-mode picture that governs their interaction in the guided regime. Sections 2.3–2.4 then extend this description to the non-Hermitian regime, in which radiative losses couple the system to the electromagnetic continuum, culminating in the exceptional point condition and Jordan-block structure of the two-waveguide system studied in this work.

2.1 Planar Optical Waveguides

Dielectric waveguides [30] confine and guide electromagnetic radiation. The physical mechanism underlying light confinement is total internal reflection, which occurs at the interface with a lower-index medium when the angle of incidence exceeds the critical angle. The standard reference geometry is the planar (slab) waveguide, a one-dimensional system that confines the electromagnetic field along a single spatial direction, as shown in Fig. 2.1.

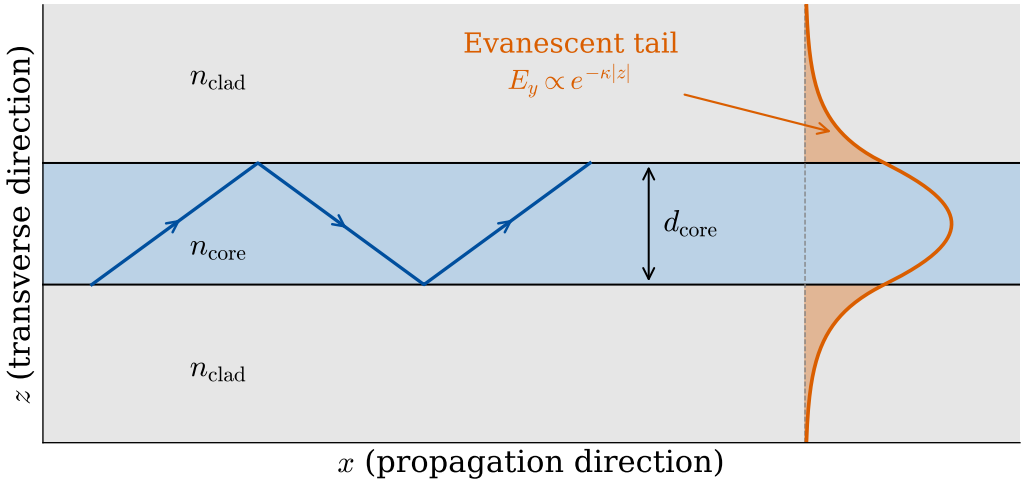


Figure 2.1: Schematic representation of a planar dielectric waveguide stratified along z. The light is confined in the core region (n_{core}) via total internal reflection, while the evanescent tails of the electromagnetic field penetrate into the cladding layers (n_{clad}).

2.1.1 Maxwell's Equations and Boundary Conditions

Electromagnetic propagation in a dielectric structure is governed by the macroscopic Maxwell equations [30]. Assuming a linear, isotropic, non-magnetic ($\mu = \mu_0$, vacuum permeability), non-dispersive, lossless, and source-free medium, the equations in the frequency domain (adopting a harmonic time dependence $e^{-i\omega t}$) take the form:

$$\nabla \times \mathbf{E}(\mathbf{r}) = i\omega\mu_0 \mathbf{H}(\mathbf{r}) \tag{2.1}$$
$$\nabla \times \mathbf{H}(\mathbf{r}) = -i\omega\varepsilon_0\varepsilon_r(\mathbf{r})\mathbf{E}(\mathbf{r}) \tag{2.2}$$
$$\nabla \cdot [\varepsilon_r(\mathbf{r})\mathbf{E}(\mathbf{r})] = 0 \tag{2.3}$$
$$\nabla \cdot \mathbf{H}(\mathbf{r}) = 0 \tag{2.4}$$

where $\mathbf{E}$ and $\mathbf{H}$ are the electric and magnetic field vectors, ω is the angular frequency, and ε_0 denotes the vacuum permittivity. The relative dielectric permittivity is given by $\varepsilon_r(\mathbf{r}) = n^2(\mathbf{r})$, where $n(\mathbf{r})$ is the position-dependent refractive index.

To yield physical solutions, the fields must satisfy boundary conditions at the interfaces between media with different refractive indices. In the absence of free surface charges and currents, the tangential components of $\mathbf{E}$ and $\mathbf{H}$, and the normal components of the electric displacement field $\mathbf{D}$ and magnetic induction field $\mathbf{B}$, are continuous across the interface [31].

2.1.2 Wave Equation and Mode Classification (TE and TM)

Consider a planar waveguide whose refractive index varies exclusively along the z-axis, $n(\mathbf{r}) = n(z)$, and which is invariant in the xy-plane. Selecting the x-axis as the propagation direction, the electric field is expressed as:

$$\mathbf{E}(x,z,t) = \mathbf{E}(z)e^{ik_x x}e^{-i\omega t} \tag{2.5}$$

where k_x represents the propagation constant along the longitudinal x-axis. Translational invariance along the y-axis ($\partial/\partial y = 0$) decouples Maxwell's equations into two independent polarization sets [32]:

Transverse Electric (TE) modes. Characterized by a purely transverse electric field ($E_y \neq 0, E_x = E_z = 0$). Substituting this ansatz into Maxwell's equations yields the scalar wave equation for E_y:

$$\frac{d^2E_y}{dz^2} + \left[k_0^2 n^2(z) - k_x^2\right]E_y = 0 \tag{2.6}$$

where $k_0 = \omega/c = 2\pi/\lambda$ is the vacuum wavenumber, with c being the speed of light in vacuum and λ the vacuum wavelength.

Transverse Magnetic (TM) modes. Characterized by a purely transverse magnetic field ($H_y \neq 0, H_x = H_z = 0$), governed by:

$$n^2(z)\frac{d}{dz}\left[\frac{1}{n^2(z)}\frac{dH_y}{dz}\right] + \left[k_0^2 n^2(z) - k_x^2\right]H_y = 0 \tag{2.7}$$

The corresponding field profiles are shown in Fig. 2.2.

Formulation of the Waveguide Eigenproblem. The waveguide eigenproblem can be formulated in two equivalent ways: by finding the longitudinal propagation constant k_x at fixed real frequency ω, or by finding the eigenfrequencies ω at fixed longitudinal wavevector k_x. While the former is the standard formulation for lossless structures, the latter is adopted throughout the present work. Treating k_x as a fixed real-valued parameter and solving for the eigenfrequencies ω, which naturally extend into the complex plane for open systems, aligns directly with the transfer matrix method through the modal condition $T_{22}(\omega, k_x) = 0$ implemented in Chapter 3 and with the non-Hermitian quasinormal-mode framework.

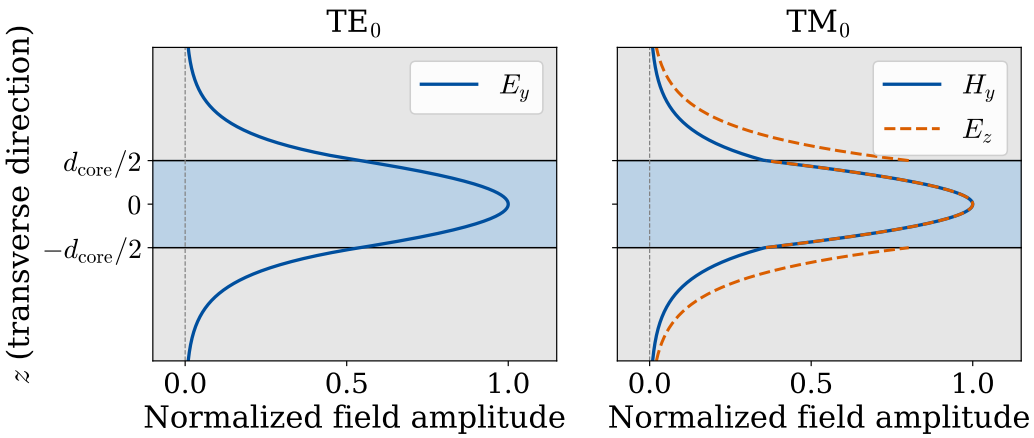


Figure 2.2: Spatial field profiles of the fundamental TE (E_y) and TM (H_y, E_z) modes of a symmetric slab with $n_{\text{core}} = 1.5$ and $n_{\text{clad}} = 1.0$. E_y and H_y are continuous across the interfaces, whereas $E_z \propto H_y/n^2$ jumps by the factor $n^2_{\text{core}}/n^2_{\text{clad}}$. Both modes are computed at the same normalized frequency, $V = (k_0 d_{\text{core}}/2)\sqrt{n^2_{\text{core}} - n^2_{\text{clad}}} = 1.85$.

2.1.3 Confinement and Dispersion

A standard planar waveguide consists of a core layer of thickness d_{core} and refractive index n_{core}, between two semi-infinite claddings with index $n_{\text{clad}} < n_{\text{core}}$. For simplicity, a symmetric structure is considered.

To achieve guidance via total internal reflection, the longitudinal wavenumber k_x must satisfy:

$$k_0 n_{\text{clad}} < k_x < k_0 n_{\text{core}} \tag{2.8}$$

Under this condition, the wave equation for TE modes (Eq. (2.6)) exhibits two distinct spatial behaviors along the transverse direction z:

1. Inside the core ($n(z) = n_{\text{core}}$), the term $k_0^2 n^2_{\text{core}} - k_x^2$ is positive. Setting $k_z^2 = k_0^2 n^2_{\text{core}} - k_x^2$, Eq. (2.6) yields oscillatory harmonic solutions (sines and cosines).

2. Inside the cladding ($n(z) = n_{\text{clad}}$), the term $k_0^2 n^2_{\text{clad}} - k_x^2$ becomes negative. Defining $\kappa^2 = k_x^2 - k_0^2 n^2_{\text{clad}} > 0$, the equation admits exponential solutions $e^{\pm\kappa|z|}$.

To ensure finite energy and prevent spatial divergence at infinity, the decaying exponential solution is selected. Consequently, the field penetrates the lower-index medium as an evanescent wave [32].

The evanescent tails provide the physical mechanism for coherent coupling between neighboring waveguides. When two waveguides are brought close to each other, the overlap of their evanescent fields allows electromagnetic energy to be transferred from one waveguide to the other. This evanescent-field overlap is the basis of the coherent coupling described by coupled-mode theory in the next section [31].

2.1.4 Transition from Guided to Leaky Modes

The guided-mode description breaks down when the field in the cladding becomes propagating rather than evanescent. When $k_x < k_0 n_{\text{clad}}$, i.e. above the cladding light line $\omega = ck_x/n_{\text{clad}}$ in the dispersion diagram, the transverse wavenumber in the cladding becomes real and the mode can couple to the radiation continuum. The mode therefore becomes leaky. The term $k_0^2 n_{\text{clad}}^2 - k_x^2$ becomes positive, rendering k_z in the cladding real-valued

$$k_{z,\text{clad}} = \sqrt{k_0^2 n_{\text{clad}}^2 - k_x^2}. \tag{2.9}$$

As a result, the field in the cladding loses its exponential decay and transforms into an outgoing propagating wave $e^{ik_{z,\text{clad}}|z|}$.

In the leaky regime, energy is no longer strictly confined to the core but is transversely radiated into the cladding along z. The resulting mode is a *leaky* or radiative mode. This outgoing energy flux prevents the confinement of energy within the guiding layer. To satisfy outgoing wave boundary conditions, the problem must be formulated in the complex plane, allowing for complex-valued angular frequencies ω. The resulting radiative openness leads to a non-Hermitian description of the system and provides the physical setting for the quasinormal-mode [23] formulation introduced in the following sections.

2.2 Coupled Mode Theory and Effective Hamiltonian

When two dielectric waveguides are placed in close proximity, the confinement of their respective electromagnetic fields is no longer ideal. The spatial overlap of their evanescent tails in the intermediate cladding induces a coherent interaction between the modes, allowing a periodic energy transfer from one structure to the other [31]. This phenomenon is mathematically formalized by the coupled mode theory (CMT) [30].

2.2.1 The 2×2 Hamiltonian Formulation

Consider a system composed of two planar waveguides, Core 1 and Core 2, separated by a gap distance d, as shown in Fig. 2.3. Let $k_{x,1}$ and $k_{x,2}$ be the propagation constants of the two modes of interest calculated for the isolated waveguides at frequency ω.

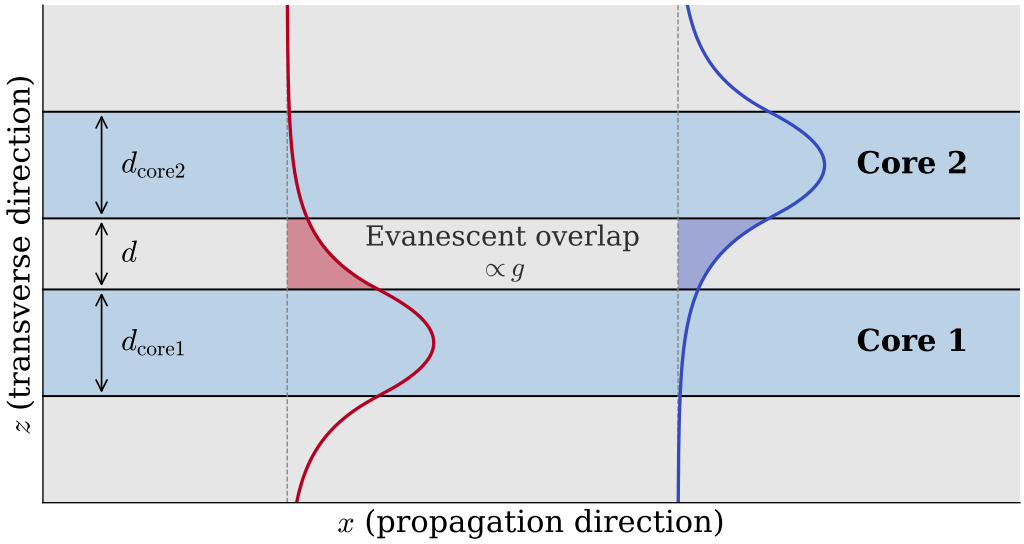


Figure 2.3: Schematic representation of two coupled planar waveguides separated by a gap d. The coherent coupling g is physically mediated by the spatial overlap of the evanescent tails of the two isolated modes within the intermediate cladding region. Red: mode of Core 1; blue: mode of Core 2, with the same colors used for $|\psi_1|^2 = 1$ and 0 in Chapters 3 and 4.

In the absence of radiation to the continuum or material absorption (purely guided regime), the spatial evolution of the complex modal amplitudes $a_1(x)$ and $a_2(x)$ along the propagation direction is governed by a matrix differential equation analogous to the time-dependent Schrödinger equation:

$$-i\frac{d}{dx}\begin{pmatrix} a_1 \\ a_2 \end{pmatrix} = \begin{pmatrix} k_{x,1} & g \\ g^* & k_{x,2} \end{pmatrix}\begin{pmatrix} a_1 \\ a_2 \end{pmatrix} \tag{2.10}$$

The matrix governing the system's evolution is known as the effective Hamiltonian $\mathbf{H}$. The diagonal elements represent the (real) propagation constants of the unperturbed modes, while the off-diagonal terms g and g^* represent the coupling coefficient. In the absence of loss or gain, the effective Hamiltonian is Hermitian ($\mathbf{H} = \mathbf{H}^\dagger$), ensuring real eigenvalues and conservative modal evolution. By appropriately choosing the relative phases of the two isolated modes,

the coupling coefficient can be assumed to be purely real ($g = g^*$), rendering the effective Hamiltonian a real and symmetric matrix.

From a physical perspective, the parameter $|g|$ is proportional to the overlap integral of the evanescent fields of the two waveguides. Since the fields in the cladding exhibit an exponential decay, the coupling strength $|g|$ also decreases exponentially as the separation distance d increases [31].

2.2.2 Supermodes and Eigenvalue Splitting

The diagonalization of the effective Hamiltonian yields the coupled system's eigenvalues, which correspond to the propagation constants $k_{x,\pm}$ of the structure's *supermodes*:

$$k_{x,\pm} = k_{x,\text{avg}} \pm \sqrt{\delta^2 + |g|^2} \tag{2.11}$$

where the average propagation constant $k_{x,\text{avg}} = (k_{x,1} + k_{x,2})/2$ and the detuning parameter $\delta = (k_{x,1} - k_{x,2})/2$ have been introduced. The detuning parameter δ therefore measures the phase mismatch between the two uncoupled modes at the chosen frequency [31].

The behavior of the supermodes is strictly tied to the balance between the phase mismatch δ and the coupling strength g:

Phase-matched case ($\delta = 0$). The two propagation constants coincide, $k_{x,1} = k_{x,2} = k_{x,0}$. This is automatic when the waveguides are geometrically and materially identical, but identity is not required: in an asymmetric structure such as the one studied in this thesis the two dispersion curves have different slopes, and δ vanishes at their crossing, that is, at one particular wavevector. The radical reduces to $|g|$ and the eigenvalues become $k_{x,\pm} = k_{x,0} \pm |g|$. The degeneracy of the original modes is lifted: the system develops a symmetric-like supermode associated with $k_{x,+}$ and an antisymmetric-like supermode associated with $k_{x,-}$. The eigenvalue distance, known as *mode splitting*, is $\Delta k_x = 2|g|$ and directly measures the strength of the coherent coupling.

Detuned case ($\delta \neq 0$). Away from the crossing the term δ^2 becomes progressively larger than $|g|^2$. In the large-detuning regime the eigenvalues approach the propagation constants of the isolated waveguides ($k_{x,+} \approx k_{x,1}$ and $k_{x,-} \approx k_{x,2}$). The supermodes lose their symmetry, and the electromagnetic energy tends to be predominantly confined within one waveguide or the other.

2.2.3 Anticrossing in the Hermitian Regime

A fundamental consequence of Eq. (2.11) is that, as long as the system remains strictly Hermitian (with $|g| > 0$ and real-valued parameters), the term under the square root $\delta^2 + |g|^2$ is strictly positive. Therefore, the two propagation constants $k_{x,+}$ and $k_{x,-}$ can never coincide.

If the geometric parameters of the waveguides are continuously varied to make $k_{x,1}$ and $k_{x,2}$ cross, the eigenvalues of the coupled system do not intersect. Instead, they experience a repulsion known as *anticrossing* (or level repulsion) [30], as illustrated in Fig. 2.4.

For this two-mode model, the simultaneous coalescence of the eigenvalues ($k_{x,+} = k_{x,-}$) and their respective eigenvectors requires the radicand to vanish. This cannot occur in a closed Hermitian system, because the radicand is a sum of non-negative real terms. In an open system, however, the diagonal entries acquire imaginary parts through radiative decay, so the radicand becomes complex and can vanish.

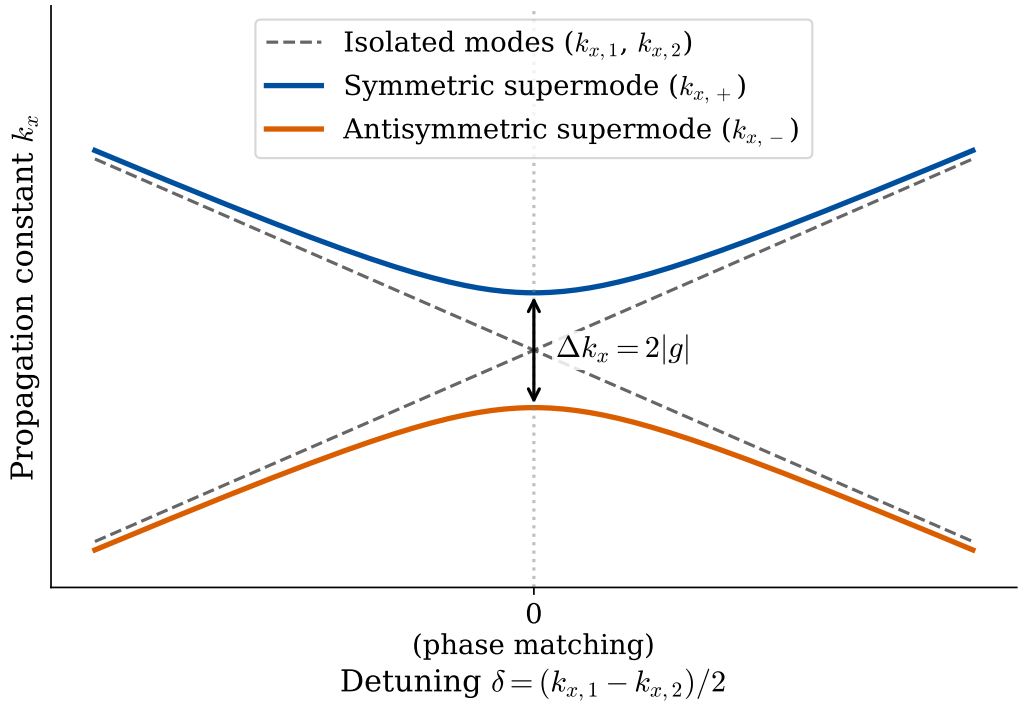


Figure 2.4: Phenomenon of eigenvalue anticrossing in a Hermitian coupled system. The unperturbed propagation constants $k_{x,1}$ and $k_{x,2}$ (dashed lines) cross at $\delta = 0$, whereas the supermodes $k_{x,+}$ and $k_{x,-}$ (solid lines) experience a level repulsion directly proportional to the coupling strength g.

Throughout the rest of this thesis, the same two-mode algebra is applied at fixed k_x, with the eigenfrequencies replacing the propagation constants. The diagonal entries therefore become the uncoupled frequencies $\omega_{1,2}(k_x)$, the detuning becomes $(\omega_1 - \omega_2)/2$, and the coupling g has the dimensions of a frequency. Equation (2.11) and the anticrossing shown in Fig. 2.4 carry over unchanged, with one difference in the labeling: the symmetric-like supermode, which has the larger k_x at fixed ω, has the lower frequency at fixed k_x. This is the formulation used in Eq. (3.10) and, with complex diagonal entries, in Eq. (2.14).

2.3 Open Systems and Quasinormal Modes (QNMs)

The description developed in the previous sections assumes a conservative and effectively closed system, in which radiation losses and material absorption are neglected. However, many practical photonic structures are open: electromagnetic energy is no longer strictly confined to the system and can be radiated into the surrounding environment. Incorporating these open-system phenomena requires a non-Hermitian description.

2.3.1 Quasinormal Modes

When an optical structure couples to an external continuum, the dynamics within its discrete subspace are described by an effective non-Hermitian Hamiltonian $\mathbf{H}\text{eff} \neq \mathbf{H}\text{eff}^{\dagger}$, whose eigenfrequencies are in general complex and whose eigenvectors are non-orthogonal.

In closed conservative systems, electromagnetic resonances are described by real-frequency normal modes that satisfy standard spatial orthogonality and energy conservation relations. In contrast, open radiating systems are properly described by *quasinormal modes* (QNMs) [23].

Under a harmonic time dependence $e^{-i\omega t}$, a QNM represents an eigensolution of Maxwell's equations subject to outgoing-wave boundary conditions at spatial infinity (Sommerfeld radiation condition). As a consequence of radiative dissipation, the eigenfrequency $\tilde{\omega}$ becomes complex-valued:

$$\tilde{\omega}_j = \omega_j - i\gamma_j \tag{2.12}$$

where $\omega_j = \mathrm{Re}(\tilde{\omega}_j)$ denotes the real resonant frequency and $\gamma_j = -\mathrm{Im}(\tilde{\omega}_j) > 0$ represents the radiative decay rate (damping coefficient). Consequently, a modal amplitude evolving as $a_j(t) \propto e^{-i\tilde{\omega}_j t} = e^{-i\omega_j t} e^{-\gamma_j t}$ decays exponentially in time, while the corresponding modal energy decays as $e^{-2\gamma_j t}$.

Because the outgoing wave condition leads to fields that diverge spatially at infinity, the modal energy computed via the standard Hermitian inner product becomes infinite; therefore, QNMs cannot be normalized in a conventional manner. Defining mathematically consistent modal expansions and normalizations requires generalized procedures. These include integral regularization, deformation of the integration contour in the complex plane, or the introduction of complex spatial coordinates through artificial absorbing layers, known as perfectly matched layers, which attenuate the divergent fields and render the integrals finite [23]. In the present work no QNM normalization is required, since the transfer matrix method yields the eigenfrequencies directly from the modal condition $T_{22} = 0$ introduced in Chapter 3.

2.3.2 Effective Non-Hermitian Hamiltonian

The non-Hermitian effective Hamiltonian provides the two-mode description of the leaky-waveguide system at fixed k_x. Unlike the Hermitian coupled-mode description, which is formulated as a spatial evolution problem along x, this formulation uses temporal evolution and the complex QNM frequencies $\tilde{\omega}_j$ as eigenvalues. To model the resonant interaction between two leaky modes in a coupled waveguide system at fixed k_x, we write the temporal evolution of the modal amplitudes $\mathbf{a}(t) = (a_1(t), a_2(t))^T$ as governed by a 2×2 effective non-Hermitian matrix differential equation:

$$i\frac{d}{dt}\mathbf{a}(t) = \mathbf{H}_{\text{eff}}\mathbf{a}(t) \tag{2.13}$$

By defining the complex QNM eigenfrequencies $\tilde{\omega}_1 = \omega_1 - i\gamma_1$ and $\tilde{\omega}_2 = \omega_2 - i\gamma_2$, the effective Hamiltonian takes the explicit form:

$$\mathbf{H}_{\text{eff}} = \begin{pmatrix} \tilde{\omega}_1 & K \\ K & \tilde{\omega}_2 \end{pmatrix} = \begin{pmatrix} \omega_1 - i\gamma_1 & g - i\alpha\sqrt{\gamma_1\gamma_2} \\ g - i\alpha\sqrt{\gamma_1\gamma_2} & \omega_2 - i\gamma_2 \end{pmatrix} \tag{2.14}$$

Here, $K = g - i\alpha\sqrt{\gamma_1\gamma_2}$ represents the total complex coupling coefficient governing the open system.

The complex coupling parameter K combines two distinct interaction mechanisms:

Coherent Coupling (g). Arises from the spatial overlap of near-field evanescent tails within the dielectric structures, driving coherent energy exchange between the waveguides in direct analogy to conservative coupled mode theory.

Dissipative Coupling ($\alpha\sqrt{\gamma_1\gamma_2}$). Arises when the two modes interact with common radiation channels, so that their decay processes are no longer independent. The parameter $\alpha \in [-1, 1]$ measures the interference efficiency within these shared outgoing radiation channels: $\alpha = 0$ corresponds to fully independent decay, while $\alpha = \pm 1$ corresponds to fully correlated decay, with the sign encoding whether the interference is constructive or destructive.

This form of the dissipative coupling follows from the temporal coupled-mode theory of open resonators [33], in which $\alpha\sqrt{\gamma_1\gamma_2}$ is the overlap between the couplings of the two modes to the radiation channels; energy conservation bounds it by $\sqrt{\gamma_1\gamma_2}$, so that $|\alpha| \leq 1$. In the Friedrich–Wintgen mechanism for bound states in the continuum [25], and in closely related recent treatments of coupled leaky photonic resonances [34], the two modes couple to a single shared radiation channel and the dissipative coupling takes its maximal value, $\alpha = \pm 1$. In the present system the two modes radiate into two channels, the two claddings, so that $|\alpha| < 1$ in general; α is therefore retained as a free real parameter and extracted directly from the fit of Section 4.2.

The two mechanisms are sketched in Fig. 2.5. An exceptional point is reached when the coherent coupling balances half the difference of the decay rates, $g = \pm(\gamma_1 - \gamma_2)/2$, while the detuning of the resonance frequencies compensates the dissipative coupling, $(\omega_1 - \omega_2)/2 = \mp\alpha\sqrt{\gamma_1\gamma_2}$, with the signs taken together (Section 2.4). The dissipative coupling shifts the position of the exceptional point but is not required for its existence: Fig. 2.6 is computed with $\alpha = 0$ and $\omega_1 = \omega_2$.

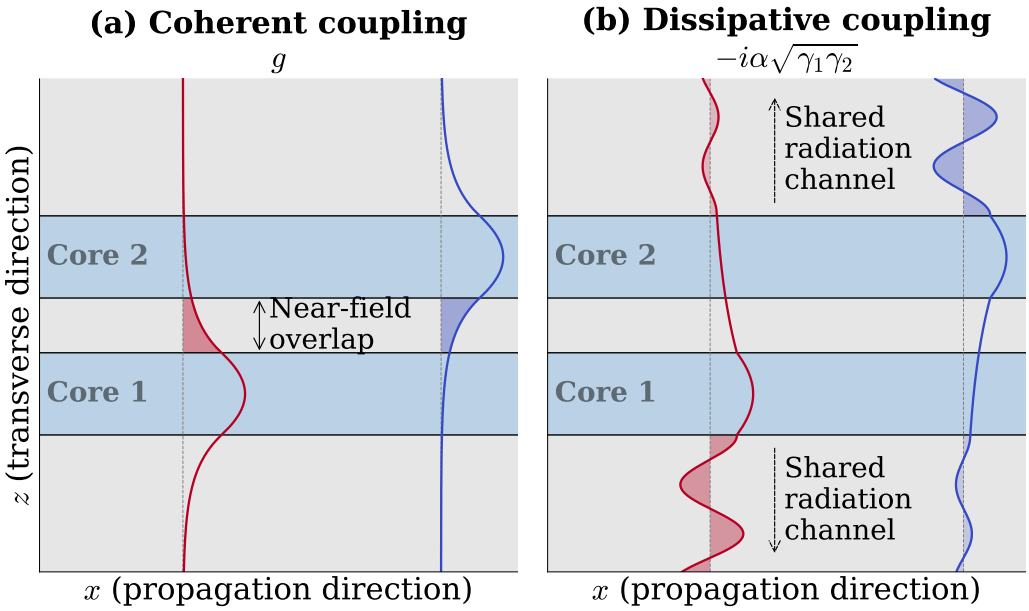


Figure 2.5: Physical mechanisms of mode interaction in an open waveguide system. **(a) Coherent coupling (g)** occurs in the near-field through the direct spatial overlap of the evanescent tails of the two modes. **(b) Dissipative coupling ($-i\alpha\sqrt{\gamma_1\gamma_2}$)** is a far-field effect: each leaky mode is evanescent in the low-index gap and radiates into both claddings, where its field oscillates with an amplitude that grows away from the stack, as for quasinormal modes. The two modes therefore share the same radiation channels, and their decay processes interfere.

2.4 Exceptional Points in the Two-Mode Model

An exceptional point (EP) is fundamentally different from an ordinary Hermitian degeneracy, where eigenvalue crossing leaves the eigenvectors linearly independent. EPs are singular points in the parameter space of non-Hermitian systems, characterized by a non-analytic dependence of the eigenvalues on system parameters.

2.4.1 Non-Hermitian Two-Mode Model

Consider the effective two-mode Hamiltonian introduced in the previous section (Eq. (2.14)). The complex eigenfrequencies of the coupled system are obtained by diagonalizing $\mathbf{H}_{\text{eff}}$:

$$\tilde{\omega}_{\pm} = \bar{\omega} - i\bar{\gamma} \pm \sqrt{\Delta^2 + K^2}, \tag{2.15}$$

where

$$\bar{\omega} = \frac{\omega_1 + \omega_2}{2}, \qquad \bar{\gamma} = \frac{\gamma_1 + \gamma_2}{2}, \tag{2.16}$$

and

$$\Delta = \frac{\omega_1 - \omega_2}{2} - i\frac{\gamma_1 - \gamma_2}{2}, \qquad K = g - i\alpha\sqrt{\gamma_1\gamma_2}. \tag{2.17}$$

The quantity

$$D = \Delta^2 + K^2 \tag{2.18}$$

is the discriminant of the two-mode problem. The eigenvalue separation is therefore

$$\tilde{\omega}_+ - \tilde{\omega}_- = 2\sqrt{D}. \tag{2.19}$$

2.4.2 Coalescence Condition

For the two-mode non-Hermitian Hamiltonian considered here, an EP is reached when the eigenvalues coalesce,

$$\tilde{\omega}_+ = \tilde{\omega}_-, \tag{2.20}$$

which requires

$$D = 0. \tag{2.21}$$

Since D is complex-valued, this condition corresponds to the simultaneous vanishing of its real and imaginary parts:

$$\mathrm{Re}(D) = 0, \qquad \mathrm{Im}(D) = 0. \tag{2.22}$$

At this point, the two eigenvectors also coalesce and the Hamiltonian becomes defective. Consequently, it can no longer be diagonalized by a complete set of eigenvectors. Instead, the matrix can be represented in Jordan form [14], which reflects the reduced dimensionality of the eigenspace at the EP.

Non-Hermiticity therefore makes exceptional degeneracies possible, but does not by itself guarantee their occurrence. The system parameters must satisfy the condition given by Eq. (2.21), and additionally $K \neq 0$: a vanishing D with $K = \Delta = 0$ is a trivial degeneracy, at which the two eigenvectors remain independent.

2.4.3 Strong and Weak Coupling Regimes

In the reference case of phase matching and negligible dissipative coupling, the ratio between the coherent coupling g and the half-difference of the radiative decay rates determines the evolution of the complex eigenfrequencies and distinguishes the strong- and weak-coupling regimes [35], summarized in Fig. 2.6.

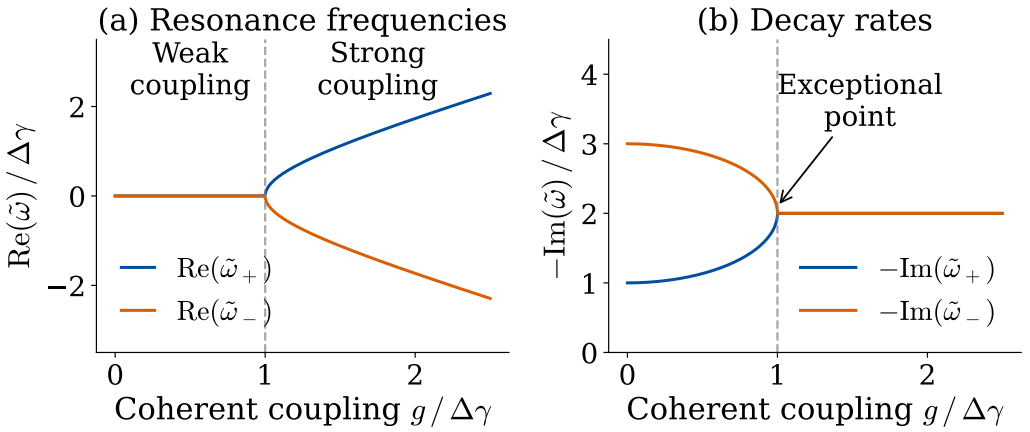


Figure 2.6: Schematic eigenvalue evolution as a function of the coherent coupling g in a representative two-mode model. The curves are computed with $\omega_1 = \omega_2$, $\alpha = 0$, $\gamma_1 = 3\,\Delta\gamma$ and $\gamma_2 = \Delta\gamma$; all quantities are in units of $\Delta\gamma$. **(a)** Real parts of the complex eigenfrequencies (resonance frequencies). **(b)** Imaginary parts (decay rates). The system transitions from a weak-coupling regime, characterized by degenerate real parts and split imaginary parts, to a strong-coupling regime where the real parts split (anticrossing) and the imaginary parts coalesce. The boundary between these regimes is marked by the exceptional point (dashed line).

In the *strong-coupling regime*, the coherent coupling g dominates over the difference in decay rates. The interaction produces a splitting of the real parts of the eigenfrequencies, while the corresponding imaginary parts tend to coalesce. Physically, the two modes are strongly hybridized through their near-field overlap.

In an intermediate *transition regime*, close to the exceptional point, the coherent coupling and the half-difference of the decay rates are comparable, and neither can be neglected.

In the *weak-coupling regime*, the difference in the decay rates dominates over the coherent coupling. The real parts of the eigenfrequencies cross, while the imaginary parts remain split, so that the two modes retain distinct lifetimes.

This classification is particularly relevant to the present system, where the coherent coupling g decreases with increasing gap between the two waveguides, while the difference of the decay rates remains finite. At phase matching and for negligible dissipative coupling, the familiar boundary $|g| = |\gamma_1 - \gamma_2|/2$ separates the strong- and weak-coupling limits. In the general model considered here, however, the transition is governed by the full complex discriminant D, so the simple condition should be regarded as a reference-case criterion.

2.4.4 Exceptional Point in the Present Two-Waveguide System

For the specific coupled-waveguide system studied in this thesis, the two resonance frequencies are not necessarily identical, and the radiative decay rates of the two uncoupled modes can differ. The general EP condition of Eq. (2.21) can therefore be evaluated explicitly by substituting Δ and K from Eq. (2.17) into $D = \Delta^2 + K^2$ (Eq. (2.18)), giving

$$\mathrm{Re}(D) = \frac{(\omega_1 - \omega_2)^2 - (\gamma_1 - \gamma_2)^2}{4} + g^2 - \alpha^2\gamma_1\gamma_2, \tag{2.23}$$

$$\mathrm{Im}(D) = -\left[\frac{(\omega_1 - \omega_2)(\gamma_1 - \gamma_2)}{2} + 2g\alpha\sqrt{\gamma_1\gamma_2}\right]. \tag{2.24}$$

Setting Eqs. (2.23)–(2.24) to zero gives the two real conditions that define the EP locus directly in terms of the physical parameters $(\omega_1, \omega_2, \gamma_1, \gamma_2, g, \alpha)$.

In the numerical analysis presented in the following chapters, the exceptional point is identified by locating the point (d, k_x) in this two-parameter space for which both $\mathrm{Re}(D)$ and $\mathrm{Im}(D)$ vanish simultaneously.

As already noted (Eq. (2.22)), $D = 0$ constitutes two real conditions, so that locating an exact EP generically requires two independent real control parameters. The candidates in the present system are the gap d and the longitudinal wavevector k_x. Requiring the two modes to be phase-matched would fix k_x as a function of d and reduce the search to one dimension, along which an exact coalescence is not generic. Phase matching is, however, not required by the EP condition: the second relation of Eq. (2.29), derived in Section 2.4.5, demands a real detuning $|\omega_1 - \omega_2|/2 = |\alpha|\sqrt{\gamma_1\gamma_2}$, which is finite whenever the dissipative coupling is. With d and k_x treated as independent, the two conditions can be satisfied simultaneously; this is carried out in Chapter 4.

2.4.5 Jordan Block Structure and Transformation Matrix

To rigorously formalize the transition to the exceptional point, we can map our specific waveguide model onto the general 2×2 non-Hermitian framework proposed by Heiss [14]. Heiss introduces a parameter-dependent Hamiltonian of the form:

$$H(\lambda) = H_0 + \lambda V = \begin{pmatrix} \tilde{\omega}_1 + \lambda\epsilon_1 & \lambda\delta_1 \\ \lambda\delta_2 & \tilde{\omega}_2 + \lambda\epsilon_2 \end{pmatrix} \tag{2.25}$$

To connect this with our effective Hamiltonian (Eq. (2.14)), we rename K as δ to match Heiss's notation — this δ is the complex coupling, and is not the

real detuning δ of Section 2.2 — and we absorb the radiative losses into the non-interacting energies by setting $\tilde{\omega}_k = \omega_k - i\gamma_k$ for $k = 1, 2$. By enforcing $\epsilon_1 = \epsilon_2 = 0$ and symmetric coupling $\delta_1 = \delta_2 = \delta$, our physical Hamiltonian corresponds to the parameter choice $\lambda = 1$. The Heiss Hamiltonian becomes:

$$\mathbf{H}_{\text{eff}} = \begin{pmatrix} \omega_1 - i\gamma_1 & \delta \\ \delta & \omega_2 - i\gamma_2 \end{pmatrix} \tag{2.26}$$

According to Heiss [14], the general EP condition is obtained by generalizing the discriminant of Eq. (2.18) to a λ-dependent quantity $D(\lambda)$ along the one-parameter family $H(\lambda)$, and solving $D(\lambda) = 0$ for λ, rather than evaluating it at the fixed physical point $\lambda = 1$. The coupling parameter satisfies

$$\lambda_{\text{EP}} = \frac{-i(\tilde{\omega}_1 - \tilde{\omega}_2)}{i(\epsilon_1 - \epsilon_2) \mp 2\sqrt{\delta_1 \delta_2}} = \frac{\pm i(\tilde{\omega}_1 - \tilde{\omega}_2)}{2\delta}. \tag{2.27}$$

We choose the normalization of the auxiliary parameter such that the physical Hamiltonian corresponds to $\lambda = 1$; the exceptional point is then obtained by imposing $\lambda_{\text{EP}} = 1$:

$$\delta = -\frac{i}{2}\left[(\omega_1 - \omega_2) - i(\gamma_1 - \gamma_2)\right] = -\frac{\gamma_1 - \gamma_2}{2} - i\frac{\omega_1 - \omega_2}{2} \tag{2.28}$$

Equating the real and imaginary parts to our coupling definition yields the explicit EP conditions for our two-waveguide system:

$$g = -\frac{\gamma_1 - \gamma_2}{2}, \qquad \alpha\sqrt{\gamma_1 \gamma_2} = \frac{\omega_1 - \omega_2}{2} \tag{2.29}$$

Choosing the other sign in λ_{EP} gives the second branch, $g = +(\gamma_1 - \gamma_2)/2$ and $\alpha\sqrt{\gamma_1\gamma_2} = -(\omega_1 - \omega_2)/2$, which corresponds to exchanging the labels of the two modes; the exceptional point found in Chapter 4 belongs to this branch.

As a direct cross-check, substituting these conditions into Eqs. (2.23)–(2.24) of Section 2.4.4 confirms that $\text{Re}(D) = \text{Im}(D) = 0$ identically, verifying the consistency of the two derivations.

The sign of g, and correspondingly of α, depends on the labeling and phase convention adopted for the two modes: since $\gamma_1, \gamma_2 > 0$, the second relation above fixes the sign of α to that of $\omega_1 - \omega_2$, consistent with the range $\alpha \in [-1, 1]$ introduced in Section 2.3.2. Changing the sign of one of the two modes maps $\delta \to -\delta$, that is $(g, \alpha) \to (-g, -\alpha)$, so that only the relative sign of g and α is physical. The relevant condition on the coupling strength can therefore be written as:

$$|g| = \frac{|\gamma_1 - \gamma_2|}{2}. \tag{2.30}$$

These relations define the parameter conditions under which the exceptional degeneracy occurs in the present system. At this exact point, the Hamiltonian ceases to be diagonalizable. It must instead be transformed into its Jordan normal form via a similarity matrix S, constructed using the sole independent eigenvector (first column) and its generalized associated vector (second column). For $\epsilon_1 = \epsilon_2 = 0$ and $\delta_1 = \delta_2 = \delta$, the transformation matrix [14] for our waveguide system reduces to:

$$S = \begin{pmatrix} i & \frac{1}{\delta} \\ 1 & 0 \end{pmatrix} = \begin{pmatrix} i & \frac{1}{g - i\alpha\sqrt{\gamma_1\gamma_2}} \\ 1 & 0 \end{pmatrix} \tag{2.31}$$

The corresponding inverse matrix is explicitly given by:

$$S^{-1} = \begin{pmatrix} 0 & 1 \\ \delta & -i\delta \end{pmatrix} \tag{2.32}$$

Applying this transformation yields the defective Jordan block structure:

$$S^{-1}\mathbf{H}_{\text{eff}}S = \begin{pmatrix} \tilde{\omega}_{\text{EP}} & 1 \\ 0 & \tilde{\omega}_{\text{EP}} \end{pmatrix} \tag{2.33}$$

where

$$\tilde{\omega}_{\text{EP}} = \frac{(\omega_1 - i\gamma_1) + (\omega_2 - i\gamma_2)}{2} \tag{2.34}$$

is the coalesced complex eigenfrequency. While the theoretical derivation introduces the auxiliary parameter λ to describe the approach to the EP, the physical system is driven through parameter space by varying the gap d and the in-plane wavevector k_x. These two parameters determine the evolution of the uncoupled resonance frequencies, radiative decay rates, and coupling coefficients. The corresponding two-parameter trajectory is analyzed numerically in Chapter 4.

Chapter 3

Guided Modes in Coupled Waveguides

3.1 System Geometry

The physical system analyzed in this work consists of an asymmetric, planar coupled-waveguide structure stratified along the z-axis, with electromagnetic wave propagation occurring along the longitudinal x-axis. As shown in the refractive index profile in Fig. 3.1, the multilayer stack is composed of five distinct regions: a first cladding, two high-index dielectric cores (Core 1 and Core 2) separated by a lower-index gap, and a second cladding.

The exact physical and geometric parameters defining the nominal structure are detailed in Table 3.1.

Region	Refractive index n	Thickness
Cladding 1	1.00	Semi-infinite
Core 1	2.00	400 nm
Gap	1.45	d
Core 2	3.50	220 nm
Cladding 2	1.00	Semi-infinite

Table 3.1: Physical parameters of the asymmetric coupled-waveguide structure

The asymmetry in both refractive index and thickness gives the two uncoupled modes different dispersion slopes, and their dispersion curves cross at a single wavevector within the investigated range. This crossing defines the phase-matching point around which the anticrossing of Section 3.3 is observed. The gap thickness d is used as a control parameter to investigate its effect on

the coupling strength.

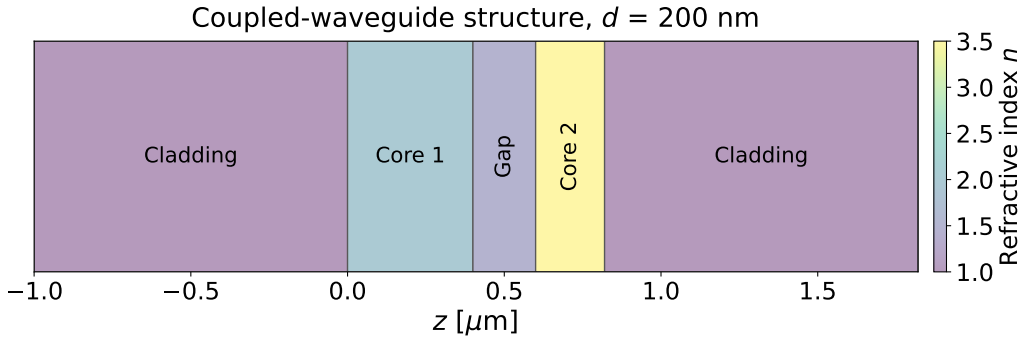


Figure 3.1: Refractive-index profile of the asymmetric coupled-waveguide structure of Table 3.1, shown for $d = 200$ nm. The five layers are the two claddings ($n = 1.00$), Core 1 ($n_1 = 2.00$, $d_{\text{core1}} = 400$ nm), the gap ($n_{\text{gap}} = 1.45$, thickness d) and Core 2 ($n_2 = 3.50$, $d_{\text{core2}} = 220$ nm). The color scale gives the refractive index and is the same in all structure and field-profile figures.

3.2 Transfer Matrix Method

To evaluate the electromagnetic response of the multilayer structure and extract its guided modes, we implemented a dedicated solver based on the transfer matrix method (TMM) [31, 32]. The TMM is a semi-analytical technique that connects the field amplitudes across an arbitrary number of homogeneous planar layers by imposing electromagnetic boundary conditions at each interface.

3.2.1 Transfer Matrix Formulation

In this work, we restrict the analysis to Transverse Electric (TE) polarization. The corresponding TM formulation, written in terms of H_y, has the same propagation matrices, while the interface matrices are modified by replacing $k_{z,j}$ with $k_{z,j}/n_j^2$ in Eq. (3.3).

For a planar system stratified along the z-axis, within the j-th homogeneous layer (characterized by a constant refractive index n_j), the solution to the scalar wave equation for TE modes can be expressed as a superposition of plane waves:

$$E_{y,j}(z) = A_j e^{ik_{z,j}z} + B_j e^{-ik_{z,j}z} \tag{3.1}$$

where A_j and B_j are the complex wave amplitudes, and $k_{z,j}$ is the transverse wavevector component in the j-th layer, defined by the dispersion relation:

$$k_{z,j} = \sqrt{\left(n_j \frac{\omega}{c}\right)^2 - k_x^2} \tag{3.2}$$

where ω/c is the vacuum wavenumber and k_x is the longitudinal propagation constant.

To relate the field amplitudes between adjacent layers, we construct two types of matrices: the interface matrix and the propagation matrix. By enforcing the continuity of the tangential electric and magnetic fields across the boundary, the interface matrix $\mathbf{T}_{j\to j+1}$ connecting layer j to layer $j+1$ is derived as:

$$\mathbf{T}_{j\to j+1} = \frac{1}{2k_{z,j+1}} \begin{pmatrix} k_{z,j+1} + k_{z,j} & k_{z,j+1} - k_{z,j} \\ k_{z,j+1} - k_{z,j} & k_{z,j+1} + k_{z,j} \end{pmatrix} \tag{3.3}$$

Inside a finite layer of thickness d_j, the fields accumulate a phase. This is described by the diagonal propagation matrix $\mathbf{T}_j(d_j)$:

$$\mathbf{T}_j(d_j) = \begin{pmatrix} e^{ik_{z,j}d_j} & 0 \\ 0 & e^{-ik_{z,j}d_j} \end{pmatrix} \tag{3.4}$$

With the positive z-direction chosen from the first towards the second cladding, the A- and B-amplitudes correspond to waves propagating along $+z$ and $-z$ respectively. The waves incoming from infinity are therefore A_1 in the first cladding and B_5 in the second. The overall action of the multilayer stack is encapsulated in a single global transfer matrix $\mathbf{T}$, obtained by sequentially multiplying the interface and propagation matrices in the order of propagation from first to second cladding:

$$\begin{pmatrix} A_5 \\ B_5 \end{pmatrix} = \mathbf{T} \begin{pmatrix} A_1 \\ B_1 \end{pmatrix} = \begin{pmatrix} T_{11} & T_{12} \\ T_{21} & T_{22} \end{pmatrix} \begin{pmatrix} A_1 \\ B_1 \end{pmatrix} \tag{3.5}$$

In our five-layer structure, $\mathbf{T}$ is calculated as:

$$\mathbf{T} = \mathbf{T}_{4\to5}\mathbf{T}_4(d_4)\mathbf{T}_{3\to4}\mathbf{T}_3(d_3)\mathbf{T}_{2\to3}\mathbf{T}_2(d_2)\mathbf{T}_{1\to2} \tag{3.6}$$

The five regions are numbered sequentially from the first cladding (layer 1) to the second cladding (layer 5), with Core 1, the gap, and Core 2 corresponding to layers 2, 3, and 4, respectively.

3.2.2 Modal Condition

Finding the natural modes (eigenstates) of the system requires identifying states that can exist autonomously, without any incoming energy from external sources at infinity.

We must therefore enforce purely outgoing (or exponentially decaying) boundary conditions. In the guided regime, these boundary conditions reduce to exponentially decaying fields in the external claddings. In the leaky regime, they are replaced by outgoing-wave conditions, allowing complex-valued eigenfrequencies. This implies that the incoming wave amplitudes from both the first cladding (A_1) and the second cladding (B_5) must be zero. Applying these boundary conditions ($A_1 = 0$ and $B_5 = 0$) to the global transfer matrix equation yields:

$$\begin{pmatrix} A_5 \\ 0 \end{pmatrix} = \begin{pmatrix} T_{11} & T_{12} \\ T_{21} & T_{22} \end{pmatrix} \begin{pmatrix} 0 \\ B_1 \end{pmatrix} \tag{3.7}$$

This leads to the relation $0 = T_{22}B_1$. Since we are looking for non-trivial field solutions ($B_1 \neq 0$), the characteristic equation for the supported modes is determined by the roots of the matrix element T_{22}:

$$T_{22}(\omega, k_x) = 0 \tag{3.8}$$

3.2.3 Root Searching Algorithm

To numerically find the roots of $T_{22}(\omega, k_x)$, we developed a three-step numerical pipeline. Because we are looking for states where T_{22} vanishes, we track the sharp resonant features that arise in the logarithmic magnitude of the matrix element.

The algorithm proceeds as follows:

1. **Global Scanning (Peak Finding):** We first perform a broad scan over the physically allowed range of ω. By utilizing the `scipy.signal.find_peaks` algorithm on the function $-\log|T_{22}|$, we identify candidate locations of the modal roots. The logarithmic scale is specifically chosen to enhance the resolution of the sharpest peaks.

2. **Interval Minimization:** Once the approximate locations are found, we define narrow brackets around each peak. The `scipy.optimize.minimize_scalar` function is applied within these intervals to locate a minimum of $|T_{22}|$.

3. **Zero Determination:** Finally, the resulting minimum is used to initialize a secant iteration (`scipy.optimize.newton` without an analytic derivative) applied to the scalar function $|T_{22}(\omega)|$. The iteration refines the frequency of the modal zero, which is accepted when the residual $|T_{22}|$ falls below the prescribed threshold.

When extending the analysis above the light line (into the leaky regime), the eigenfrequencies become complex ($\tilde{\omega} = \omega - i\gamma$) to account for radiation losses. We implemented a mode-tracking strategy to locate the complex roots of $T_{22}(\omega, k_x) = 0$. The procedure is outlined as follows:

1. **Initialization:** The root-finding process is initialized using the guided modes located just below the cladding light line. A small negative imaginary perturbation is added to the real eigenfrequency to seed the search in the dissipative regime.

2. **Complex Newton–Raphson Algorithm:** The search is performed using a custom implementation of the Newton–Raphson method generalized for complex variables. The algorithm iteratively refines the guess by calculating the numerical derivative of the matrix element via a central finite-difference scheme, and stops when the residual $|T_{22}|$ falls below 10^{-8}.

3. **Modal Tracking (Continuation):** To map the full leaky dispersion branch, we employ a sequential continuation method. The converged complex eigenvalue at a given longitudinal wavevector k_x is used as the initial guess at the adjacent wavevector, the sweep proceeding from the light line towards smaller k_x, ensuring a continuous tracking of the modal curve.

Although the solver is fully capable of tracking complex roots across the entire spectrum, the physical discussion in the remainder of this chapter is restricted strictly to purely real roots (guided modes). The dissipative dynamics and the non-Hermitian nature of the leaky regime will be thoroughly explored in Chapter 4.

3.2.4 TMM Validation

Before analyzing the five-layer structure, the solver was validated on a single-slab waveguide by comparing its dispersion diagram with the one produced by an independent code provided by the supervisor. The reference slab is defined by the parameters of Table 3.2, used identically in both codes. The comparison showed that the guided branches below the cladding light line overlap

over the whole range of normalized wavevectors, while the leaky branches above the light line are reproduced consistently in both their real and imaginary parts. Figure 3.2 shows the dispersion obtained with the present solver. This agreement validates the implementation of the modal dispersion and the complex-frequency extension above the light line.

A quantitative check is provided by normal incidence, where the quasinormal modes of a symmetric slab in air are known analytically:

$$\frac{\tilde{\omega}_m d_{\mathrm{core}}}{c} = \frac{m\pi - i\ln[(n+1)/(n-1)]}{n}, \qquad m = 1, 2, \ldots \tag{3.9}$$

For $n = \sqrt{12}$ this gives $\mathrm{Re}(\tilde{\omega}_m)\, d_{\mathrm{core}}/c = 0.907,\ 1.814,\ 2.721$ and $\mathrm{Im}(\tilde{\omega}_m)\, d_{\mathrm{core}}/c = -0.172$ for all m; at $k_x = 0$ the solver reproduces these values with a relative deviation below 10^{-10}.

Region	Refractive index n	Thickness
Cladding	1.00	Semi-infinite
Core	$\sqrt{12} \simeq 3.46$	400 nm
Cladding	1.00	Semi-infinite

Table 3.2: Parameters of the symmetric single-slab waveguide used to validate the solver. The dispersion diagram of Fig. 3.2 is expressed in the normalized variables $k_x d_{\mathrm{core}}$ and $\mathrm{Re}(\omega) d_{\mathrm{core}}/c$.

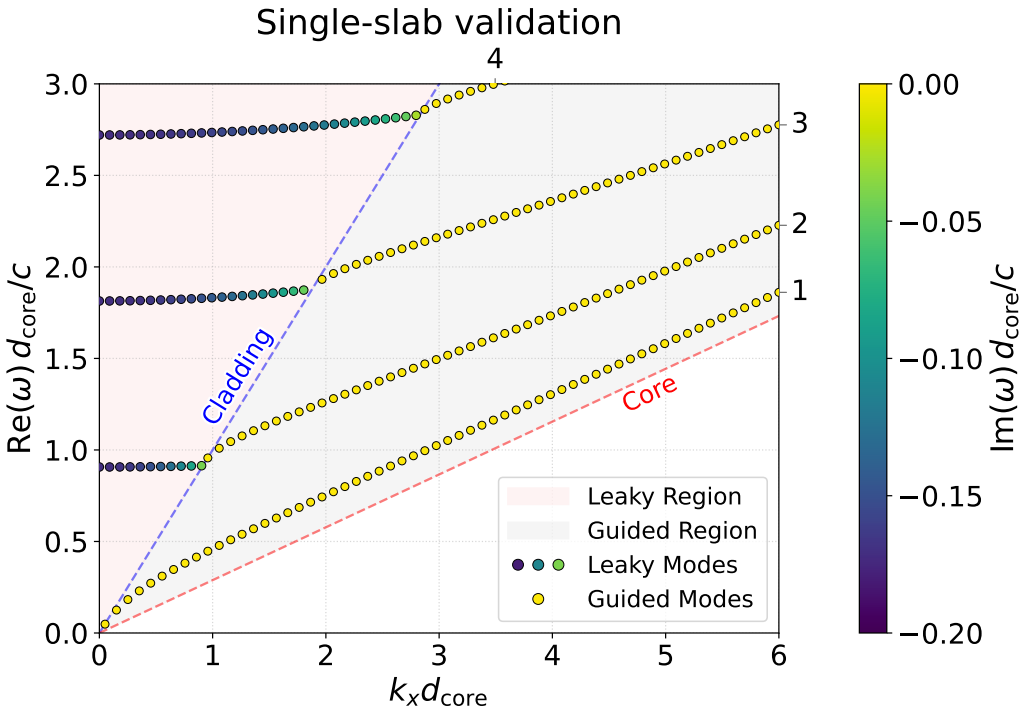


Figure 3.2: Dispersion of the single slab of Table 3.2 computed with the TMM solver, in the normalized variables $k_x d_{\mathrm{core}}$ and $\mathrm{Re}(\omega)\, d_{\mathrm{core}}/c$. Guided modes (yellow) lie between the core and cladding light lines (dashed). Leaky modes lie above the cladding light line, and their color gives $\mathrm{Im}(\omega)\, d_{\mathrm{core}}/c$. The numbers label the guided branches in order of increasing frequency. At $k_x = 0$ the leaky branches start from the analytic values of Eq. (3.9). The leaky branches are shown only to validate the complex-frequency implementation; their physics is discussed in Chapter 4.

3.3 Numerical Results

This section applies the eigenfrequency formulation introduced in Chapter 2 to the asymmetric five-layer structure of Section 3.1. The longitudinal wavevector k_x is treated as the control parameter, and the corresponding eigenfrequencies ω are extracted from $T_{22}(\omega, k_x) = 0$. The analysis focuses on the purely guided regime, where $n_{\text{eff}} = k_x/k_0$ is larger than both the cladding and gap refractive indices. Under this condition, the fields are evanescent in the claddings and in the gap, and the eigenfrequencies are strictly real.

3.3.1 Dispersion Relations

The global dispersion behavior of the coupled system is mapped out by sweeping the longitudinal wavevector k_x and finding the resonant frequencies ω that satisfy the modal condition $T_{22} = 0$.

As shown in Fig. 3.3, the solver identifies the distinct bands corresponding to the guided modes (black dots). As the frequency increases, the modes become progressively more confined within the high-index cores, and their effective indices approach the corresponding core refractive indices. Due to the geometrical and material asymmetry of the two waveguides, their individual dispersion curves possess different slopes. The different dispersion relations lead to a region of approximate phase matching between the two isolated modes. The finite gap allows the evanescent tails to overlap, transforming the isolated-mode crossing into an anticrossing of the coupled system. In Fig. 3.3 this anticrossing involves branches 2 and 3 near $k_x c \simeq 3.3 \times 10^{15}$ rad/s and $\omega \simeq 1.8 \times 10^{15}$ rad/s. The red points above the cladding light line correspond to leaky modes of the same structure; they are shown only for completeness, while the guided-mode analysis is restricted to the black branches.

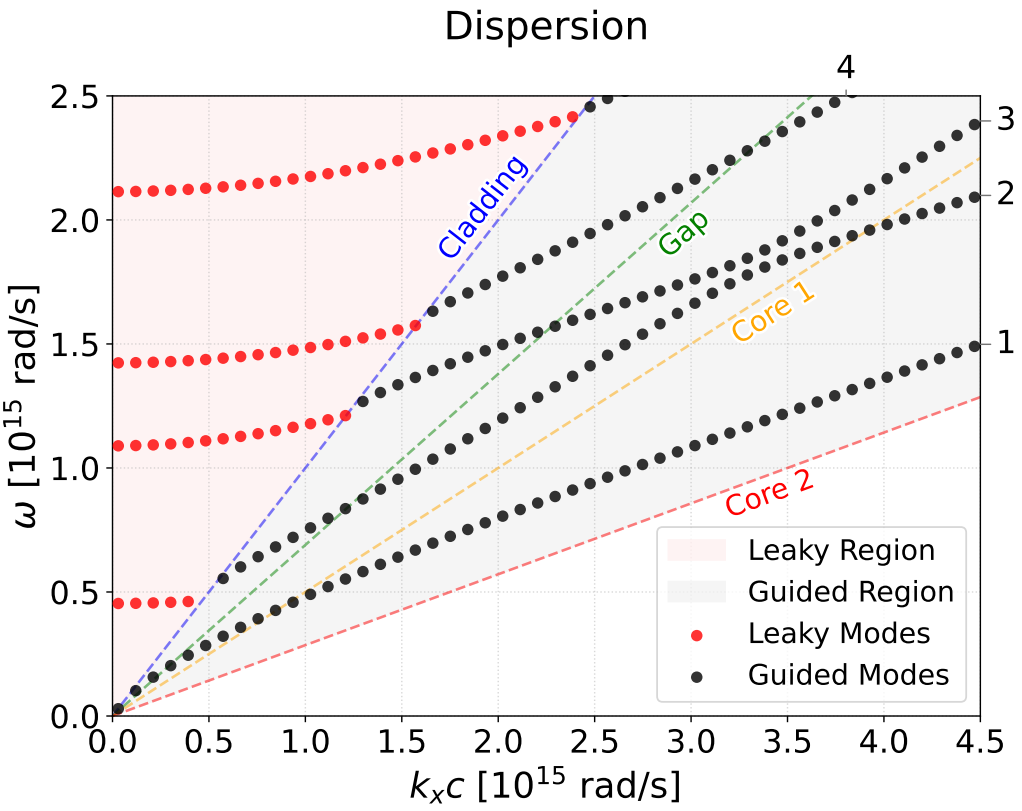


Figure 3.3: Dispersion of the coupled waveguides of Table 3.1 for $d = 200$ nm. Black: guided modes. Red: leaky modes above the cladding light line, shown for completeness. Dashed lines: light lines of the cladding, gap, Core 1 and Core 2. The numbers label the guided branches in order of increasing frequency; the anticrossing analyzed in Sections 3.3.2–3.3.3 is between branches 2 and 3.

3.3.2 Supermode Formation

To understand the nature of the modes near the anticrossing region, we extract and reconstruct the transverse electric field profiles $E_y(z)$. When the phase-matching condition is met, the system does not support isolated modes confined strictly in Core 1 or Core 2, but rather hybridized states known as supermodes.

Figure 3.4 illustrates the normalized field amplitudes for the two split branches at $k_x = 1.10 \times 10^7$ rad/m, for a representative gap of $d = 200$ nm. The lower-frequency branch corresponds to a symmetric-like (in-phase) supermode, where the fields in the two cores oscillate in phase. Conversely, the higher-frequency branch corresponds to an antisymmetric-like (out-of-phase) supermode, char-

acterized by a π phase shift between the two cores and a node inside the gap. The non-zero evanescent field within the gap ($0.4\mu\text{m} < z < 0.6\mu\text{m}$) provides the spatial overlap responsible for the coherent coupling between the two cores. In both supermodes the field in Core 2 has one node: the interacting pair is formed by the fundamental TE_0 mode of Core 1 and the first-order TE_1 mode of Core 2. Their group indices, $1/s_1 \simeq 2.1$ and $1/s_2 \simeq 4.1$ (Table 3.3), show that the Core 2 mode is the slower of the two.

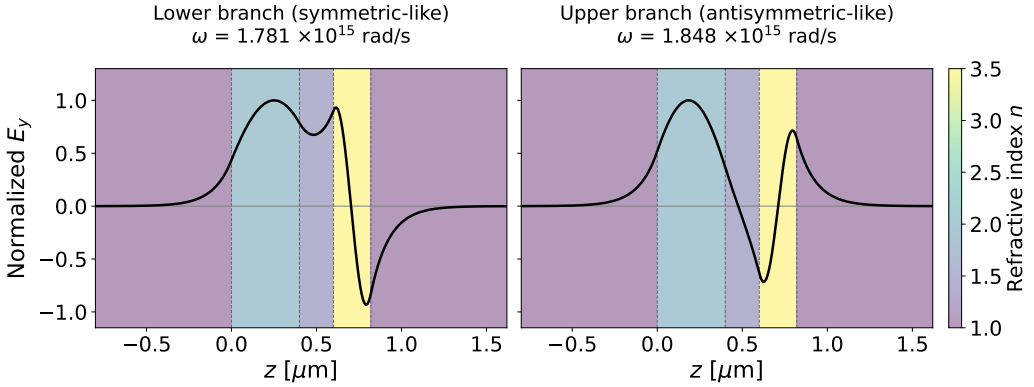


Figure 3.4: Transverse field profiles $E_y(z)$ of the two supermodes at the anticrossing, for $d = 200$ nm and $k_x = 1.10 \times 10^7$ rad/m. Left: symmetric-like supermode (lower branch). Right: antisymmetric-like supermode (upper branch). Each profile is normalized to its maximum $|E_y|$ and taken positive in Core 1. The background color gives the refractive index.

3.3.3 Coherent Coupling and Hamiltonian Fitting

The anticrossing observed in the TMM dispersion is described quantitatively by a Hermitian two-mode Hamiltonian. Within the coupled-mode theory (CMT) framework, the TMM dispersion data are mapped onto the reduced 2×2 model:

$$\mathbf{H}_\omega = \begin{pmatrix} \omega_1 & g \\ g & \omega_2 \end{pmatrix} \tag{3.10}$$

where ω_1 and ω_2 are the uncoupled eigenfrequencies of Core 1 and Core 2 at a given k_x, and g is the coherent coupling strength. This constitutes a reduced-order description of the full electromagnetic problem and allows the coherent coupling strength to be extracted from the observed mode splitting.

The eigenfrequencies predicted by this model are

$$\omega_{\pm} = \frac{\omega_1 + \omega_2}{2} \pm \sqrt{\left[\frac{\omega_1 - \omega_2}{2}\right]^2 + g^2}. \tag{3.11}$$

To accurately model the dispersion in the vicinity of the anticrossing, the uncoupled modal dispersion relations are locally approximated as linear functions of the longitudinal wavevector. Since the fitting procedure is performed using the scaled variable $q = k_x c$, we write

$$\omega_i = \omega_{0,i} + s_i q, \qquad q = k_x c, \tag{3.12}$$

where $s_i = d\omega_i/dq$ is a dimensionless dispersion slope related to the group velocity by $v_{g,i} = c\, s_i$ and the index $i \in \{1, 2\}$ denotes the waveguide core. The fitting procedure therefore involves five free parameters in total: the coherent coupling strength g, and two parameters for each waveguide (the frequency intercept $\omega_{0,i}$ and the slope s_i).

The five parameters are determined by a simultaneous nonlinear least-squares fit of both TMM dispersion branches to the two eigenvalues of $\mathbf{H}_\omega$ (Fig. 3.5). The optimization is performed over the selected k_x interval around the phase-matching region.

For the representative configuration with $d = 200$ nm, the fit yields the coherent coupling

$$g = (3.36 \pm 0.01) \times 10^{13} \text{ rad/s}. \tag{3.13}$$

This value comes from a fit of the $d = 200$ nm configuration using 20 wavevectors in $[0.9, 1.4] \times 10^7$ rad/m, whereas the gap sweep of Table 3.3 uses the 17 points of the global grid that fall in the same interval; the difference between the two fitted values corresponds to 0.13 times their combined standard uncertainty.

Furthermore, by analyzing the eigenvectors of the Hamiltonian, we can calculate the modal weight $|\psi_1|^2$ associated with Core 1. The colormap in Fig. 3.5 shows the corresponding redistribution of the modal weight between the two waveguides: far from the phase-matching point, the modes are essentially isolated (purely red or purely blue), while at the anticrossing, the modal weight is evenly distributed between the two waveguides ($|\psi_1|^2 = 0.5$), indicating maximum hybridization.

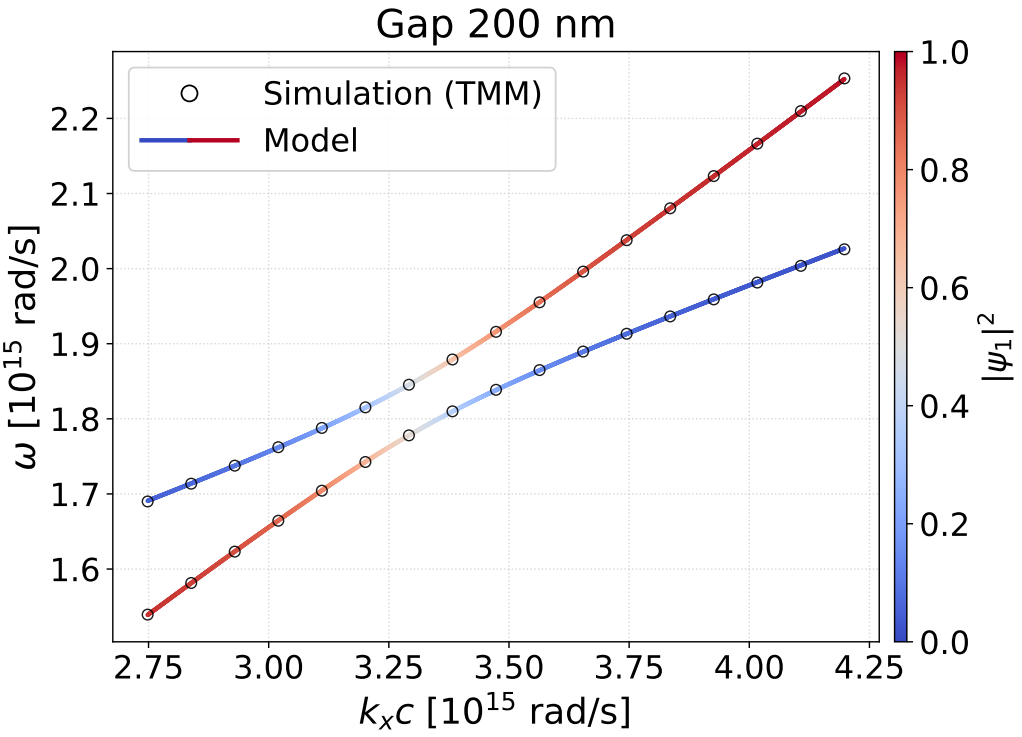


Figure 3.5: Anticrossing region for $d = 200$ nm. Open circles: TMM eigenfrequencies. Lines: eigenvalues of the fitted Hermitian Hamiltonian H_ω of Eq. (3.10), colored by the weight $|\psi_1|^2$ of the Core 1 mode in each eigenvector (red: mode localized in Core 1; blue: in Core 2). The curves are those of the gap sweep (Table 3.3); the denser fit of Eq. (3.13) is indistinguishable on this scale.

3.3.4 Dependence on Gap Thickness

The strength of the coherent coupling g is fundamentally governed by the spatial overlap of the evanescent tails of the uncoupled modes within the gap. Because the fields in the strictly guided regime decay exponentially outside the cores, the coupling coefficient itself is expected to exhibit an exponential dependence on the gap thickness d.

To verify this, we repeated the Hamiltonian fitting for varying gap thicknesses: $d = 100$ nm, 200 nm, 300 nm, 400 nm, 500 nm. As the gap increases, the separation between the split branches at the anticrossing decreases, denoting a weaker interaction (Fig. 3.6); the corresponding Hamiltonian fits are shown in Fig. 3.7.

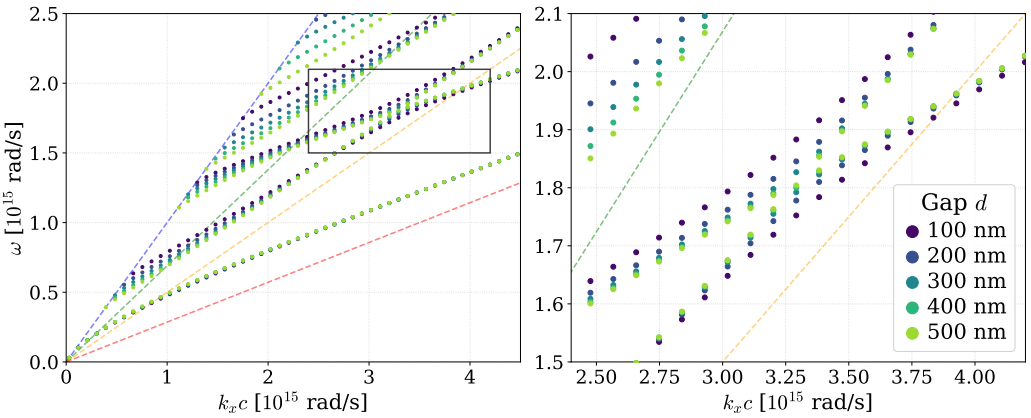


Figure 3.6: Guided dispersion for $d = 100$–500 nm (color: gap thickness). Left: full wavevector range, with the light lines of the four materials (dashed); the rectangle marks the region enlarged on the right. Right: zoom on the anticrossing. As d increases the splitting between the two branches decreases, reflecting the decay of the coherent coupling.

By plotting the extracted coupling strengths g as a function of the gap thickness on a logarithmic scale, we observe a linear trend. The data are well described by the exponential decay law:

$$g(d) = Ae^{-\eta d} = Ae^{-\frac{d}{L_d}} \tag{3.14}$$

where A is a prefactor with the dimensions of g, $\eta = 1/L_d$ is the inverse decay length, and L_d is the decay length of the coupling. This exponential dependence is consistent with the evanescent-field-mediated coupling expected in the guided regime.

The fitted couplings and dispersion slopes for each gap thickness are reported in Table 3.3; the main quantity of interest is the coherent coupling strength g.

Fitting the extracted couplings gives a decay length $L_d = 149.9 \pm 0.7$ nm (Fig. 3.8).

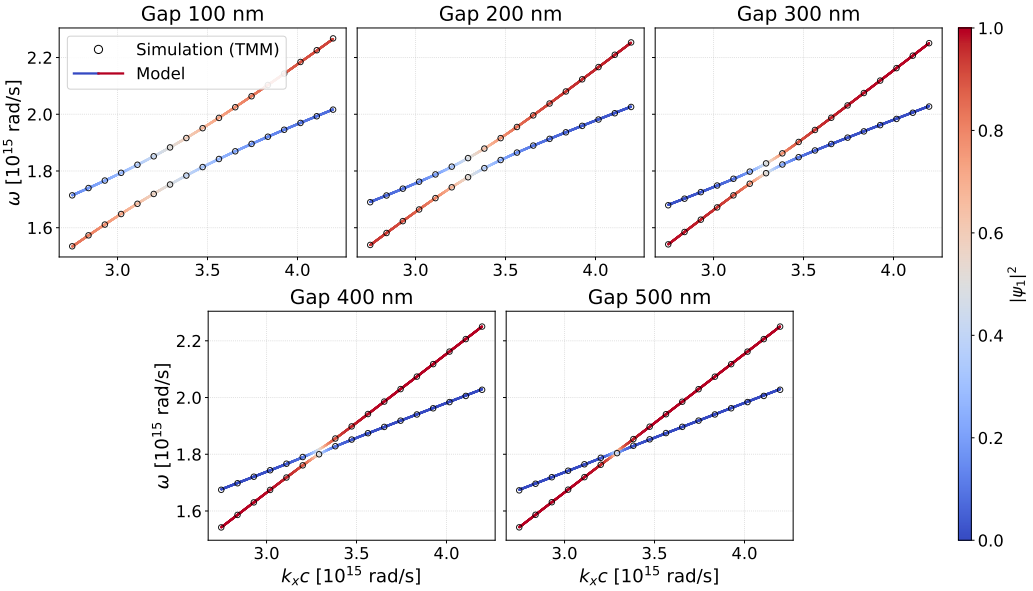


Figure 3.7: Hermitian Hamiltonian fits for $d = 100$–500 nm. Open circles: TMM eigenfrequencies; lines: eigenvalues of H_ω, colored by $|\psi_1|^2$ as in Fig. 3.5. As d increases, the region of strong hybridization ($|\psi_1|^2 \approx 0.5$) shrinks around the crossing point.

The value of the decay length can be compared with the transverse decay constant of the evanescent field in the gap, evaluated at the anticrossing point already used in Fig. 3.4 ($d = 200$ nm, $k_x = 1.10 \times 10^7$ rad/m, $\omega \simeq 1.82 \times 10^{15}$ rad/s, the average of the two split branches, corresponding to a vacuum wavelength $\lambda = 2\pi c/\omega \simeq 1.04\ \mu$m),

$$\kappa_{\text{gap}} = \frac{1}{c}\sqrt{(k_x c)^2 - (n_{\text{gap}}\omega)^2}, \tag{3.15}$$

with $n_{\text{gap}} = 1.45$ from Table 3.1. This gives $\kappa_{\text{gap}} = 6.64 \times 10^6$ m^{-1}, corresponding to $1/\kappa_{\text{gap}} \simeq 150.7$ nm, in agreement with the fitted decay length $L_d = 149.9 \pm 0.7$ nm to within one percent. Since the crossing point q_{cross} varies by less than 0.3% across the five gaps (Section 3.4), κ_{gap} is effectively the same for all of them. The coherent coupling is therefore governed directly by the evanescent decay of the fields in the gap, as anticipated at the beginning of this section.

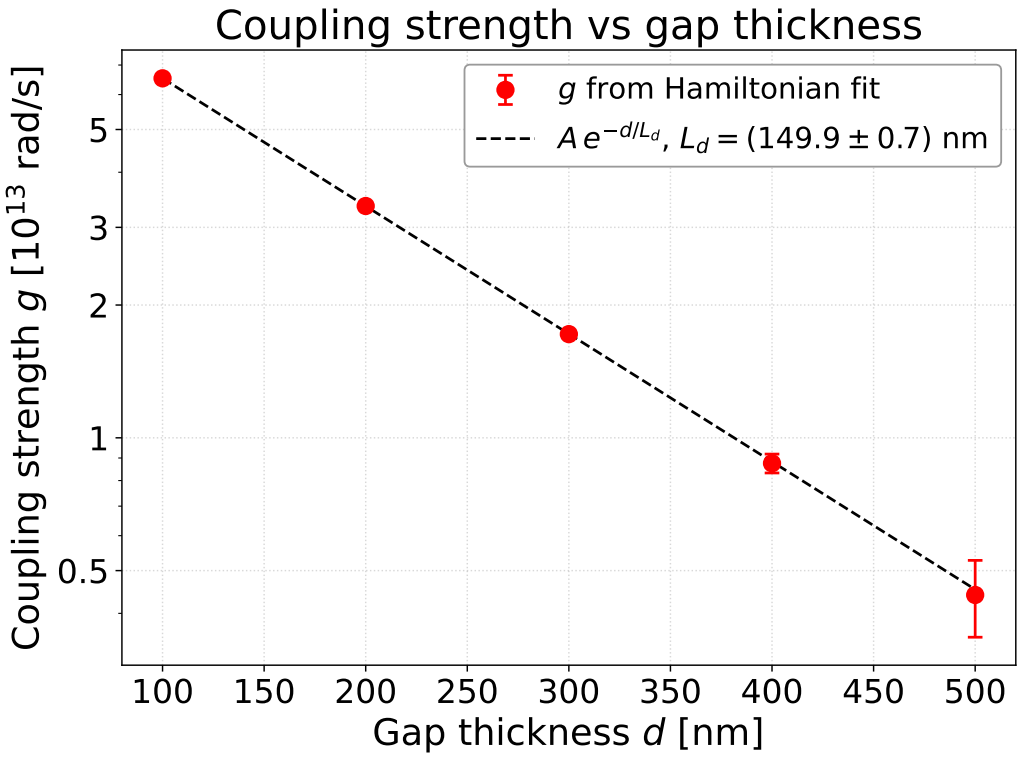


Figure 3.8: Exponential decay of the coherent coupling strength g as a function of the gap thickness d. The extracted coupling values (red dots) follow a linear trend within the investigated range on a semi-logarithmic scale, in agreement with an evanescent-field-mediated coupling mechanism. The fitted decay length of the coupling is $L_d = 149.9 \pm 0.7$ nm.

d [nm]	g [rad/s]	s_1	s_2
100	$(6.531 \pm 0.012) \times 10^{13}$	0.4728 ± 0.0004	0.2407 ± 0.0004
200	$(3.354 \pm 0.012) \times 10^{13}$	0.4832 ± 0.0003	0.2407 ± 0.0003
300	$(1.718 \pm 0.018) \times 10^{13}$	0.4868 ± 0.0003	0.2426 ± 0.0003
400	$(8.75 \pm 0.43) \times 10^{12}$	0.4878 ± 0.0004	0.2441 ± 0.0004
500	$(4.40 \pm 0.87) \times 10^{12}$	0.4881 ± 0.0005	0.2450 ± 0.0005

Table 3.3: Best-fit coherent coupling g and dispersion slopes s_1, s_2 of the effective Hamiltonian, for the investigated gap thicknesses. The slopes are dimensionless because the fit is expressed in terms of the scaled longitudinal variable $q = k_x c$; the corresponding group velocities are $v_{g,i} = c\, s_i$. The uncertainties are one standard deviation from the covariance matrix of the nonlinear least-squares fit. Since the TMM eigenfrequencies are computed deterministically to numerical precision, the reported uncertainties quantify the local parameter uncertainty associated with the fit rather than measurement noise. The frequency intercepts $\omega_{0,i}$ are not listed: they are extrapolated far outside the fitted window and carry no physical meaning (Section 3.4).

3.4 Discussion

In the guided regime, the TMM solver maps the modal dispersion and shows the hybridization of the two isolated waveguide modes into symmetric-like and antisymmetric-like supermodes. The Hermitian two-mode Hamiltonian reproduces the TMM branches and yields the coherent coupling g, with a relative uncertainty of 0.4% for the representative case $d = 200$ nm.

The fitted dispersion slopes s_1 and s_2 and, to a good approximation, the physical crossing point of the two bare dispersions remain stable across the investigated gap range. Solving $\omega_1(q) = \omega_2(q)$ independently for each gap gives $q_{\text{cross}} = (3.296 \pm 0.009) \times 10^{15}$ rad/s, with a variation of 0.3% across the five fits. In contrast, the intercepts $\omega_{0,i}$, extrapolated to $q = 0$ far outside the fitted region, vary by up to $\sim 30\%$. The corresponding small variations of the fitted slopes are amplified by the extrapolation, so the intercepts do not carry a direct physical meaning.

These results show that increasing the gap primarily suppresses the inter-waveguide coupling rather than significantly modifying the individual modal dispersions. The avoided crossing and the exponential decay of g with gap thickness are therefore consistent with a conservative, Hermitian interaction dominated by evanescent-field overlap. Within the lossless guided-mode regime, energy is exchanged coherently between the two cores without radiative dissipation.

This guided-mode picture applies only below the cladding light line. Above the light line, the modes radiate into the claddings, their eigenfrequencies become complex, and the effective Hamiltonian becomes non-Hermitian. Chapter 4 extends the analysis to this radiative regime, where the guided-mode anticrossing can evolve into a coalescence of eigenvalues and eigenvectors at an exceptional point.

Chapter 4

Leaky Modes in Coupled Waveguides

4.1 Structure and Method

4.1.1 Modified Geometry

Extending the analysis to the leaky regime is not simply a matter of following the modal branches of Chapter 3 above the cladding light line. The non-Hermitian dynamics of interest require two ingredients at the same time: the modes must retain an evanescent overlap inside the gap, which sustains the coherent coupling g, and they must radiate into the claddings, which generates the decay rates $\gamma_{1,2}$. In the reference case of negligible dissipative coupling and phase matching, the exceptional point is reached when the coherent coupling balances half the difference of the decay rates (Section 2.4); radiation into common channels can also produce the dissipative coupling $\alpha\sqrt{\gamma_1\gamma_2}$. In terms of the effective index, which we define here through the real part of the complex eigenfrequency as $n_{\mathrm{eff}} = k_x c/\,\mathrm{Re}(\tilde{\omega})$, the two requirements for simultaneous evanescent coupling and radiation amount to the double inequality

$$n_{\mathrm{gap}} < n_{\mathrm{eff}} < n_{\mathrm{clad}}, \tag{4.1}$$

where the left inequality keeps the transverse wavevector imaginary in the gap and the right one makes it real in the claddings.

The structure of Table 3.1 cannot satisfy Eq. (4.1). That geometry is adequate for the guided analysis, but there the window is empty: with $n_{\mathrm{gap}} > n_{\mathrm{clad}}$, a mode cannot be evanescent in the gap and radiate into the claddings at the same time.

We therefore exchange the gap and cladding indices, so that the gap becomes the *lowest*-index region of the stack: $n_{\text{gap}} = 1.00$ and $n_{\text{clad}} = 1.45$ (Table 4.1). We keep the core thicknesses unchanged, and the gap d remains the control parameter: we sweep it over 300–1400 nm, with finer sampling between 680 and 820 nm where the transition of Section 4.3.4 occurs.

Region	Refractive index n	Thickness
Cladding 1	1.45	Semi-infinite
Core 1	2.20	400 nm
Gap	1.00	d
Core 2	3.50	220 nm
Cladding 2	1.45	Semi-infinite

Table 4.1: Physical parameters of the structure used in the leaky regime. Relative to Table 3.1 the gap and cladding indices are exchanged, so that the window of Eq. (4.1) is non-empty, and the index of Core 1 is raised from 2.00 to 2.20.

The index of Core 1 is raised to 2.20 so that the TE_1 branches of the two cores cross inside the window of Eq. (4.1).

The resulting index profile is shown in Fig. 4.1.

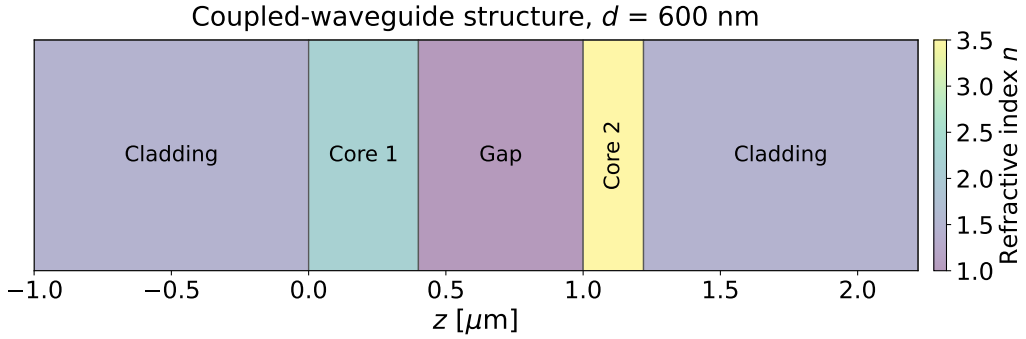


Figure 4.1: Refractive-index profile of the structure of Table 4.1, shown for $d = 600$ nm, with the same color scale as Fig. 3.1. Compared with Fig. 3.1 the gap is now the lowest-index region of the stack.

As noted in Section 1.3, the asymmetry is essential: with $\omega_1 = \omega_2$ and $\gamma_1 = \gamma_2$, Eqs. (2.23)–(2.24) vanish only for $g = \alpha = 0$.

We identify the interacting pair as the first-order transverse modes, TE_1, of the two cores; in the guided structure of Chapter 3 the pair was instead formed by TE_0 of Core 1 and TE_1 of Core 2. Throughout this chapter we illustrate the

analysis at the representative separation $d = 600$ nm, where the two branches reach their minimum splitting at $k_x^{\mathrm{ref}} c = 1.63 \times 10^{15}$ rad/s, corresponding to $n_{\mathrm{eff}} = 1.19$, that is $\mathrm{Re}(\tilde{\omega}) \simeq 1.37 \times 10^{15}$ rad/s and a vacuum wavelength of 1.37 μm.

4.1.2 Complex-Frequency Solver

Above the cladding light line, the modal condition $T_{22}(\omega, k_x) = 0$ of Eq. (3.8) no longer admits real solutions, and we therefore seek the eigenfrequencies in the lower complex half-plane, $\tilde{\omega} = \omega - i\gamma$ with $\gamma > 0$. The transfer matrix formalism of Section 3.2 carries over unchanged; what requires attention is the branch of the transverse wavevector

$$k_{z,j} = \sqrt{\left(n_j \frac{\tilde{\omega}}{c}\right)^2 - k_x^2}. \tag{4.2}$$

In the two semi-infinite claddings, the chosen branch fixes the outgoing-wave convention [36]. We use the principal branch throughout, defined by $\mathrm{Re}(k_{z,j}) \geq 0$ and $k_{z,j} = +i|k_{z,j}|$ for negative real argument. The absence of incoming waves is then imposed by the modal condition $A_1 = B_5 = 0$, as in Section 3.2.

The global scan of Section 3.2.3 has no counterpart in two dimensions; we replace it with continuation. We displace each guided mode close to the light line into the dissipative half-plane by a small imaginary perturbation, refine it with the complex Newton–Raphson iteration of Section 3.2.3, and use the converged eigenvalue to seed the adjacent wavevector. Because two branches can approach each other closely near an exceptional point, where the separation of Eq. (2.19) vanishes with a square-root topology, the iteration seeded on one branch can converge on the other; we therefore relabel the two branches after each step by minimizing their total displacement in the complex plane relative to the previous wavevector.

4.2 Non-Hermitian Effective Hamiltonian

4.2.1 Parametric Model

The effective Hamiltonian of Eq. (2.14) describes the interaction at a single wavevector, whereas the solver returns two complex branches over an interval of k_x. To exploit the full interval, we introduce an explicit k_x dependence for each Hamiltonian parameter and linearize it about a reference point. Using the scaled variable $q = k_x c$ introduced in Section 3.3.3 and writing $\Delta q = q - q_{\mathrm{ref}}$,

$$\omega_j(q) = \omega_0 + s_j \Delta q, \tag{4.3}$$
$$\gamma_j(q) = \gamma_{0,j} + \gamma'_j \Delta q, \tag{4.4}$$
$$g(q) = g_0 + g_1 \Delta q. \tag{4.5}$$

with $j \in \{1,2\}$, while the dissipative coupling retains the form $\alpha\sqrt{\gamma_1\gamma_2}$ of Section 2.3.2. The slopes s_j, γ'_j and g_1 are dimensionless, as in Chapter 3, while g_0 is the coherent coupling at the reference point. The term g_1 captures the leading wavevector dependence of the coherent coupling within the fitted window. This dependence is physically motivated by the variation of the evanescent decay constant in the gap with k_x, but the linear form is used here as a local approximation. The fit is performed over $k_x \in [0.4, 0.7] \times 10^7$ rad/m, corresponding to a half-width of 4.5×10^{14} rad/s in q. At $d = 600$ nm the fitted data span $q = 1.20$–1.91×10^{15} rad/s (19 points), that is, from -4.3 to $+2.8 \times 10^{14}$ rad/s around q_{ref}.

Substituting Eqs. (4.3)–(4.5) into Eq. (2.14) gives the explicit form of the fitted Hamiltonian,

$$\mathbf{H}_{\mathrm{eff}}(q) = \begin{pmatrix} \omega_1(q) - i\gamma_1(q) & g(q) - i\alpha\sqrt{\gamma_1(q)\gamma_2(q)} \\ g(q) - i\alpha\sqrt{\gamma_1(q)\gamma_2(q)} & \omega_2(q) - i\gamma_2(q) \end{pmatrix}, \tag{4.6}$$

whose eigenvalues, obtained from Eq. (2.15), are compared with the TMM data as described below.

We give the two bare branches the same intercept ω_0, so that $\omega_1(q_{\mathrm{ref}}) = \omega_2(q_{\mathrm{ref}})$ and the real detuning vanishes at the reference point by construction. We define q_{ref} as the point of minimum splitting of the real parts of the two TMM branches, $\mathrm{Re}(\tilde{\omega}_+) - \mathrm{Re}(\tilde{\omega}_-)$, determined directly from the computed eigenvalues and therefore independently of the fit. It is redetermined at each gap thickness. This choice is a convention: when the two decay rates differ, the crossing of the bare frequencies need not coincide with the minimum of the real splitting, and the fitted value of α depends on it (Section 4.2.2). In the gap sweep q_{ref} is taken on the computed k_x grid and is therefore known to within one grid step, about 1.1×10^{13} rad/s. Substituting $\omega_1 = \omega_2$ into Eqs. (2.23)–(2.24), we obtain, at q_{ref},

$$\mathrm{Im}(D) = -2g\alpha\sqrt{\gamma_1\gamma_2}, \qquad \mathrm{Re}(D) = g^2 - \frac{(\gamma_1 - \gamma_2)^2}{4} - \alpha^2\gamma_1\gamma_2, \tag{4.7}$$

so that $\mathrm{Im}(D) = 0$ requires $\alpha = 0$ whenever $g \neq 0$, and $\mathrm{Re}(D) = 0$ then reduces to $|g| = |\gamma_1 - \gamma_2|/2$, which is Eq. (2.30). This reduction is a property

of the reference point rather than of the exceptional point. At q_{ref} the real detuning vanishes by construction, whereas the general condition of Eq. (2.29) requires a finite detuning whenever $\alpha \neq 0$. Section 4.4 evaluates D away from the reference point and locates the exceptional point close to it.

We quote uncertainties throughout this section from the covariance matrix of each fit, rescaled so that the reduced χ^2 equals unity. Because the TMM eigenfrequencies are computed deterministically to numerical precision, these uncertainties do not represent measurement noise. Instead, they quantify how strongly the fitted parameters are constrained by the residual mismatch between the full electromagnetic calculation and the two-mode model. The same normalization is used for all models, so the comparison in Table 4.2 is consistent across parametrizations.

4.2.2 Model Comparison

The parametrization of Eqs. (4.3)–(4.5) contains eleven parameters, of which three describe effects absent from the guided analysis: the wavevector dependence g_1 of the coherent coupling, the dissipative coupling α, and the reference point q_{ref} itself, if left free rather than fixed at the minimum-splitting point. Rather than fitting all of them at once, we compared the models obtained by releasing, singly or in combination, g_1, α and q_{ref}, starting from a baseline in which the two modes are coupled only through a constant g_0 (Table 4.2). The goal is to find the minimal model, that is, the one with the fewest parameters that still reproduces the TMM eigenvalues.

The baseline is inadequate. Its coupling is purely real, so it can split the decay rates only through the difference between the two bare ones, $\gamma_1(q)$ and $\gamma_2(q)$: at the reference point, the splitting of the imaginary parts cannot exceed $|\gamma_1 - \gamma_2|$. The model therefore reproduces the anticrossing of the real parts but systematically underestimates the splitting of the imaginary parts. With q_{ref} fixed, the two intermediate models, $+g_1$ and $+\alpha$, separate the contributions of the two additional terms, and we find that they differ greatly in importance. Releasing g_1 alone lowers the residual by ten percent, from $\chi = 0.217$ to 0.195; releasing α alone lowers it by seventy percent, to $\chi = 0.060$. Adding both gives $\chi = 0.047$, and the wavevector dependence of the coherent coupling provides a secondary improvement on top of the dominant contribution of the dissipative term. With the reference point fixed at the minimum-splitting point, the two leaky branches cannot be reproduced by a purely coherent interaction.

Model	Additional free parameters	N_{par}	χ
Base	—	8	0.217
$+g_1$	g_1	9	0.195
$+\alpha$	α	9	0.060
$+q_{\mathrm{ref}}$	q_{ref}	9	0.090
$+g_1,\ \alpha$	$g_1,\ \alpha$	10	0.047
$+g_1,\ q_{\mathrm{ref}}$	$g_1,\ q_{\mathrm{ref}}$	10	0.047
$+\alpha,\ q_{\mathrm{ref}}$	$\alpha,\ q_{\mathrm{ref}}$	10	0.047
$+g_1,\ \alpha,\ q_{\mathrm{ref}}$	$g_1,\ \alpha,\ q_{\mathrm{ref}}$	11	0.047

Table 4.2: Normalized RMS residual $\chi = \sqrt{\langle[(y_{\mathrm{data}} - y_{\mathrm{model}})/\sigma]^2\rangle}$ (not a formal χ^2) for the Hamiltonian models at $d = 600$ nm. The baseline contains ω_0, s_1, s_2, $\gamma_{0,1}$, $\gamma_{0,2}$, γ_1', γ_2' and g_0; the other models add g_1, α and/or q_{ref}. Because the TMM eigenfrequencies are computed deterministically to numerical precision, no measurement uncertainty is available. The quantity σ is taken as the standard deviation of the data over the fitted window. The normalized residual χ therefore measures the residual in units of the spread of the data themselves, so only the ratios between the models are meaningful. Fits with q_{ref} free were started from several initial values of q_{ref} across the window; the lowest residual is reported.

The fit of the adopted model, $+g_1,\ \alpha$, is shown in Fig. 4.2, while the fits of all the other models of Table 4.2 are collected in Appendix C. As in Chapter 3, the color of the model curves gives the weight of the Core 1 mode in each eigenvector, $|\psi_1|^2/(|\psi_1|^2 + |\psi_2|^2)$, computed from the right eigenvectors of Eq. (4.6). Since the two right eigenvectors are not orthogonal, their Core 1 weights at a given q need not sum to one.

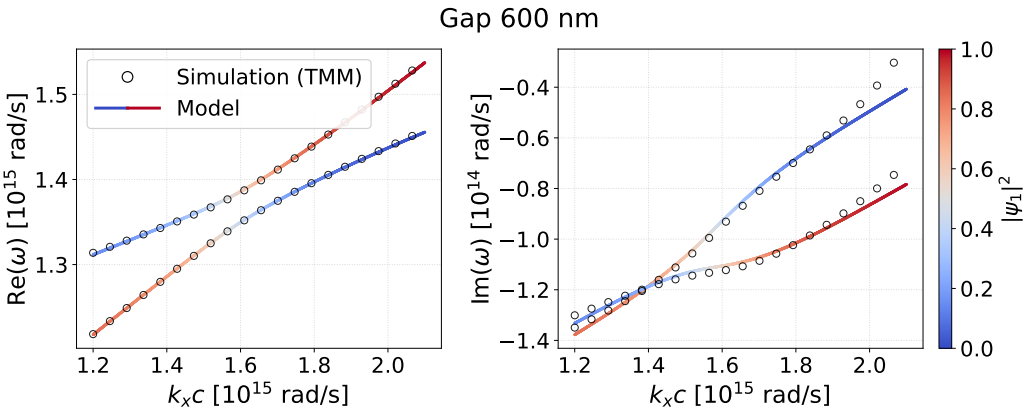


Figure 4.2: Real (left) and imaginary (right) parts of the eigenfrequencies near the anticrossing, for $d = 600$ nm. Open circles: TMM eigenfrequencies in the fitted window. Lines: eigenvalues of the non-Hermitian Hamiltonian of Eq. (4.6) for the model $+g_1$, α, colored by the weight $|\psi_1|^2$ of the Core 1 mode.

The same conclusion follows from the fitted decay rates, independently of the residual. In the baseline the two decay-rate slopes γ_1' and γ_2' differ by a factor of 2.7, and adding g_1 leaves them nearly as asymmetric; once we release α they converge to within ten percent of each other. With the reference point fixed, a model without dissipative coupling can only reproduce the observed splitting of the imaginary parts by forcing the two uncoupled modes to have strongly different decay rates. Releasing q_{ref} alone does not remove this: the $+q_{\mathrm{ref}}$ model reaches only $\chi = 0.090$, with decay rates that differ by a factor of 3.9 at the reference point.

Releasing q_{ref} as well leaves χ unchanged at the fourth decimal and makes the fit degenerate: the uncertainty returned for α then exceeds its value by five orders of magnitude, and that on q_{ref} by four. The degeneracy involves the couplings. Since the two bare branches share the intercept ω_0, a shift of q_{ref} introduces a constant detuning between them, which only α and g_1 can compensate. Fixing one of the two removes the degeneracy but not the ambiguity: with $g_1 = 0$ and α, q_{ref} free the fit reaches the same $\chi = 0.047$ with $\alpha = 0.135$ instead of 0.087, and with $\alpha = 0$ and g_1, q_{ref} free it reaches it with a purely coherent coupling that changes sign inside the fitted window, at $q \simeq 1.86 \times 10^{15}$ rad/s. The data therefore do not determine q_{ref}, g_1 and α separately, and the solution with $\alpha = 0$, whose coherent coupling changes sign, is not physically consistent with the assumed evanescent-overlap origin of the coherent coupling. We adopt the ten-parameter model with q_{ref} fixed at the minimum-splitting point of Section 4.2.1, and regard the value of α as

defined relative to this convention.

The ten-parameter model is retained while both coupling contributions and their wavevector dependence remain sufficiently resolved by the fit. As the gap widens the coherent coupling falls towards the scale set by the difference of the decay rates, and we reduce the parametrization in stages, as summarized in Table 4.3: we fix g_1 to zero first, then g_0 as well, leaving the dissipative coupling as the only off-diagonal term, and finally take the Hamiltonian diagonal at the largest separations.

Gap range	Off-diagonal term	Constrained parameters
$d \le d_1$	$g_0 + g_1\Delta q - i\alpha\sqrt{\gamma_1\gamma_2}$	—
$d_1 < d \le d_2$	$g_0 - i\alpha\sqrt{\gamma_1\gamma_2}$	$g_1 = 0$
$d_2 < d \le d_3$	$-i\alpha\sqrt{\gamma_1\gamma_2}$	$g_0 = g_1 = 0$
$d > d_3$	0	$g_0 = g_1 = \alpha = 0$

Table 4.3: Reduction of the coupling parametrization with increasing separation. The thresholds are $d_1 = 760$ nm, $d_2 = 850$ nm and $d_3 = 1350$ nm. The regime boundaries are parametrization cutoffs selected from fit quality and parameter identifiability.

We set the thresholds by comparing the residual of the full model against its reduced forms across the fitted range, guided by the physical expectation that the coherent coupling — a near-field, exponentially decaying quantity — should become negligible before the far-field dissipative term does. Although g_0 and g_1 remain individually resolved at more than twenty standard deviations at d_1, near this gap the linear form of Eq. (4.5) changes sign in the upper part of the fitted window, which has no physical meaning for an evanescent overlap. Beyond d_1 we therefore constrain $g_1 = 0$, at the cost of an increase of the residual from $\chi = 0.068$ to 0.104.

Since the thresholds are chosen with the help of the fits themselves, one may ask whether the zero of α is produced by the regime switching. As a control, the full ten-parameter model was fitted at every gap thickness without any regime switching. Because this fit never constrains g_0 to zero, it provides an independent check on the location of the zero of α: it vanishes between $d =$ 750 nm and $d = 760$ nm and remains compatible with zero, with a negative sign, up to 850 nm, matching the threshold d_1 to within the sampling of the gap sweep. The zero of α is therefore not produced by the regime switching. The unconstrained fit does, however, become numerically degenerate beyond $d \simeq 875$ nm, where g_0 falls below its own uncertainty by an order of magnitude and the residual χ rises monotonically to 0.13 at $d = 1400$ nm. We constrain

$g_0 = 0$ beyond $d_2 = 850$ nm (Table 4.3) to obtain a resolved fit. The values of α found there depend on this constraint, because in the weak-coupling regime g_0, α and the difference of the decay rates enter the eigenvalues in nearly degenerate combinations.

4.3 Numerical Results

4.3.1 Complex Dispersion and Field Profiles

Above the cladding light line, we find that the solver returns a set of radiative branches whose eigenfrequencies acquire decay rates of order 10^{14} rad/s, so that $Q = \omega/2\gamma \simeq 6$ for the mode of Core 1 and between 7 and 15 for that of Core 2 (Fig. 4.3). The resonances are therefore broad, and the mode splitting remains a fraction of the linewidth over the whole range studied: the anti-crossing we analyze is a property of the complex eigenvalues returned by the solver rather than a spectrally resolvable feature. This is not incidental to the exceptional point. Its condition, Eq. (2.30), is set by the difference of the decay rates, so a structure with narrow resonances would reach it only at much weaker coupling, that is, at much larger separations.

The field profiles of the selected pair, shown in Fig. 4.4, differ from the guided supermodes of Fig. 3.4 in two respects: the field is oscillatory rather than evanescent in the claddings, and it has a non-vanishing imaginary part whose spatial structure carries the phase lag between the two radiating cores.

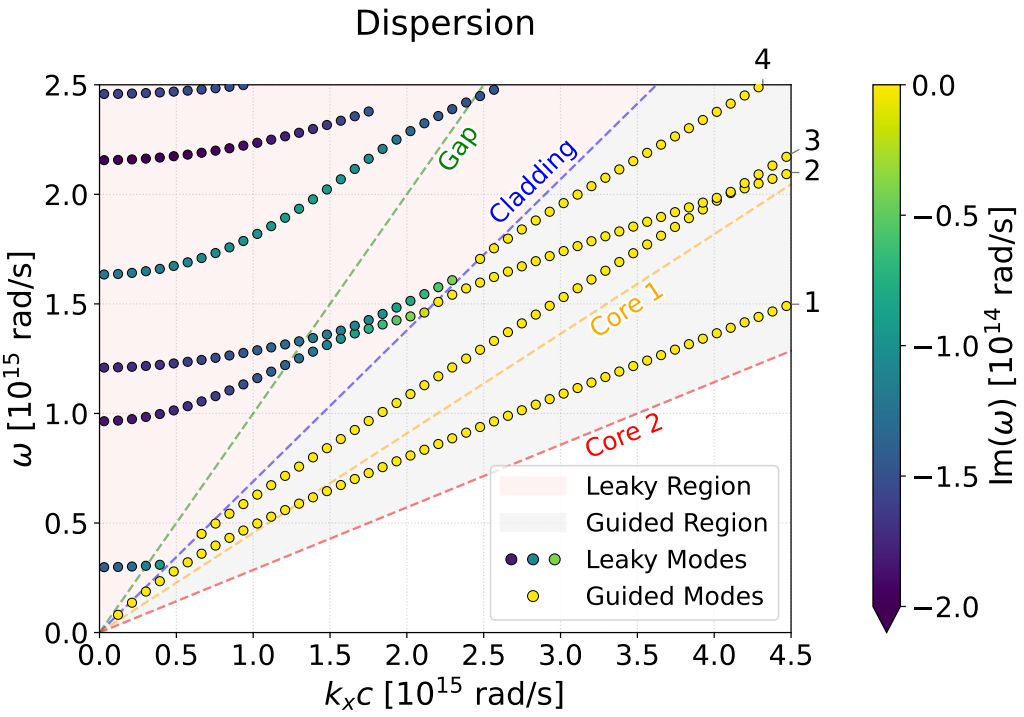


Figure 4.3: Dispersion of the structure of Table 4.1 for $d = 600$ nm. Guided modes (yellow) lie below the cladding light line. Leaky modes lie above it, and their color gives $\mathrm{Im}(\tilde{\omega}) = -\gamma$, where γ is the radiative decay rate; values below -2×10^{14} rad/s are saturated. Dashed lines: light lines; the numbers label the guided branches in order of increasing frequency.

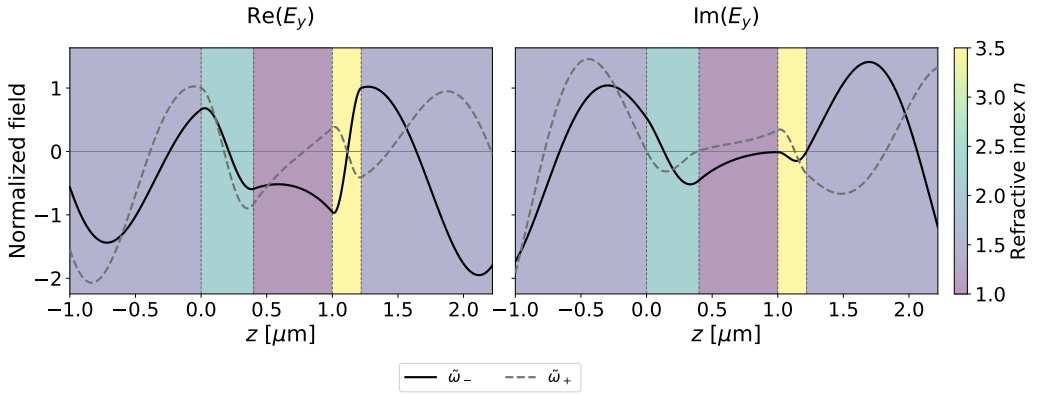


Figure 4.4: Real (left) and imaginary (right) parts of $E_y(z)$ for the two branches of the interacting pair ($\tilde{\omega}_-$, lower real frequency, solid; $\tilde{\omega}_+$, dashed), for $d =$ 600 nm at $q_{\mathrm{ref}} = 1.63 \times 10^{15}$ rad/s. Each profile is normalized so that $E_y = 1$ at the point of maximum $|E_y|$ inside the stack. The fields grow in the claddings, as expected for quasinormal modes with outgoing-wave boundary conditions. Background color: refractive index.

4.3.2 Coherent Coupling

We find that the coherent coupling extracted from the fits decreases with separation and follows, over the range in which it is well resolved, the same exponential law found in the guided regime:

$$g_0(d) = A e^{-\eta d}, \qquad \eta = (3.60 \pm 0.03) \times 10^6 \ \mathrm{m}^{-1}, \tag{4.8}$$

corresponding to a decay length $L_d = 278.1 \pm 2.4$ nm (Fig. 4.5). We compare this value with the transverse decay constant of the evanescent field in the gap, evaluated at the reference point,

$$\kappa_{\mathrm{gap}} = \frac{1}{c}\sqrt{(k_x^{\mathrm{ref}} c)^2 - \omega_0^2}, \tag{4.9}$$

with $n_{\mathrm{gap}} = 1$. Because the reference point moves to smaller effective index as d increases, from $n_{\mathrm{eff}} = 1.28$ at 300 nm to 1.13 at 760 nm, κ_{gap} is not constant over the fitted range: it decreases from 3.8 to 2.4×10^6 m^{-1}. Between 300 and 600 nm, where it ranges from 3.8 to 2.9×10^6 m^{-1} with mean 3.41×10^6 m^{-1}, the ratio is $\eta/\kappa_{\mathrm{gap}} = 1.06$, and comparing the two interval by interval we obtain ratios of 1.12, 0.99, 1.09 and 1.22 between 300 and 650 nm. Closer to the transition the coupling decays faster than the evanescent field, with local ratios of 1.2–1.5, so that over the whole fitted range η exceeds the mean κ_{gap} by 28%. We conclude that g_0 is governed by the overlap of the evanescent

tails inside the gap, as in Section 3.3.4, with a faster decay near d_1, where the wavevector dependence of the coupling is largest.

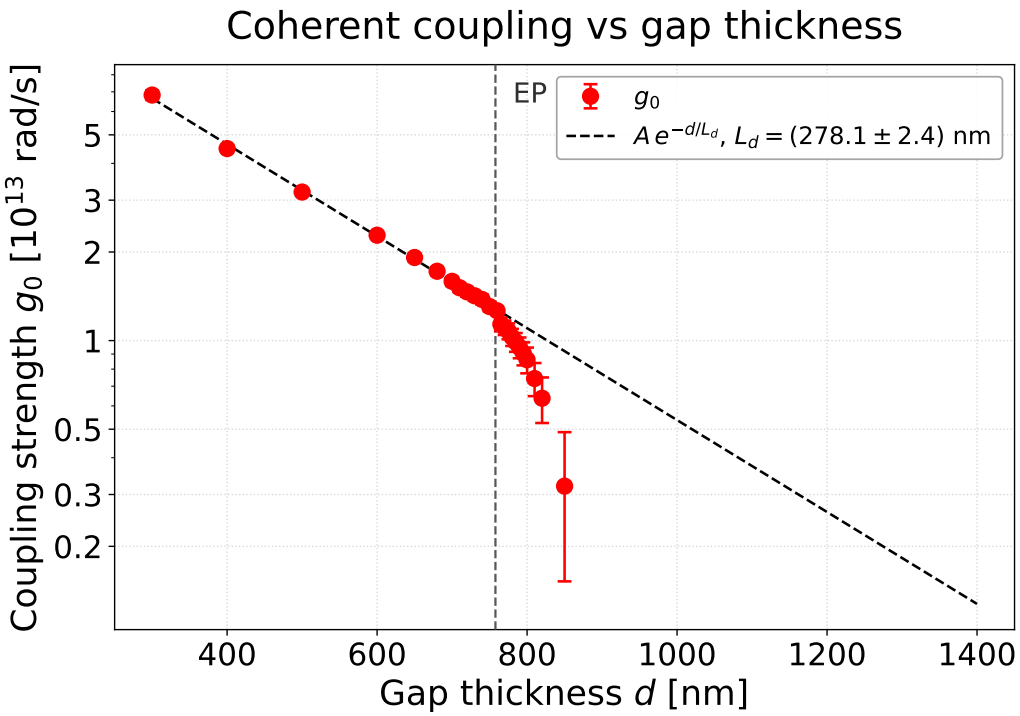


Figure 4.5: Coherent coupling g_0 as a function of the gap thickness, on a semi-logarithmic scale. Dashed line: exponential fit over $d \leq 760$ nm, with $L_d = 278.1 \pm 2.4$ nm, to be compared with $1/\kappa_{\text{gap}} \simeq 293$ nm, the mean over 300–600 nm (356 nm over the whole fitted range). The points at $760 < d \leq 850$ nm come from the model $+\alpha$ ($g_1 = 0$, Table 4.3) and are not included in the fit; beyond $d_2 = 850$ nm, g_0 is constrained to zero. Vertical dashed line: exceptional point, $d^* = 757.8$ nm.

Unlike in the guided case, the coupling also acquires a wavevector dependence. We find the fitted slope g_1 negative at every separation, between -0.019 and -0.062, with the largest magnitude at d_1, which is consistent with Eq. (4.9): κ_{gap} increases with k_x, so the tails decay faster and the overlap is weaker at the upper end of the window. Near d_1 this variation exceeds g_0 in the upper part of the fitted interval, where the linear form of Eq. (4.5) changes sign; for this reason the exceptional point search of Section 4.4.2 is restricted to $|\Delta q| \leq 10^{14}$ rad/s.

4.3.3 Dissipative Coupling

The dissipative coupling, defined relative to the reference point, behaves differently. We find α decreasing from 0.192 at $d = 300$ nm to zero at $d = 759$ nm (Fig. 4.6). Fitting three functional forms over $d \leq 760$ nm, we obtain $R^2 = 0.890$ for an exponential law, which cannot reach zero at finite d, 0.987 for a linear one, and 0.996 for a quadratic one.

The sign of α beyond d_1 must be read with care. Only the relative sign of g and α is physical (Section 2.4.5). In the parametrization of Table 4.3, the fits of the model $+\alpha$ at $760 < d \leq 850$ nm return $g_0\alpha > 0$, as below d_1: α vanishes at d_1 but does not change sign (Fig. 4.6), and $\mathrm{Im}(D)$ at q_{ref} touches zero there rather than crossing it (Fig. 4.9). In the unconstrained ten-parameter fit of Section 4.2.2, instead, α becomes slightly negative beyond 760 nm, within two standard deviations of zero up to 850 nm, while in the model $+\alpha$ it is positive at four standard deviations or more (e.g. $\alpha = 0.021 \pm 0.004$ at 780 nm). The two parametrizations agree on the vanishing of α near 760 nm, but not on its sign beyond that point: the zero of α is therefore more robust than its sign away from the reference point. Once g_1 is set to zero, α absorbs part of the wavevector dependence of the coupling, the same partial degeneracy between g_1 and α found at $d = 600$ nm.

Beyond d_2, where g_0 is constrained to zero, the eigenvalues depend on α only through α^2, so its sign is not determined. Its magnitude, within this parametrization, does not simply vanish: within the weak-coupling window 850–1350 nm a quadratic fit to $|\alpha|$ gives $R^2 = 0.962$ and shows an apparent secondary maximum, $|\alpha| \simeq 0.11$ near $d \simeq 1100$ nm, before decreasing towards zero at the largest separations (Fig. 4.7). Whether this reflects an oscillatory dependence of the dissipative coupling on the gap cannot be established with the present data, also because beyond d_2 the fitted α depends on the constraint $g_0 = 0$.

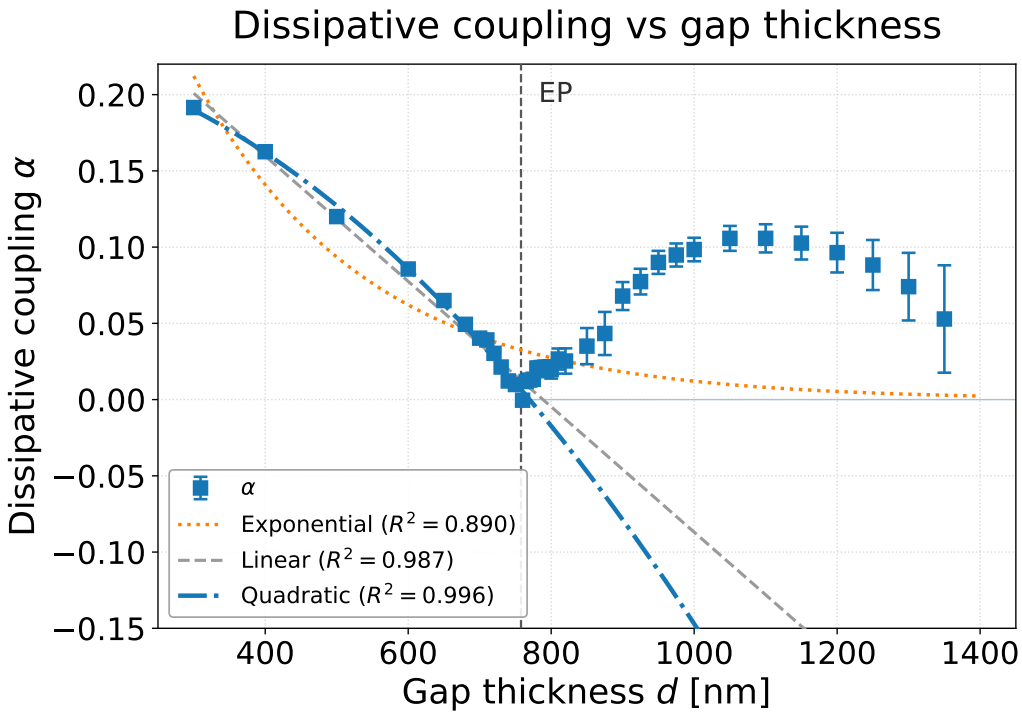


Figure 4.6: Dissipative coupling α as a function of the gap thickness, from the regime-dependent parametrization of Table 4.3. Exponential (dotted), linear (dashed) and quadratic (dash-dotted) forms are fitted over $d \leq 760$ nm and extrapolated across the full range; the points at larger d are shown for reference and are not used in the fits. For $d > d_2 = 850$ nm only $|\alpha|$ is determined. Vertical dashed line: exceptional point. Unlike the exponential decay of g_0 in Fig. 4.5, none of these forms describes α over its full range.

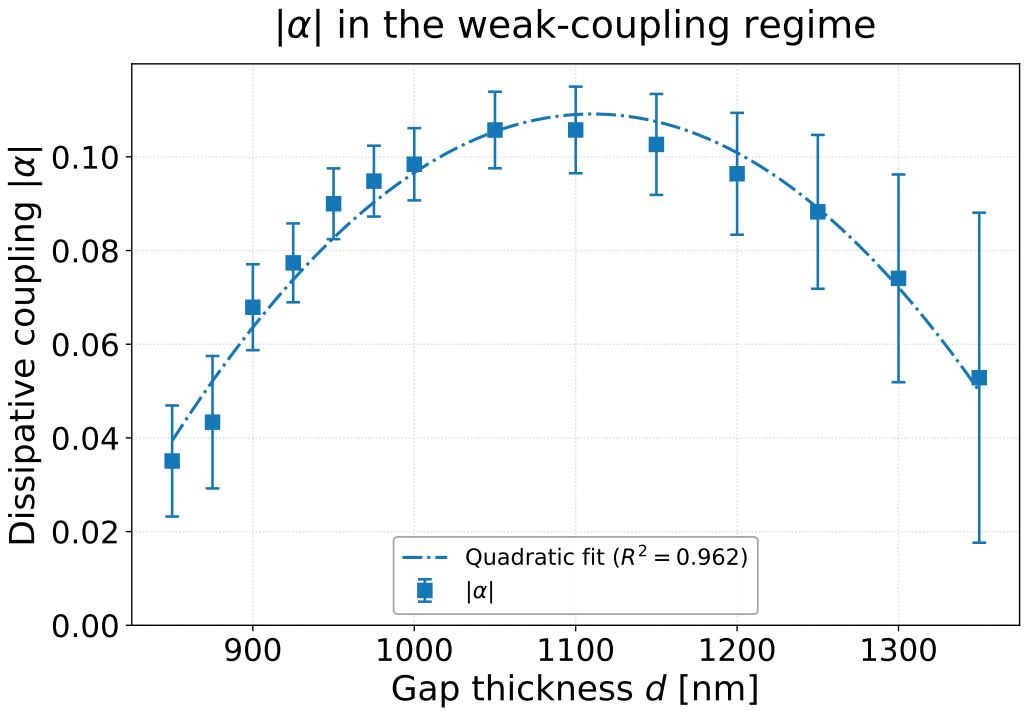


Figure 4.7: $|\alpha|$ in the weak-coupling window 850–1350 nm, where g_0 is constrained to zero, with a quadratic fit ($R^2 = 0.962$) showing the apparent secondary maximum discussed in the text.

The coherent coupling is a near-field quantity, set by the overlap of two exponentially decaying tails inside the gap, and inherits their exponential dependence on d. The dissipative coupling depends instead on how the radiation of the two modes is shared between the two claddings and, unlike g_0, vanishes at a finite separation. Representative values of both couplings are collected in Table 4.4.

d [nm]	Model	g_0 [rad/s]	α
300	$+g_1,\ \alpha$	$(6.83 \pm 0.26) \times 10^{13}$	$+0.1915 \pm 0.0022$
500	$+g_1,\ \alpha$	$(3.20 \pm 0.06) \times 10^{13}$	$+0.1200 \pm 0.0017$
700	$+g_1,\ \alpha$	$(1.59 \pm 0.06) \times 10^{13}$	$+0.0403 \pm 0.0018$
760	$+g_1,\ \alpha$	$(1.26 \pm 0.04) \times 10^{13}$	-0.0004 ± 0.0023
900	α-only	—	$+0.0679 \pm 0.0092$
1100	α-only	—	$+0.1057 \pm 0.0092$

Table 4.4: Coherent and dissipative coupling at representative gap thicknesses, from the regime-dependent parametrization of Table 4.3. A dash indicates a parameter constrained to zero rather than fitted: beyond $d_2 = 850$ nm this applies to g_0, and beyond $d_3 = 1350$ nm to α as well. The uncertainties are one standard deviation from the covariance matrix, as discussed in Section 4.2.1.

4.3.4 From Strong to Weak Coupling

The balance between the coherent coupling and the half-difference of the decay rates drives the system through the transition anticipated in Section 2.4.3. We compare g_0 with half the difference of the decay rates, the two quantities entering the exceptional point condition $|g| = |\gamma_1 - \gamma_2|/2$ of Eq. (2.30). Both decrease with separation, but g_0 decreases faster: their ratio falls from 1.80 at $d = 300$ nm to unity between 740 and 750 nm, where the balance between the two reverses.

We show the eigenvalues in Fig. 4.8. At the smallest separations the real parts display a clear anticrossing while the imaginary parts approach each other, the behavior we identified as strong coupling in Section 2.4.3. As the gap widens the anticrossing narrows and the two decay rates separate, until beyond the gap at which g_0 falls below $|\Delta\gamma|$ the real parts pass through each other while the imaginary parts split. The system has moved into the weak-coupling regime.

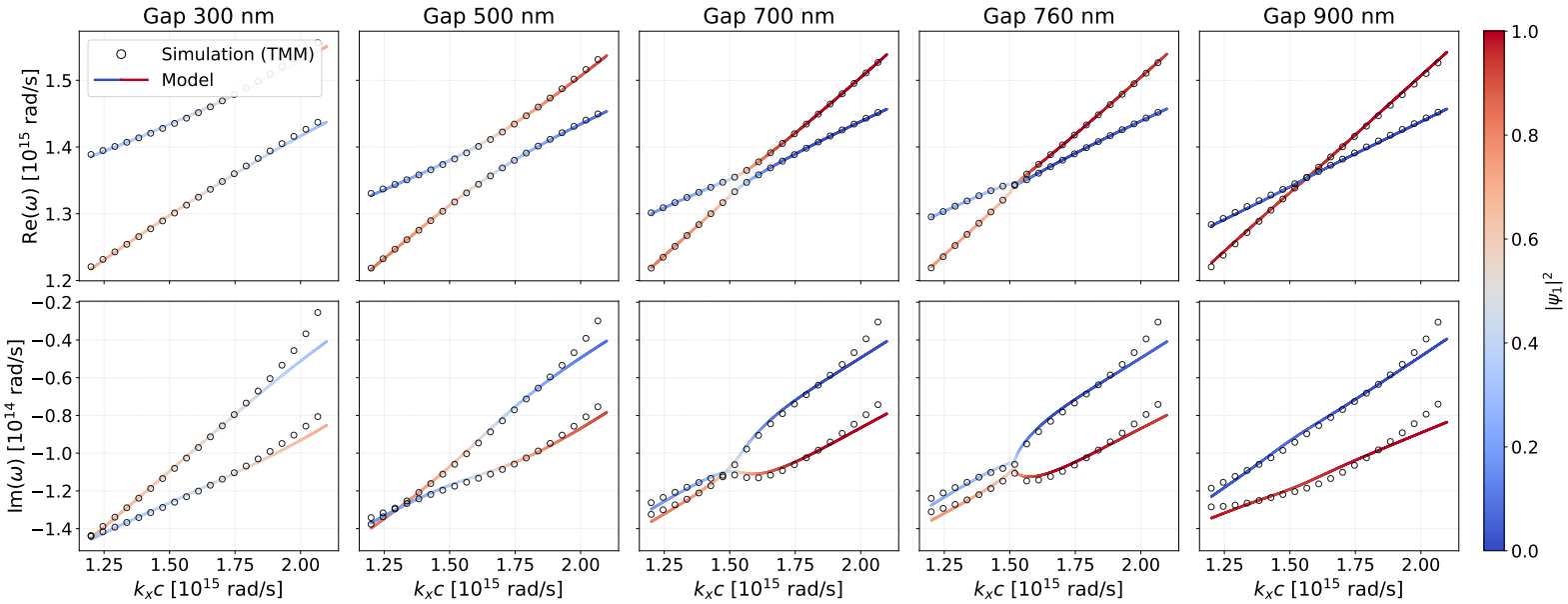


Figure 4.8: Real (top) and imaginary (bottom) parts of the eigenfrequencies for $d = 300$, 500, 700, 760 and 900 nm, from deep strong coupling, through the approach to the exceptional point, to weak coupling. Open circles: TMM eigenfrequencies in the fitted window; lines: model eigenvalues, colored by $|\psi_1|^2$. The anticrossing of the real parts narrows and closes as d increases, while the splitting of the imaginary parts grows in its place.

In the plane $(d, \Delta q)$ the two regimes meet at a single point, where eigenvalues and eigenvectors coalesce; along a path that misses it, such as the reference trajectory $\Delta q = 0$, the change is a smooth crossover (Section 4.4.3). Locating this point is the subject of the following section.

4.4 Localization of the Exceptional Point

4.4.1 Discriminant at the Reference Point

The transition of Section 4.3.4 is governed by the discriminant $D = \Delta^2 + K^2$ of Eq. (2.18), which vanishes at an exceptional point [14]. We first evaluate D at q_{ref} from the fitted parameters, where it reduces to the two expressions of Eq. (4.7). Interpolating between the fitted separations, we find

$$\mathrm{Re}(D) = 0 \ \text{ at } \ d = 745 \pm 12 \text{ nm}, \qquad \mathrm{Im}(D) = 0 \ \text{ at } \ d = 759 \pm 2 \text{ nm}. \quad (4.10)$$

The first is the condition $|g_0| = |\gamma_{0,1} - \gamma_{0,2}|/2$ identified in Section 4.3.4, and the second is the vanishing of α. They are met at separations that differ by 14 nm, comparable to the uncertainty of the less well determined of the two (Fig. 4.9).

At the reference point, the two conditions constrain the gap alone, and two real conditions on a single parameter are generically incompatible. The mismatch originates from the choice of q_{ref}: the real detuning vanishes there by construction, whereas the general EP condition requires $|\Delta\omega| = |\Gamma_{12}|$. Introducing the real detuning $\Delta\omega$, the decay-rate difference $\Delta\gamma$, and the dissipative coupling Γ_{12},

$$\Delta\omega = \frac{\omega_1 - \omega_2}{2}, \qquad \Delta\gamma = \frac{\gamma_1 - \gamma_2}{2}, \qquad \Gamma_{12} = \alpha\sqrt{\gamma_1\gamma_2}, \quad (4.11)$$

the EP conditions of Eq. (2.29) become $|g| = |\Delta\gamma|$ and $|\Delta\omega| = |\Gamma_{12}|$. At q_{ref} the first condition is tested correctly, but the second condition reduces to $\alpha = 0$ because $\Delta\omega = 0$ by construction. The two zeros found at 745 nm and 759 nm therefore diagnose the failure of the reference trajectory to satisfy both EP conditions simultaneously; they do not represent an exact exceptional point.

Phase matching is a choice of where to evaluate the discriminant, not a physical constraint on the exceptional point. The in-plane wavevector $q = k_x c$ is an independent control parameter and can be varied experimentally through the angle of incidence at fixed frequency. Because the fitted Hamiltonian of Eq. (4.6) already contains the dependence on $\Delta q = q - q_{\mathrm{ref}}$, the exceptional point must be sought in the full two-parameter plane $(d, \Delta q)$ rather than along

the reference trajectory $\Delta q = 0$: we refer to this as the q-dependent correction to the exceptional point condition.

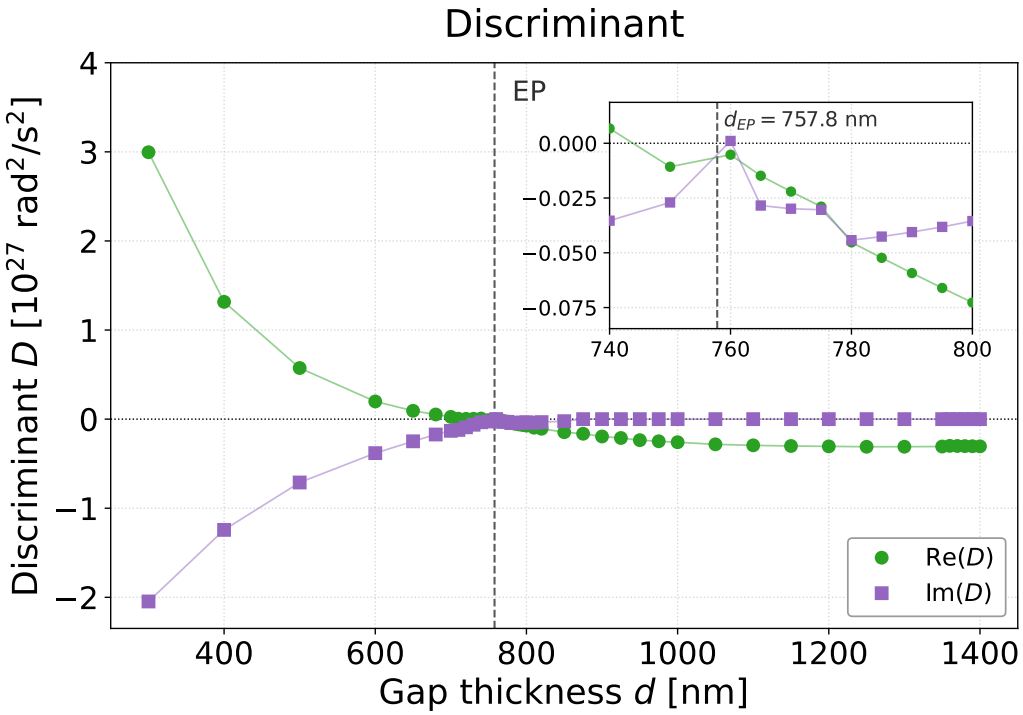


Figure 4.9: Real and imaginary parts of the discriminant D at q_{ref} as a function of the gap thickness; the lines join the sampled gaps. Inset: enlargement of 740–800 nm. Re(D) vanishes at 745 ± 12 nm and Im(D) at 759 ± 2 nm. Beyond $d_2 = 850$ nm, where g_0 is constrained to zero, Im(D) vanishes identically at q_{ref} and carries no information. Vertical dashed line: exceptional point of Section 4.4.2.

4.4.2 q-Dependent Correction

With the notation of Eq. (4.11), $\Delta = \Delta\omega - i\Delta\gamma$ and $K = g - i\Gamma_{12}$, so that Eqs. (2.23)–(2.24) become

$$\text{Re}(D) = \Delta\omega^2 - \Delta\gamma^2 + g^2 - \Gamma_{12}^2, \qquad \text{Im}(D) = -2\,(\Delta\omega\,\Delta\gamma + g\,\Gamma_{12}), \quad (4.12)$$

where all quantities now depend[1] on both d and Δq through Eqs. (4.3)–(4.5). In particular $\Delta\omega = (s_1 - s_2)\,\Delta q/2$ vanishes only at the reference point. For $g \neq$

[1] $\Delta\omega$ and $\Delta\gamma$ are half-differences between the two modes, whereas Δq denotes an offset from the reference wavevector.

0 the condition $\mathrm{Im}(D) = 0$ gives $\Gamma_{12} = -\Delta\omega\,\Delta\gamma/g$; substituting into $\mathrm{Re}(D) = 0$ and multiplying by g^2 yields

$$\left(g^2 - \Delta\gamma^2\right)\left(g^2 + \Delta\omega^2\right) = 0. \tag{4.13}$$

The second factor is strictly positive, since $g \neq 0$ by assumption. The exceptional point is therefore defined by

$$g = \pm\,\Delta\gamma, \qquad \Delta\omega = \mp\,\Gamma_{12}, \tag{4.14}$$

with the signs taken together and both relations evaluated at the same point $(d, \Delta q)$. The first relation has the same form as Eq. (2.30), but it must hold at the detuning fixed by the second relation rather than at $\Delta q = 0$. Since g and $\Delta\gamma$ both depend on Δq, the gap at which it is met differs from the 745 nm found at the reference point.

We solve these conditions using the fitted parameters of the $+g_1,\ \alpha$ model, which is the adopted parametrization because it retains both the wavevector dependence of the coherent coupling and the dissipative coupling while keeping q_{ref} fixed by the data. For each gap we locate the root $\Delta q(d)$ of $\mathrm{Im}(D)$ closest to the reference point, restricting the search to $|\Delta q| \leq 10^{14}$ rad/s where the linearization of Eqs. (4.3)–(4.5) holds, and then find the zero of $\mathrm{Re}(D)$ along this curve. The two zero loci intersect at

$$d^* = 757.8 \text{ nm}, \qquad \Delta q^* = -3.1 \times 10^{12} \text{ rad/s}, \tag{4.15}$$

a detuning of 0.7% of the half-width of the fitted window (Fig. 4.10). At this point $g = +\Delta\gamma = 1.29 \times 10^{13}$ rad/s and $\Delta\omega = -\Gamma_{12} = -1.94 \times 10^{11}$ rad/s, which is the upper-sign branch of Eq. (4.14); the lower-sign branch, which reproduces Eq. (2.29) directly, corresponds to exchanging the labels of the two modes (Appendix A). The coalesced eigenfrequency is

$$\tilde{\omega}_{\mathrm{EP}} = (1.343 - 0.106\,i) \times 10^{15} \text{ rad/s}, \tag{4.16}$$

corresponding to a vacuum wavelength of 1.40 μm and a quality factor $Q = \mathrm{Re}(\tilde{\omega}_{\mathrm{EP}})/(2|\,\mathrm{Im}(\tilde{\omega}_{\mathrm{EP}})|) \simeq 6$.

The checks of Table 4.5 address the ways in which a zero of D could fail to be an exceptional point. The coupling $|K|$ is finite, so the degeneracy is not the trivial one. The Jacobian of $(\mathrm{Re}(D), \mathrm{Im}(D))$ is non-singular, so the two loci cross transversally and the exceptional point is an isolated point of the parameter plane, as required by the codimension argument of Section 2.4.4. The detuning lies well inside the fitted window, so the result does not rely on extrapolating the linearized parametrization.

The existence of the exceptional point is more robust than its precise location. Near d^* the functions $g(d)$ and $|\Delta\gamma(d)|$ are nearly parallel (Fig. 4.11), so that their crossing is ill-conditioned and sensitive to small changes in either.

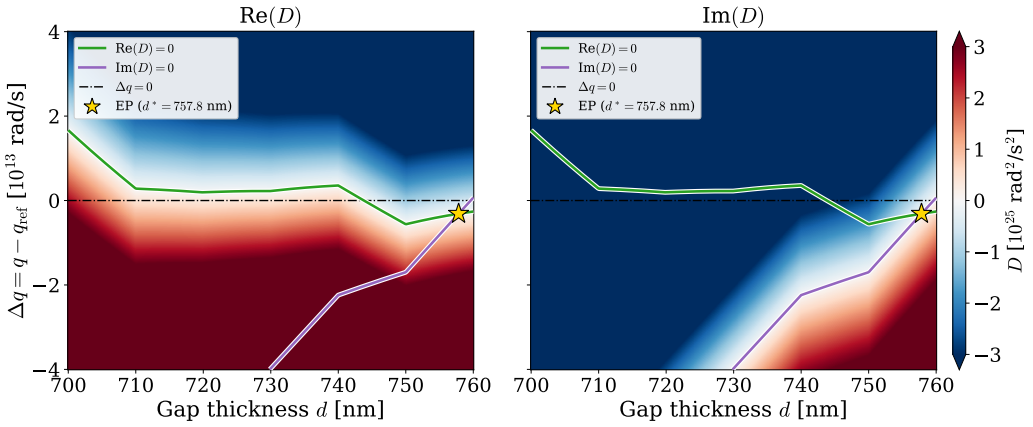


Figure 4.10: Re(D) (left) and Im(D) (right) over the plane of the gap d and the detuning $\Delta q = q - q_{\mathrm{ref}}$, from the parameters of the model $+g_1$, α interpolated linearly between the sampled gaps; the color scale is saturated at $\pm 3 \times 10^{25}$ rad^2/s^2. The zero loci Re(D) = 0 (green) and Im(D) = 0 (purple) intersect transversally at the exceptional point (star). The dash-dotted line $\Delta q = 0$ is the trajectory of Section 4.4.1, which crosses the two loci at different gaps. The kinks in the loci reflect the linear interpolation.

Quantity	Requirement at an EP	Value at $(d^*, \Delta q^*)$
$\lvert g\rvert/\lvert\Delta\gamma\rvert$	$= 1$	1.0000
$\lvert D\rvert \,/\, \lvert D\rvert_{d=300\,\mathrm{nm}}$	$\to 0$	$\sim 10^{-8}$
$\lvert K\rvert$	$\neq 0$	1.29×10^{13} rad/s
$\lvert\Delta q^*\rvert$ / half-window	$\ll 1$	0.7%
Normalized $\lvert \det J\rvert$	$\neq 0$	0.72
Phase rigidity r	$\to 0$	$< 10^{-3}$
Normalized $\lvert\langle\psi_1\rvert\psi_2\rangle\rvert$	$\to 1$	1.0000

Table 4.5: Properties of the solution of Eq. (4.14). The residual $|D|$ is limited by the numerical tolerance of the root search. J is the Jacobian of (Re(D), Im(D)) with respect to $(d, \Delta q)$, with d in nm and Δq in units of 10^{12} rad/s; the corresponding angle between the two zero loci is 46°. The phase rigidity is defined in Eq. (4.20). The first row follows from the EP condition $g = \pm\Delta\gamma$; the last two rows provide numerical checks of eigenvector coalescence. The remaining rows quantify the residual, the non-zero coupling, the detuning range and the transversality of the intersection. The value of $|\det J|$ depends on the units chosen for d and Δq, and only its being non-zero is meaningful.

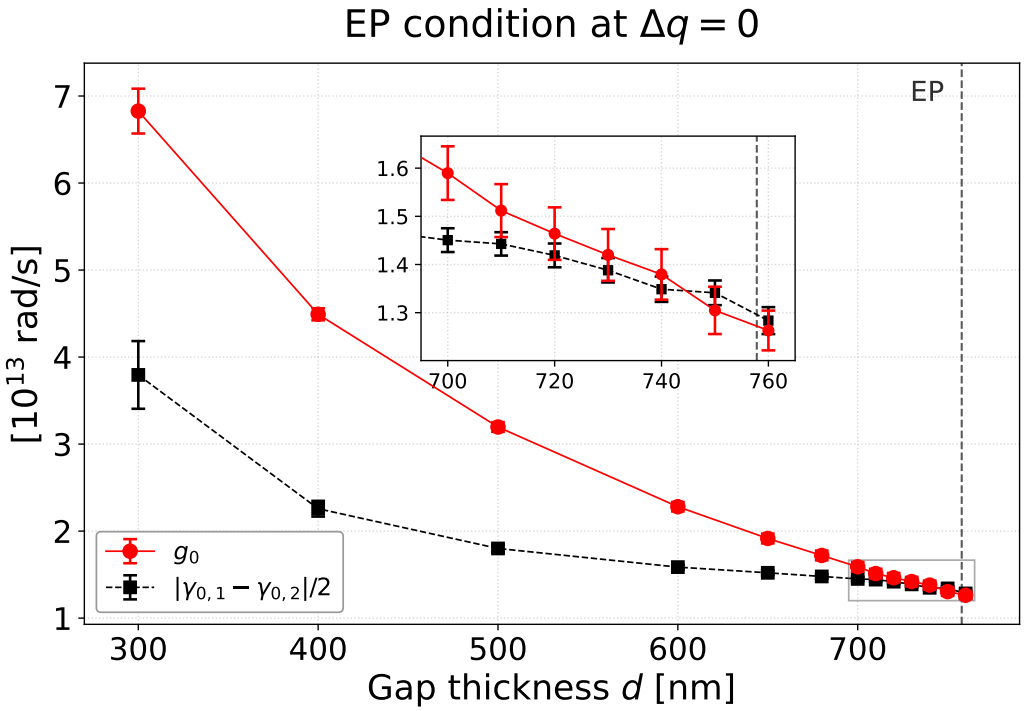


Figure 4.11: Coherent coupling g_0 (red circles) and half the difference of the decay rates, $|\gamma_{0,1}-\gamma_{0,2}|/2$ (black squares), at the reference wavevector, $\Delta q = 0$, for the model $+g_1$, α. Inset: enlargement of 700–760 nm. The two curves cross at $d \simeq 745$ nm, corresponding to the condition $\mathrm{Re}(D) = 0$ at q_{ref}. The vertical dashed line marks the EP position $d^* = 757.8$ nm obtained from the simultaneous two-parameter solution.

We estimate the resulting uncertainty by propagating the fit uncertainties of g_0, α, $\gamma_{0,1}$ and $\gamma_{0,2}$ through 400 Monte Carlo realizations, in which each parameter is perturbed independently within its standard deviation. In 69% of the realizations the exceptional point falls within the range $d \leq d_1 = 760$ nm covered by the model $+g_1,\ \alpha$; for these the median location is 756 nm with a 16–84% spread of ±3 nm, and $|\Delta q^*|$ remains below 5% of the half-window in every case. In the remaining realizations no crossing occurs within this range, so the spread quoted is conditional on $d^* \leq d_1$ and underestimates the uncertainty towards larger gaps; the independent perturbations also neglect the correlations between fitted parameters. We therefore quote $d^* = 758 \pm 3$ nm as an indicative uncertainty, and regard the existence of the exceptional point as the robust result. Its detuning is not: Δq^* is smaller than the grid step on which q_{ref} is determined, and it is set by a residual α comparable to its own uncertainty.

The proximity of d^* to the zero of α at 759 nm follows from Eq. (4.14). As $\alpha \to 0$ the dissipative coupling Γ_{12} vanishes and the second condition forces $\Delta q \to 0$: the locus $\mathrm{Im}(D) = 0$ crosses the line $\Delta q = 0$ exactly at the zero of α, and the exceptional point lies on this locus at a short distance from it (Fig. 4.10). At d^* the fitted value is $\alpha = 0.0018$, of the same order as its uncertainty. This small residual dissipative coupling sets the finite detuning of Eq. (4.15), and its uncertainty dominates that of Δq^*.

4.4.3 Signature of the Degeneracy

The localization above rests on the coalescence of the eigenvalues. An exceptional point additionally requires the coalescence of the eigenvectors, and is characterized by a non-analytic dependence of the eigenvalues on the control parameters. We verify both properties along the line $\Delta q = \Delta q^*$, which passes through the exceptional point.

For the eigenvectors we use the phase rigidity [37,38]. Let $|\psi_i\rangle$ denote the right eigenvector of the effective Hamiltonian,

$$H_{\mathrm{eff}} |\psi_i\rangle = \tilde{\omega}_i |\psi_i\rangle . \tag{4.17}$$

For the present system the Hamiltonian is complex symmetric, $H_{\mathrm{eff}}^T = H_{\mathrm{eff}}$. Moreover, in the mapping to the parametrization introduced by Heiss, the two off-diagonal couplings satisfy $\delta_1 = \delta_2$. Consequently, the corresponding left eigenvector can be written as

$$\langle \tilde{\psi}_i | = \langle \psi_i^* | = \psi_i^T , \tag{4.18}$$

so that the scalar product entering the phase rigidity is the bilinear, or c-, product [14],

$$\langle \psi_i^* | \, | \psi_i \rangle = \psi_i^T \psi_i . \tag{4.19}$$

The phase rigidity is therefore defined as

$$r_i = \frac{\left| \langle \psi_i^* | \, | \psi_i \rangle \right|}{\langle \psi_i | \, | \psi_i \rangle} = \frac{\left| \psi_i^T \psi_i \right|}{\psi_i^\dagger \psi_i} . \tag{4.20}$$

where the numerator is the bilinear product appropriate to the complex-symmetric Hamiltonian of Eq. (4.6). The phase rigidity approaches one for well separated modes and vanishes at an exceptional point, where the coalesced eigenvector becomes self-orthogonal. Along $\Delta q = \Delta q^*$ it decreases from 0.76 at $d = 650$ nm to below 10^{-3} at d^*, where the normalized overlap of the two eigenvectors reaches unity, and rises again beyond it (Fig. 4.12). Along $\Delta q = 0$ it never falls below 0.18, and equals 0.40 at 745 nm: the trajectory through the reference point does not reach the degeneracy.

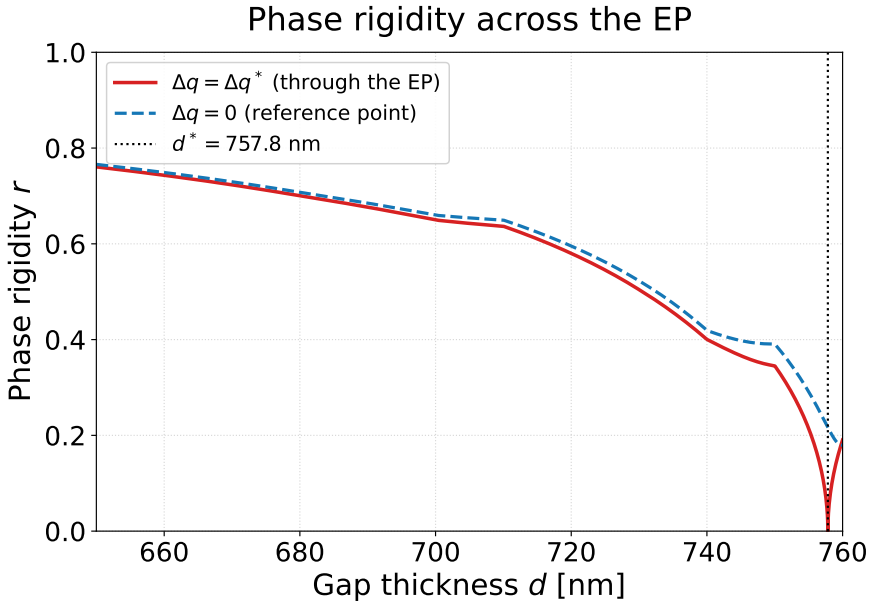


Figure 4.12: Phase rigidity r of Eq. (4.20) as a function of the gap, along the line through the exceptional point ($\Delta q = \Delta q^*$, red solid) and along the reference trajectory ($\Delta q = 0$, blue dashed). Only the former reaches $r \to 0$, at d^* (dotted line). The kinks at the sampled gaps reflect the linear interpolation of the fitted parameters.

For the eigenvalues, near a second-order exceptional point the separation of Eq. (2.19) vanishes as the square root of the distance from the singularity, because D has a simple zero there; where D has a double zero, as at an ordinary Hermitian degeneracy, the separation vanishes linearly instead. Fitting $|\tilde{\omega}_+ - \tilde{\omega}_-| \propto |d - d^*|^p$ along $\Delta q = \Delta q^*$, within the interpolation interval 750–760 nm that contains d^*, we obtain

$$p = 0.505 \;\; (d < d^*), \qquad p = 0.498 \;\; (d > d^*), \tag{4.21}$$

in agreement with the value $1/2$ from both sides. This confirms that D has a simple zero at d^*, consistently with the non-singular Jacobian of Table 4.5. Windows extending across the sampled gaps at 740 and 750 nm give exponents between 0.41 and 0.52, because the linear interpolation introduces discontinuities in the derivatives of the parameters at these nodes; the local value is the meaningful one.

For comparison, the same power-law fit along the reference trajectory $\Delta q = 0$, with the position of the apparent singularity left as a free parameter, gives $p = 0.49$ and places the fitted singularity at 756 nm. This apparent square-root scaling is therefore consistent with the nearby exceptional-point structure, but the reference trajectory does not pass exactly through the EP identified in Eq. (4.15); fixing the singularity at 745 nm instead gives $p = 0.35$. The exact EP identification is therefore based on the two-parameter localization together with the eigenvector and discriminant checks.

4.5 Discussion

The leaky-mode analysis reveals how the complex eigenvalues evolve as the gap is increased. The coherent coupling decreases exponentially with the separation, with a decay length close to the evanescent decay length in the gap over the range where the coupling is well resolved. In contrast, the half-difference of the radiative decay rates varies more slowly, and the two quantities become equal near $d \simeq 745$ nm along the reference trajectory. The dissipative coupling, defined relative to the chosen reference point, decreases and vanishes close to the same region.

The reference trajectory $\Delta q = 0$ does not satisfy the two EP conditions at the same gap: $\mathrm{Re}(D)$ and $\mathrm{Im}(D)$ vanish 14 nm apart. This mismatch results from imposing zero real detuning at q_{ref}, whereas the general EP condition requires the real detuning to balance the dissipative coupling. Allowing the in-plane wavevector to vary as a second control parameter brings the two conditions together at $d^* = 758 \pm 3$ nm, with $|\Delta q^*|$ much smaller than the fitted-window half-width. Within the effective Hamiltonian, the eigenvalues and

eigenvectors coalesce, the two zero loci of the discriminant intersect transversally, and the eigenvalue separation follows the square-root law expected at a second-order exceptional point. The second control parameter is already present in the problem through k_x and can be varied experimentally through the angle of incidence.

The present identification remains model dependent in two respects. First, the EP is located from the fitted effective Hamiltonian rather than directly from the full TMM problem. Second, the separation of the coupling into coherent and dissipative contributions depends on the reference-point convention and becomes progressively less identifiable in the weak-coupling regime. A direct TMM verification would instead locate a double zero of T_{22}, that is, a double pole of the transmission coefficient, and identify the EP. In terms of the modal condition, this corresponds to a double zero [39],

$$T_{22}(\tilde{\omega}_{\mathrm{EP}}, k_x^{\mathrm{EP}}, d_{\mathrm{EP}}) = 0, \qquad \left.\frac{\partial T_{22}}{\partial \tilde{\omega}}\right|_{\mathrm{EP}} = 0. \tag{4.22}$$

Locating such a double zero at the corresponding wavevector and on a denser gap sweep around d^* would provide an independent confirmation of the exceptional point without relying on the two-mode reduction.

The apparent non-monotonic behavior of the dissipative coupling in the weak-coupling regime cannot yet be assigned to a specific physical mechanism. A wider gap sweep, combined with a treatment of the phase accumulated in the radiative channels, would be needed to determine whether the observed rise and fall is part of an oscillatory dependence. Extending the analysis to TM polarization and to additional interacting mode pairs would further test whether the mechanisms identified here persist beyond the specific TE two-mode system studied in this thesis.

Chapter 5

Conclusions

This thesis followed a pair of coupled planar waveguides from the guided regime to a non-Hermitian exceptional-point condition. The asymmetry of the two waveguides, in both refractive index and thickness, is essential for the EP mechanism studied here because it allows the two modes to acquire different radiative decay rates. A single transfer matrix solver, with a root search on the real frequency axis for guided modes and in the complex plane for leaky modes, provided the computational framework for the analysis throughout the thesis.

In the guided regime, the two isolated-waveguide dispersions hybridize into symmetric- and antisymmetric-like supermodes across an avoided crossing, and this behavior was captured quantitatively by fitting the TMM data to a 2×2 Hermitian effective Hamiltonian. The extracted coherent coupling $g(d)$ decays exponentially with the gap thickness, with a decay length $L_d = 149.9 \pm 0.7$ nm, within 1% of the evanescent decay length in the gap, $1/\kappa_{\text{gap}} = 150.7$ nm, as expected from the evanescent-field-overlap mechanism introduced in Chapter 2.

Above the cladding light line, the structure was modified so that the modes remained evanescently coupled across the gap while radiating into the claddings at different rates. The complex TMM eigenvalues were then fitted to non-Hermitian effective Hamiltonians containing coherent and dissipative coupling. At the representative separation $d = 600$ nm, introducing the dissipative coupling reduces the normalized residual from $\chi = 0.217$ in the baseline model to $\chi = 0.060$, while allowing a wavevector-dependent coherent coupling alone gives $\chi = 0.195$. Releasing both g_1 and α gives $\chi = 0.047$. Allowing q_{ref} to vary does not improve the residual further but makes the parameters partially degenerate, showing that q_{ref}, g_1, and α cannot be determined independently from the same fit. We therefore adopt the ten-parameter model with q_{ref} fixed at the minimum-splitting point, and interpret α relative to this convention.

The coherent coupling decays exponentially with the gap, with a decay length close to the evanescent decay length in the gap, confirming its near-field origin. The dissipative coupling decreases from 0.19 at 300 nm and vanishes near 760 nm; in the weak-coupling regime its magnitude apparently rises again to a secondary maximum.

The balance between the coherent coupling and the half-difference of the radiative decay rates drives the system from strong to weak coupling. Along the reference trajectory $\Delta q = 0$, the two conditions associated with $D = 0$ are satisfied at gaps separated by 14 nm, because the real detuning is forced to vanish at the chosen reference point while the general EP condition allows a finite detuning set by the dissipative coupling. Treating the in-plane wavevector as a second independent control parameter, the two conditions are satisfied simultaneously at $d^* = 758 \pm 3$ nm, close to phase matching. At this point, the eigenvalues and eigenvectors coalesce, the phase rigidity falls below 10^{-3}, the two zero loci of the discriminant intersect transversally, and the eigenvalue separation follows the square-root law expected for a second-order exceptional point.

These results identify an exceptional point of the fitted two-mode effective Hamiltonian in a fully passive photonic structure. In this system, the non-Hermiticity is supplied by radiative losses and the EP is reached by varying two parameters already present in the problem: the gap thickness and the in-plane wavevector, the latter being tunable experimentally through the angle of incidence.

The analysis presented here has three limitations. First, the position of the exceptional point is known only to within a few nanometers: near d^*, the coherent coupling and the half-difference of the decay rates are nearly parallel functions of the gap, so their crossing is ill-conditioned. Second, the signatures of the degeneracy in Section 4.4 were established on the fitted effective Hamiltonian. A direct TMM verification, by locating a double zero of T_{22}, that is, a double pole of the transmission coefficient, at the corresponding wavevector and on a denser gap sweep around d^*, would make the identification independent of the two-mode reduction. Third, the resonances are broad, with $Q \simeq 6$, so the degeneracy would not be spectrally resolved in a simple reflection measurement.

The apparent non-monotonic behavior of the dissipative coupling in the weak-coupling regime remains unresolved; a wider gap sweep combined with a treatment of the phase accumulated in the radiative channels would be needed to determine its origin. Extending the analysis to TM polarization and to additional interacting mode pairs would further test whether the mechanisms identified here persist beyond the specific TE two-mode system studied in this thesis.

Appendix A

Derivation of the Exceptional Point Condition and Jordan Block Structure

This appendix presents, in full, the derivation summarized in Section 2.4.5 of the exceptional point (EP) condition and of the associated Jordan block structure, starting from the parameter-dependent Hamiltonian introduced by Heiss [14].

A.1 Eigenvalues of the Parametric Hamiltonian

Consider the Heiss Hamiltonian

$$H(\lambda) = H_0 + \lambda V = \begin{pmatrix} \tilde{\omega}_1 + \lambda\epsilon_1 & \lambda\delta_1 \\ \lambda\delta_2 & \tilde{\omega}_2 + \lambda\epsilon_2 \end{pmatrix}. \tag{A.1}$$

For a general 2×2 matrix $M = \begin{pmatrix} a & b \\ c & d \end{pmatrix}$, the characteristic equation $x^2 - (a+d)x + (ad - bc) = 0$ gives the eigenvalues

$$x_\pm = \frac{a+d}{2} \pm \sqrt{\left(\frac{a-d}{2}\right)^2 + bc}. \tag{A.2}$$

Identifying $a = \tilde{\omega}_1 + \lambda\epsilon_1$, $b = \lambda\delta_1$, $c = \lambda\delta_2$, $d = \tilde{\omega}_2 + \lambda\epsilon_2$, and introducing the compact notation

$$\Delta_0 \equiv \tilde{\omega}_1 - \tilde{\omega}_2, \qquad \epsilon_d \equiv \epsilon_1 - \epsilon_2, \tag{A.3}$$

the term under the square root in Eq. (A.2) becomes

$$R(\lambda) = \left(\frac{\Delta_0 + \lambda\epsilon_d}{2}\right)^2 + \lambda^2\delta_1\delta_2. \tag{A.4}$$

A.2 The Exceptional Point Condition

An EP occurs when the two eigenvalues of $H(\lambda)$ coalesce, i.e. when $R(\lambda) = 0$. Multiplying Eq. (A.4) by 4 and expanding,

$$(\Delta_0+\lambda\epsilon_d)^2+4\lambda^2\delta_1\delta_2 = 0 \quad\Longrightarrow\quad \lambda^2\left(\epsilon_d^2 + 4\delta_1\delta_2\right)+2\Delta_0\epsilon_d\,\lambda+\Delta_0^2 = 0, \tag{A.5}$$

which is a quadratic equation in λ. Its discriminant is

$$\begin{aligned}(2\Delta_0\epsilon_d)^2 - 4\Delta_0^2\left(\epsilon_d^2 + 4\delta_1\delta_2\right) &= 4\Delta_0^2\epsilon_d^2 - 4\Delta_0^2\epsilon_d^2 - 16\Delta_0^2\delta_1\delta_2 \\ &= -16\,\Delta_0^2\,\delta_1\delta_2,\end{aligned} \tag{A.6}$$

so that Eq. (A.5) admits the two roots

$$\lambda = \frac{-2\Delta_0\epsilon_d \pm 4i\,\Delta_0\sqrt{\delta_1\delta_2}}{2\left(\epsilon_d^2 + 4\delta_1\delta_2\right)} = \frac{\Delta_0\left[-\epsilon_d \pm 2i\sqrt{\delta_1\delta_2}\,\right]}{\epsilon_d^2 + 4\delta_1\delta_2}. \tag{A.7}$$

The denominator factors as a difference of squares, since $\left(2i\sqrt{\delta_1\delta_2}\right)^2 = -4\delta_1\delta_2$:

$$\epsilon_d^2 + 4\delta_1\delta_2 = \left(\epsilon_d - 2i\sqrt{\delta_1\delta_2}\right)\left(\epsilon_d + 2i\sqrt{\delta_1\delta_2}\right). \tag{A.8}$$

Each numerator in Eq. (A.7) cancels one of these two factors, leaving

$$\lambda_{\mathrm{EP}}^{(\pm)} = \frac{-\Delta_0}{\epsilon_d \pm 2i\sqrt{\delta_1\delta_2}}. \tag{A.9}$$

Multiplying numerator and denominator by i (using $i^2 = -1$) casts this in the form used in the main text:

$$\boxed{\lambda_{\mathrm{EP}}^{(\pm)} = \frac{-i(\tilde{\omega}_1 - \tilde{\omega}_2)}{i(\epsilon_1 - \epsilon_2) \mp 2\sqrt{\delta_1\delta_2}}.} \tag{A.10}$$

The two roots $\lambda_{\mathrm{EP}}^{(\pm)}$ are, in general, distinct points in the complex λ-plane, each marking an exceptional point. They are related by the exchange of mode

labels ($1 \leftrightarrow 2$), which sends $\Delta_0 \to -\Delta_0$ and $\epsilon_d \to -\epsilon_d$ while leaving $\delta_1\delta_2$ unchanged; substituting these into Eq. (A.9) gives

$$\frac{-(-\Delta_0)}{-\epsilon_d \pm 2i\sqrt{\delta_1\delta_2}} = \frac{-\Delta_0}{\epsilon_d \mp 2i\sqrt{\delta_1\delta_2}} = \lambda_{\mathrm{EP}}^{(\mp)}, \tag{A.11}$$

so that under this exchange $\lambda_{\mathrm{EP}}^{(+)}$ and $\lambda_{\mathrm{EP}}^{(-)}$ swap into one another. This is the precise sense in which the two branches describe the same physical exceptional point.

A.3 Specialization to the Two-Waveguide System

Setting $\epsilon_1 = \epsilon_2 = 0$ and $\delta_1 = \delta_2 = \delta$ in Eq. (A.10) gives

$$\lambda_{\mathrm{EP}} = \frac{-i(\tilde{\omega}_1 - \tilde{\omega}_2)}{\mp 2\delta} = \pm\frac{i(\tilde{\omega}_1 - \tilde{\omega}_2)}{2\delta}. \tag{A.12}$$

Imposing $\lambda_{\mathrm{EP}} = 1$ (the physical Hamiltonian) and solving for δ,

$$\delta = -\frac{i}{2}(\tilde{\omega}_1 - \tilde{\omega}_2). \tag{A.13}$$

Substituting $\tilde{\omega}_k = \omega_k - i\gamma_k$,

$$\begin{aligned}\delta &= -\frac{i}{2}\left[(\omega_1 - \omega_2) - i(\gamma_1 - \gamma_2)\right] \\ &= -\frac{\gamma_1 - \gamma_2}{2} - i\,\frac{\omega_1 - \omega_2}{2}.\end{aligned} \tag{A.14}$$

Equating the real and imaginary parts of Eq. (A.14) to the physical definition $\delta = g - i\alpha\sqrt{\gamma_1\gamma_2}$ yields the explicit EP conditions

$$g = -\frac{\gamma_1 - \gamma_2}{2}, \qquad \alpha\sqrt{\gamma_1\gamma_2} = \frac{\omega_1 - \omega_2}{2}, \qquad \text{i.e.} \qquad |g| = \frac{|\gamma_1 - \gamma_2|}{2}. \tag{A.15}$$

A.4 Verification of the Jordan Block Structure

At the EP, $\mathbf{H}_{\mathrm{eff}} = \begin{pmatrix} \tilde{\omega}_1 & \delta \\ \delta & \tilde{\omega}_2 \end{pmatrix}$ with δ given by Eq. (A.14). For a nontrivial exceptional point, $\delta \neq 0$; otherwise the Hamiltonian reduces to a scalar multiple of the identity and the degeneracy is not exceptional. Under this condition, the similarity transformation

$$S = \begin{pmatrix} i & \frac{1}{\delta} \\ 1 & 0 \end{pmatrix}, \qquad S^{-1} = \begin{pmatrix} 0 & 1 \\ \delta & -i\delta \end{pmatrix} \tag{A.16}$$

brings $\mathbf{H}_{\text{eff}}$ to Jordan normal form. First,

$$\mathbf{H}_{\text{eff}} S = \begin{pmatrix} i\tilde{\omega}_1 + \delta & \tilde{\omega}_1/\delta \\ i\delta + \tilde{\omega}_2 & 1 \end{pmatrix}. \tag{A.17}$$

Left-multiplying by S^{-1},

$$S^{-1}\mathbf{H}_{\text{eff}} S = \begin{pmatrix} i\delta + \tilde{\omega}_2 & 1 \\ i\delta(\tilde{\omega}_1 - \tilde{\omega}_2) + 2\delta^2 & \tilde{\omega}_1 - i\delta \end{pmatrix}. \tag{A.18}$$

For this to equal the Jordan block $\begin{pmatrix} \tilde{\omega}_{\text{EP}} & 1 \\ 0 & \tilde{\omega}_{\text{EP}} \end{pmatrix}$, two conditions must hold:

$$\text{(a)} \quad i\delta + \tilde{\omega}_2 = \tilde{\omega}_1 - i\delta \qquad \text{(equal diagonal entries)}, \tag{A.19}$$

$$\text{(b)} \quad i\delta(\tilde{\omega}_1 - \tilde{\omega}_2) + 2\delta^2 = 0 \qquad \text{(vanishing (2,1) entry)}. \tag{A.20}$$

Condition (a) gives $2i\delta = \tilde{\omega}_1 - \tilde{\omega}_2$, i.e. $\delta = -i(\tilde{\omega}_1 - \tilde{\omega}_2)/2$ — precisely the EP condition of Eq. (A.14). Substituting $\tilde{\omega}_1 - \tilde{\omega}_2 = 2i\delta$ (from condition (a)) into condition (b),

$$i\delta(2i\delta) + 2\delta^2 = -2\delta^2 + 2\delta^2 = 0, \tag{A.21}$$

which is satisfied identically. Condition (b) therefore does not impose any additional constraint beyond (a): a single condition on the complex coupling δ is both necessary and sufficient for $\mathbf{H}_{\text{eff}}$ to reduce to a Jordan block. Since δ is complex, this single condition is equivalent to two independent real conditions, $\text{Re}(D) = \text{Im}(D) = 0$ (cf. Section 2.4.2), so that a second-order EP generically has codimension two in a real parameter space — consistent with the two-parameter (d, k_x) search of Section 2.4.4.

Finally, the coalesced eigenvalue follows from the diagonal entry of Eq. (A.18) evaluated at the EP:

$$\tilde{\omega}_{\text{EP}} = i\delta + \tilde{\omega}_2 = \frac{\tilde{\omega}_1 - \tilde{\omega}_2}{2} + \tilde{\omega}_2 = \frac{\tilde{\omega}_1 + \tilde{\omega}_2}{2} = \frac{(\omega_1 - i\gamma_1) + (\omega_2 - i\gamma_2)}{2}, \tag{A.22}$$

which reproduces the result quoted in Section 2.4.5.

Appendix B

Implementation of the Numerical Solver

This appendix documents the solver written for this thesis. Its purpose is to make the numerical results reproducible and to expose the points at which a choice had to be made: the branch of the complex square root, the strategy used to continue a root from one wavevector to the next, the criterion by which two eigenvalue branches are labeled, and the way the effective Hamiltonian is fitted.

B.1 Overview and Structure

The solver is written in Python and relies only on NumPy [40] for array algebra, on five SciPy [41] routines (`signal.find_peaks`, `optimize.minimize_scalar`, `optimize.newton`, `optimize.brentq` and `optimize.curve_fit`) and on Matplotlib [42] for the figures. No photonics or electromagnetic library is used: the transfer matrices, the root search in the complex plane and the branch tracking are implemented from scratch. The listings below are simplified excerpts of the code: comments have been translated and shortened, and auxiliary code has been omitted.

The code is organized in four stages, executed in sequence:

1. **Transfer matrix.** Given a layer stack, a frequency ω and a longitudinal wavevector k_x, the global 2×2 matrix $\mathbf{T}(\omega, k_x)$ is assembled (Section B.2).

2. **Mode search.** The modal condition $T_{22} = 0$ is solved for ω at fixed k_x, on the real axis for guided modes (Section B.3) and in the lower complex half-plane for leaky modes (Section B.4).

3. **Hamiltonian fit.** The two complex branches are fitted to the effective non-Hermitian Hamiltonian of Eq. (4.6), with the parametrization selected according to the gap (Section B.6).

4. **Exceptional Point analysis.** The discriminant is evaluated over the plane $(d, \Delta q)$ and its zero loci are intersected (Section B.7).

The stages communicate through plain-text `.out` files rather than through variables held in memory. Each file carries a header recording the refractive indices, the layer thicknesses and the wavevector grid used to produce it, so that the origin of any dataset can be traced from the file itself. This design has a practical motivation: the mode search over a full gap sweep takes far longer than the fitting and the exceptional point analysis, so separating them allows the analysis to be repeated without recomputing the modes. All results reported in Chapters 3 and 4 are obtained from these intermediate files.

B.2 Transfer Matrix Construction

Within each homogeneous layer the transverse wavevector follows from the dispersion relation of Eq. (4.2). Its evaluation is the first point at which a choice is required, because the argument of the square root changes sign between the guided and the leaky regime, and because ω itself becomes complex above the light line.

```
def calc_kz(n, omega, kx):
    """
    Transverse wavevector in a layer of index n, for a
       given omega and kx.
    For real omega and kx, a positive argument
       corresponds to propagating waves and a negative
       argument to evanescent waves; in the leaky
       regime the argument is generally complex. np.lib
       .scimath.sqrt returns the principal
    branch in both cases, so that no explicit case
       distinction is needed.
    """
    k0 = omega / c
    return np.lib.scimath.sqrt((n * k0)**2 - kx**2)
```

Listing B.1: Transverse wavevector: the branch of the complex square root is fixed by the choice of square-root function.

We use `np.lib.scimath.sqrt` because `np.sqrt` returns `nan` for a negative real argument, whereas `scimath.sqrt` promotes the argument to complex and returns the principal branch. For a negative real argument this gives

$k_z = +i|k_z|$, which is the branch convention used throughout the calculation. The physical guided or outgoing-wave boundary condition is then imposed separately through the modal condition $A_1 = B_5 = 0$: in the guided regime this removes the exponentially growing solutions in the claddings, while in the leaky regime it removes the incoming waves and retains the outgoing ones. The same square-root convention is therefore used in both regimes without an explicit switch in the code.

The interface and propagation matrices follow directly from the continuity of E_y and dE_y/dz across each boundary.

```
def T_interface(kz_j, kz_jp1):
    """
    Transfer matrix across the interface from layer j
       to layer j+1, obtained
    by imposing continuity of the tangential field and
       of its derivative.
    """
    m11 = kz_jp1 + kz_j
    m12 = kz_jp1 - kz_j
    m21 = kz_jp1 - kz_j
    m22 = kz_jp1 + kz_j
    return (1 / (2 * kz_jp1)) * np.array([[m11, m12], [
       m21, m22]],
                                         dtype=complex
                                            )

def T_propagation(kz_j, d_j):
    """Phase accumulated across a layer of thickness
       d_j."""
    arg = 1j * kz_j * d_j
    return np.array([[np.exp(arg), 0], [0, np.exp(-arg)
       ]], dtype=complex)
```

Listing B.2: Interface and propagation matrices for TE polarization.

The matrices are multiplied in the order in which they are generated in the code, from the first interface to the last. This produces the transpose of the product written in Eq. (3.6). Since every individual interface and propagation matrix is symmetric, transposition reverses the order of the product without changing the T_{22} element. The modal condition $T_{22} = 0$ is therefore unchanged. Assembling it requires some care, because the propagation matrix contains $e^{\pm ik_z d}$ and the exponent becomes large and real whenever the field is strongly evanescent in a thick layer. For a sufficiently large gap the argument exceeds the range of double precision, the exponential overflows, and the product propagates `inf` and `nan` values into every subsequent matrix. The root search would then receive meaningless values with no indication that

anything had gone wrong.

The solution adopted is to detect the condition before it occurs and return a sentinel matrix with very large entries, which the root search discards as a failed evaluation. The threshold is $|\mathrm{Re}(ik_z d)| > 500$, safely below the overflow limit of a double.

```
def calc_total_T_matrix(omega, kx):
    """
    Global transfer matrix of the stack, assembled as an alternating product
    of interface and propagation matrices. The semi-infinite outer layers
    carry no propagation term.
    """
    # Guard: reject unphysical frequencies before any computation.
    if np.abs(omega) > 1e18 or np.isnan(np.abs(omega)):
        return np.array([[1e50, 1e50], [1e50, 1e50]], dtype=complex)

    kz = np.array([calc_kz(n, omega, kx) for n in n_layers], dtype=complex)

    matrices = []
    for i in range(len(n_layers) - 1):
        matrices.append(T_interface(kz[i], kz[i+1]))
        if i < len(n_layers) - 2:
            # Guard: exp(500) is close to the double-precision limit. Beyond
            # it the propagation matrix overflows, so the evaluation is abandoned instead.
            arg = 1j * kz[i+1] * d_layers[i+1]
            if np.abs(np.real(arg)) > 500:
                return np.array([[1e50, 1e50], [1e50, 1e50]], dtype=complex)
            matrices.append(T_propagation(kz[i+1], d_layers[i+1]))

    res = np.eye(2, dtype=complex)
    for M in matrices:
        res = res @ M
        if np.any(np.isnan(res)) or np.any(np.isinf(np.abs(res))):
            return np.array([[1e50, 1e50], [1e50, 1e50]], dtype=complex)
    return res
```

Listing B.3: Assembly of the global transfer matrix, with guards against exponential overflow.

Returning a large finite value rather than raising an exception keeps the function total: every call returns a matrix, and the minimization and root-finding routines treat the sentinel as a point of very large residual and move away from it. In the calculations of this thesis $|\mathrm{Re}(ik_z d)|$ never exceeds a few tens, so the guard is not triggered; it is kept as a safeguard for thicker layers.

B.3 Guided Modes: Real Root Search

Below the light line the eigenfrequencies are real, and the modal condition reduces to finding the zeros of $|T_{22}(\omega)|$ on a finite interval. The difficulty is not the root finding itself but the localization of the roots: $|T_{22}|$ varies over many orders of magnitude and the zeros are extremely narrow, so a uniform scan can miss them unless a prohibitively dense grid is used.

The pipeline described in Section 3.2.3 addresses this in three stages. A coarse scan of 1000 points is performed between the two light lines, and the quantity $-\log_{10}|T_{22}|$ is examined instead of $|T_{22}|$ itself: on a logarithmic scale a narrow zero becomes a tall, well-separated peak that `find_peaks` can locate reliably. Each peak is then refined by a bounded minimization over a bracket whose width scales with the frequency, and the resulting minimum seeds a secant iteration (`optimize.newton` without an analytic derivative) on $|T_{22}|$.

```
        # Coarse scan between the two light lines.
        om_min = c * kx / n_core_max
        om_max = c * kx / n_clad_min
        omega_scan = np.linspace(om_min * 0.99, om_max
            * 1.01, 1000)

        # A narrow zero of |T22| becomes a tall peak of
            -log|T22|, which
        # find_peaks can localize reliably. The offset
            1e-20 avoids log(0).
        t22_vals = np.array([np.abs(target_function(om,
            kx))
                             for om in omega_scan])
        log_data = -np.log10(t22_vals + 1e-20)

        prom = 1e-6 if kx > 2e7 else 1e-5
        peaks, _ = find_peaks(log_data, prominence=prom
            , distance=8)

        refined_guesses = []
        for p in peaks:
            g = omega_scan[p]
            # Bracket width scaled to the frequency,
                clipped to a sensible
```

```
            # range so that adjacent modes are not
               captured by the same
            # minimization.
            delta = min(max(5e12, 0.01 * g), 1e14)
            res = minimize_scalar(lambda om: np.abs(
               target_function(om, kx)),
                                  bounds=(g - delta, g
                                     + delta),
                                  method='bounded')

            # Near cutoff the zero is shallower, so the
                acceptance threshold
            # on the residual is relaxed within 5% of
               the light line.
            om_light = (c * kx) / n_clad_min
            tol_min = 1e-2 if abs(res.x - om_light) /
               om_light < 0.05 else 1e-3

            if res.success and res.fun < tol_min:
                refined_guesses.append(res.x)
```

Listing B.4: Peak localization and bracket refinement in the guided regime.

The refined guesses are then passed to the secant iteration, with a bounded minimization as fallback when the iteration fails to converge. A root returned by the secant iteration is accepted if $|T_{22}| < 0.1$ (0.5 for $k_x > 2 \times 10^7$ rad/m); the fallback minimization, over $\pm 5 \times 10^{13}$ rad/s around the starting point, is accepted with the same threshold of 0.1. Near a simple real root $|T_{22}|$ is locally proportional to $|\omega - \omega_m|$, so the secant iteration converges even though $|T_{22}|$ does not change sign. Roots closer than $10^{-4}\omega_{\max}$ are merged, and the surviving list is carried over to the next wavevector as an additional set of starting points, which keeps a branch from being lost where its peak temporarily falls below the prominence threshold.

B.4 Leaky Modes: Complex Root Search

Above the light line the eigenfrequencies acquire a negative imaginary part and the search must be conducted in two dimensions. The strategy adopted here differs substantially from the guided case: a two-dimensional analogue of the coarse scan would be prohibitively expensive, and the peaks it would have to resolve are not peaks of a real function but zeros of a complex one. The search is therefore replaced by continuation, and it needs a root-finding routine that operates directly on complex arguments.

B.4.1 Complex Newton–Raphson Iteration

The SciPy routine `optimize.newton` also accepts complex arguments; an explicit implementation is used here to keep the convergence criteria and the handling of failures under control. The derivative is not available in closed form, since T_{22} is the product of seven matrices whose entries depend on ω through several square roots and exponentials, and it is therefore evaluated by a central finite difference.

```
def complex_newton(f, x0, kx, tol=1e-6, maxiter=50):
    """
    Newton-Raphson iteration for a complex-valued function of a complex
    variable. The derivative is evaluated by a central finite difference,
    since T22 is not available in closed form.
    """
    om = complex(x0)
    for _ in range(maxiter):
        f_val = f(om, kx)

        # Adaptive step: relative to |omega| where that is meaningful, with
        # an absolute floor to avoid cancellation when omega is small. With
        # omega ~ 1e15 this gives h ~ 1e7, small against the scale of the
        # root and large enough to stay above double-precision noise.
        h = max(1e-12, 1e-8 * abs(om))
        df = (f(om + h, kx) - f(om - h, kx)) / (2 * h)
        # A vanishing or undefined derivative means the iteration has left
        # the basin of attraction: abandon rather than diverge.
        if abs(df) < 1e-20 or np.isnan(abs(df)):
            return None
        # Convergence on the residual.
        if abs(f_val) < 1e-8:
            return om

        om_new = om - f_val / df
        # Convergence on the increment.
        if abs(om_new - om) < tol:
            return om_new
        om = om_new
    return None
```

Listing B.5: Newton–Raphson iteration generalized to complex arguments.

A fixed absolute step would be either too large near a sharp root or, at $\omega \sim 10^{15}$ rad/s, so small relative to the argument that the difference $f(\omega + h) - f(\omega - h)$ would be dominated by round-off. The adaptive form $h = \max(10^{-12}, 10^{-8}|\omega|)$ gives $h \sim 10^{7}$ rad/s at the frequencies of interest, eight orders of magnitude below the root and eight above the precision of a double, which places it comfortably between the two failure modes. The absolute floor only becomes active if the iteration wanders towards the origin, where it prevents a step of exactly zero. In practice the iteration always stops on the residual criterion: at $\omega \sim 10^{15}$ rad/s the absolute increment tolerance of 10^{-6} rad/s is below the resolution of a double and is never met.

The routine returns `None` rather than an approximate root whenever it fails. In the continuation described below a failed attempt is retried from a different starting point, and an approximate root accepted silently would corrupt the branch from that wavevector onwards.

B.4.2 Initialization and Continuation

The continuation is seeded from guided modes close to the cladding light line. Near the light line, the corresponding leaky root has a real part close to the guided-mode frequency and a small negative imaginary part. The guided frequency can therefore be used as a natural initial estimate for the complex root by adding a small displacement into the lower half-plane.

```
        # Guided modes within 15% of the light line are close enough to the
        # leaky branch to serve as seeds.
        mask = (guided_kx >= kx * 0.8) & (guided_kx <= kx * 1.2)

        for om_g in guided_om[mask]:
            if abs(om_g - om_light) / om_light < 15e-2:

                # Displace into the dissipative half-plane by a small
                # fraction of the distance from the light line.
                delta = om_g - om_light
                guess = complex(om_g, -1e-2 * abs(delta))

                om_opt = complex_newton(get_T22, guess, kx)

                if om_opt is not None:
                    residual = abs(get_T22(om_opt, kx))
```

```
                    # Accept only converged roots in the lower half-plane and
                    # inside the leaky window.
                    if (residual < 1e-8 and
                        om_opt.imag < 0 and
                        om_opt.real > om_light and
                        om_opt.real < om_max_limit):
                        current_modes.append(om_opt)
```

Listing B.6: Seeding the complex search from the guided modes near the light line.

Once a root has been found, the sweep proceeds by using it as the starting point for the adjacent wavevector. The wavevector array is traversed in reverse order, from the light line towards smaller k_x, because that is the direction in which the branch is born.

Continuation with a single starting point fails wherever the branch moves quickly, in particular as a mode approaches cutoff and its decay rate grows by orders of magnitude over a short interval in k_x. Rather than reducing the step size everywhere, which would slow the whole sweep for the sake of a narrow region, the iteration is attempted from several starting points in turn and every distinct root that passes the filters below is retained.

```
        for prev_om in previous_modes:
            # Five starting points, tried in order. The first is the previous
            # root; the next three rescale it towards the origin at increasing rates; the last is a fixed
            # guess deep in the dissipative region, which recovers modes
            # collapsing towards cutoff.
            guesses = [
                prev_om,                        # same point
                prev_om * 0.9,                  # slow descent
                prev_om * 0.75,                 # faster descent
                prev_om * 0.5,                  # steep descent
                complex(prev_om.real, -1e14)    # cutoff fallback
            ]

            for guess in guesses:
                om_opt = complex_newton(get_T22, guess, kx)
```

```
                if om_opt is None:
                    continue

                residual = abs(get_T22(om_opt, kx))
                if (residual < 1e-8 and
                    om_opt.imag < 0 and
                    om_opt.real > om_light and
                    om_opt.real < om_max_limit):
                    if not any(abs(om_opt - m) / abs(
                        om_opt) < 1e-4
                                for m in current_modes):
                        current_modes.append(om_opt)
```

Listing B.7: Continuation with multiple starting points.

The first four guesses scale the previous root by decreasing factors, moving the starting point towards the origin along the ray through the previous solution, that is, at constant quality factor; they recover branches whose frequency drops quickly as k_x is reduced. The fifth keeps the real part and places the imaginary part at -10^{14} rad/s, a value chosen to lie within the range of decay rates the structure actually produces (Section 4.3.1); it recovers modes whose losses grow too abruptly for the scaled guesses to follow.

The accepted roots must satisfy $|T_{22}| < 10^{-8}$, have a real part between the cladding light line and the upper limit of the search window, and lie in the lower half-plane: a positive imaginary part would describe a mode gaining energy in a passive structure and can only be a spurious root of the analytic continuation. A root is also discarded if $|\mathrm{Im}\,\tilde{\omega}| > 10\,|\mathrm{Re}\,\tilde{\omega}|$, which removes solutions so heavily damped that they no longer correspond to a resonance. Finally, roots closer than 10^{-4} in relative terms are merged, since the five starting points frequently converge to the same solution.

B.5 Branch Tracking

The mode search returns, at each wavevector, an unordered set of complex eigenfrequencies. Assigning them to continuous branches is a separate problem, and near an exceptional point it is the delicate one.

The natural ordering by real part fails exactly where the analysis of Chapter 4 is carried out. In the strong-coupling regime the real parts anticross, so ordering by real part keeps each branch intact; but beyond the transition of Section 4.3.4 the real parts cross, and an ordering by real part would swap the two branches at the crossing, producing a discontinuity in the imaginary parts that is an artifact of the labeling. The same problem affects the continuation

itself, as noted in Section 4.1.2: where the two roots approach each other, the iteration seeded on one branch may converge on the other.

The criterion adopted instead is continuity in the complex plane. At each step the two possible assignments are compared by the total displacement they imply with respect to the previous pair, and the one with the smaller displacement is retained.

```
def track_two_branches(l1_raw, l2_raw):
    """
    Assign two complex eigenvalues to continuous
       branches. Ordering by real
    part fails where the real parts cross, so the
       assignment is chosen to
    minimize the total displacement from the previous
       step.
    """
    l1_tracked = np.zeros_like(l1_raw, dtype=complex)
    l2_tracked = np.zeros_like(l2_raw, dtype=complex)

    prev_ev = None
    for i in range(len(l1_raw)):
        e1, e2 = l1_raw[i], l2_raw[i]

        if prev_ev is None:
            # First point: order by real part to fix
               the convention.
            if np.real(e1) < np.real(e2):
                l1_tracked[i], l2_tracked[i] = e1, e2
            else:
                l1_tracked[i], l2_tracked[i] = e2, e1
        else:
            d_same = np.abs(e1 - prev_ev[0]) + np.abs(
               e2 - prev_ev[1])
            d_swap = np.abs(e2 - prev_ev[0]) + np.abs(
               e1 - prev_ev[1])
            if d_same < d_swap:
                l1_tracked[i], l2_tracked[i] = e1, e2
            else:
                l1_tracked[i], l2_tracked[i] = e2, e1

        prev_ev = [l1_tracked[i], l2_tracked[i]]

    return l1_tracked, l2_tracked
```

Listing B.8: Branch labeling by minimum displacement in the complex plane.

The same routine is applied to the numerical data and to the model eigenvalues during the fit. (In the model comparison of Table 4.2, where the real parts anticross over the whole window, the data are simply ordered by real

part, which is equivalent.) This is required: the residual is formed by subtracting the model from the data branch by branch, so if the two were labeled by different criteria the residual would contain a spurious discontinuity wherever the conventions disagreed, and the fit would attempt to absorb it into the parameters. Applying the identical criterion on both sides guarantees that the comparison is made between corresponding branches.

The criterion is local, and it fails if the sampling in k_x is coarse enough that a branch moves further between two adjacent points than the separation between the branches. The grids of Section B.8 were chosen to keep this condition satisfied throughout the fitted window.

B.6 Hamiltonian Fit and Model Selection

The fit compares four real quantities at each wavevector: the real and imaginary parts of the two eigenvalues. These are concatenated into a single target vector, so that a single call to `curve_fit` minimizes the residual of all four simultaneously.

Before fitting, all frequencies are divided by $W_{\mathrm{scale}} = 10^{15}$ rad/s. Rescaling is needed because the parameters of the model differ by fifteen orders of magnitude, from $\omega_0 \sim 10^{15}$ to dimensionless slopes of order unity, and the trust-region reflective algorithm, which `curve_fit` uses when parameter bounds are given, estimates the Jacobian by finite differences using a step tied to the parameter values. Without rescaling the step appropriate to ω_0 is meaningless for s_1, and the fit either fails to move the small parameters or reports a covariance matrix dominated by the scaling.

```
def selected_gap_leaky_model(kx_c_scaled, *theta,
                             free_names=None,
                                fixed_values=None):
    """
    Model function passed to curve_fit. Free parameters
        arrive positionally
    in theta and are merged with the constrained ones;
       the eigenvalues are
    computed, assigned to branches, and returned as a
       single real vector.
    """
    params = dict(fixed_values)
    for name, value in zip(free_names, theta):
        params[name] = value

    l1_raw, l2_raw = hamiltonian_eigenvalues(
        kx_c_scaled * W_SCALE,
```

```
        params["w0"] * W_SCALE, params["s1"], params["
            s2"],
        params["g0"] * W_SCALE, params["g1"],
        params["gamma01"] * W_SCALE, params["gamma1"],
        params["gamma02"] * W_SCALE, params["gamma2"],
        params["kref_c"] * W_SCALE, alpha=params["alpha
            "])

    # Same tracking criterion applied to the data, so
        that model and data
    # branches correspond.
    l1_tracked, l2_tracked = track_two_branches(l1_raw,
        l2_raw)

    return np.concatenate([
        np.real(l1_tracked), np.imag(l1_tracked),
        np.real(l2_tracked), np.imag(l2_tracked)
    ]) / W_SCALE
```

Listing B.9: Model function for the fit: parameters are rescaled, eigenvalues computed and tracked, then flattened into a single real vector.

The same fitting function is used for all regime-dependent parametrizations. The different models are obtained by changing which Hamiltonian parameters are treated as free and which are constrained, so that the same least-squares procedure can be applied consistently to all cases.

Within the range of the model $+g_1$, α, each fit is initialized with the parameters obtained at the previous gap. Beyond d_1 the chain is interrupted after the first reduced fit, and each subsequent fit starts from values estimated from the data at that gap, with $\alpha = +0.02$ for the α-only fits. The coherent coupling g_0 is bounded to be non-negative, which fixes the relative phase of the two modes: the sign of α is therefore defined relative to that of g_0 (Section 4.3.3). The dissipative coupling is bounded by $|\alpha| \leq 0.9$. When q_{ref} is left free, the residual has several local minima, one of them at the edge of the fitted window; those fits were therefore repeated from several starting values of q_{ref}, and the lowest residual is reported.

```
def impose_mode_convention(params, errs):
    """
    The fit is symmetric under exchange of the two
        modes, so a convention is
    imposed afterwards: index 1 is the branch with the
        larger real slope.
    """
    if params["s1"] < params["s2"]:
        params, errs = params.copy(), errs.copy()
        params["s1"], params["s2"] = params["s2"],
```

```
            params["s1"]
        params["gamma01"], params["gamma02"] = (params[
            "gamma02"],
                                                params[
                                                    "
                                                    gamma01
                                                    "])
        params["gamma1"], params["gamma2"] = (params["
            gamma2"],
                                              params["
                                                  gamma1
                                                  "])
        errs["s1"], errs["s2"] = errs.get("s2", 0.0),
            errs.get("s1", 0.0)
        errs["gamma01"], errs["gamma02"] = (errs.get("
            gamma02", 0.0),
                                            errs.get("
                                                gamma01"
                                                , 0.0))
        errs["gamma1"], errs["gamma2"] = (errs.get("
            gamma2", 0.0),
                                          errs.get("
                                              gamma1",
                                              0.0))
    return params, errs
```

Listing B.10: Mode labeling convention applied after the fit.

The fitted parameters, their uncertainties and the residual are written to an `.out` file with one row per gap thickness, which is the input to the analysis of the following section.

B.7 Exceptional Point Search

The exceptional point analysis of Section 4.4 operates entirely on the fitted parameters, and requires no further evaluation of the transfer matrix. From each row of the fit file the four real quantities of Eq. (4.11) are reconstructed at an arbitrary detuning Δq, and from them the discriminant.

The system of Eq. (4.14) is solved in two stages rather than as a two-dimensional root search, which exploits the structure of the problem: at fixed gap, $\mathrm{Im}(D)$ is a smooth one-variable function of Δq, so its zero can be bracketed and refined reliably, and the remaining condition becomes one-dimensional along the resulting curve.

```
def solve_ImD_zero(p, dk_range=1e14, n_scan=2001):
    """
    At fixed gap, find the detuning that cancels Im(D). A coarse scan
    brackets the sign changes and brentq refines them. The brentq solver preserves the bracket, unlike an unbracketed Newton iteration.

    Several roots may exist. The current implementation retains the root closest to \Delta q=0. Over the investigated range, this root remains on the branch connected to the reference solution. The search range is restricted to the interval where the linear
    parametrization of the Hamiltonian remains valid.
    """
    xs = np.linspace(-dk_range, dk_range, n_scan)
    ys = np.array([discriminant(p, x).imag for x in xs])

    sign_changes = np.where(np.diff(np.sign(ys)) != 0)[0]
    if len(sign_changes) == 0:
        return None

    roots = [brentq(lambda x: discriminant(p, x).imag, xs[k], xs[k + 1])
             for k in sign_changes]
    return roots[int(np.argmin(np.abs(roots)))]
```

Listing B.11: Solution of $\mathrm{Im}(D) = 0$ at fixed gap, on the branch continuously connected to the reference point.

The restriction of the search to $|\Delta q| \leq 10^{14}$ rad/s follows from the validity of the linearization. Outside that interval the linearization of Eqs. (4.3)–(4.5) is no longer justified, and at the largest gaps the term $g_1 \Delta q$ would exceed g_0 and reverse the sign of the coherent coupling, which has no physical meaning.

The exceptional point is then located by scanning $\mathrm{Re}(D)$ along the curve just constructed and interpolating its sign change. The transversality of the intersection is verified by evaluating the Jacobian of $(\mathrm{Re}\, D, \mathrm{Im}\, D)$ with respect to $(d, \Delta q)$ by finite differences. This last check requires attention to units: d is measured in nanometers and Δq in rad/s, so the two columns of the Jacobian differ by twelve orders of magnitude, and the normalized determinant evaluates to $\sim 10^{-12}$ regardless of the geometry. Non-dimensionalizing both variables with the scales of the problem before forming the determinant removes the artifact and returns the value quoted in Table 4.5.

B.8 Numerical Parameters

Table B.1 collects the tolerances, step sizes and grids used to produce the results of Chapters 3 and 4. The calculations were performed in Python using NumPy, SciPy and Matplotlib. The parameter bounds and numerical tolerances listed below refer to the gap-sweep fits unless explicitly stated otherwise. The bound $|\alpha| \leq 0.999$ was used for the single-configuration model-comparison fits of Table 4.2, whereas the gap-sweep fits used the tighter bound ($|\alpha| \leq 0.9$).

Stage	Parameter	Value
Transfer matrix	Overflow guard on $\lvert\mathrm{Re}(ik_z d)\rvert$	500
	Sentinel matrix entries	10^{50}
Guided search	Points in the coarse scan	1000
	Peak prominence	10^{-5} (10^{-6} for $k_x > 2\times10^7$ rad/m)
	Minimum peak separation	8 points
	Bracket half-width	$0.01\,\omega$
		clipped to $[5\times10^{12}, 10^{14}]$ rad/s
	Accepted bracket minimum	$\lvert T_{22}\rvert < 10^{-3}$ (10^{-2} near light line)
	Secant tolerance	10^{-7} rad/s (absolute)
	Maximum iterations	100
	Root merging threshold	$10^{-4}\,\omega_{\max}$
	Seed merging before the secant	10^{11} rad/s
	Accepted secant root	$\lvert T_{22}\rvert < 0.1$ (0.5 for $k_x > 2\times10^7$ rad/m)
	Fallback minimization	$\pm5\times10^{13}$ rad/s, accepted if $\lvert T_{22}\rvert < 0.1$
Leaky search	Finite-difference step	$\max(10^{-12}, 10^{-8}\lvert\omega\rvert)$ rad/s
	Residual tolerance	$\lvert T_{22}\rvert < 10^{-8}$
	Increment tolerance	10^{-6} rad/s (never reached)
	Maximum iterations	50
	Seed displacement	$10^{-2}\times$ distance from the light line
	Seed acceptance window	15% from the light line
	Continuation guesses	$\{1, 0.9, 0.75, 0.5\}\times\tilde{\omega}_{\mathrm{prev}}$
		$\mathrm{Re}\,\tilde{\omega}_{\mathrm{prev}} - 10^{14}\,i$ rad/s
	Loss filter	$\lvert\mathrm{Im}\,\tilde{\omega}\rvert < 10\,\lvert\mathrm{Re}\,\tilde{\omega}\rvert$
	Root merging threshold	10^{-4} (relative)
Wavevector grids	Global sweep	100 points, 10^5–3×10^7 rad/m
	Leaky fit, gap sweep	80 points, 0.4–0.7×10^7 rad/m
	Leaky fit, $d = 600$ nm	19 points, 4.0–6.37×10^6 rad/m
	Guided fit, $d = 200$ nm	20 points, 0.9–1.4×10^7 rad/m
	Guided fit, gap sweep	global grid, 17 points in
		0.9–1.4×10^7 rad/m
Pair selection	$\mathrm{Re}\,\tilde{\omega}$, $d = 600$ nm	$[1.0, 2.0]\times10^{15}$ rad/s
	$\mathrm{Im}\,\tilde{\omega}$, $d = 600$ nm	$[-1.5, -0.2]\times10^{14}$ rad/s
	$\mathrm{Re}\,\tilde{\omega}$, gap sweep	$[1.2, 1.5]\times10^{15}$ rad/s
	ω, guided fits	$[1.5, 2.2]\times10^{15}$ rad/s

Stage	Parameter	Value
Fit	Frequency scaling W_{scale}	10^{15} rad/s
	Algorithm	trust-region reflective
	Bounds	$g_0 \geq 0$; $\lvert\alpha\rvert \leq 0.9$ (0.999 in Table 4.2)
	Max. function evaluations	10^5
	Initial α, α-only fits	+0.02
	Starts for free q_{ref}	13, evenly spaced
EP search	Detuning search range	$\lvert\Delta q\rvert \leq 10^{14}$ rad/s
	Points in the Δq scan	2001
	Gap grid for interpolation	3000 points
	Monte Carlo realizations	400 (random seed 11)

Table B.1: Tolerances, step sizes and grids used throughout the calculations. Where a parameter is wavevector-dependent, both values are given.

Appendix C

Fits of the Hamiltonian Models Compared in Chapter 4

This appendix collects the complete fit curves for the Hamiltonian models compared in Table 4.2 of Chapter 4. All fits are performed for the representative separation $d = 600$ nm over the same wavevector interval and using the same residual definition. The models differ only in which of the parameters g_1, α, and q_{ref} are released as additional free parameters.

The purpose of this appendix is to provide a visual comparison of the model predictions with the TMM eigenfrequencies. In each figure, the left panel shows the real parts of the two eigenfrequencies and the right panel shows their imaginary parts. Open circles denote the TMM results, while the solid curves are the eigenvalues of the corresponding fitted effective Hamiltonian. The model curves are colored according to the Core 1 weight of the associated right eigenvector, using the same convention as in Chapter 4.

C.1 Fit Curves at $d = 600$ nm

The eight compared parametrizations are shown below in the same order as Table 4.2: the baseline model, the models with g_1, α, or q_{ref} released individually, and the four corresponding two- and three-parameter extensions.

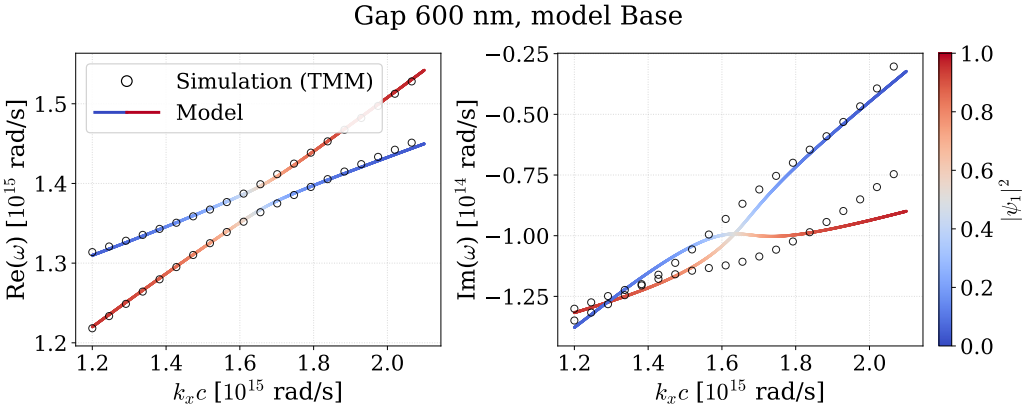


Figure C.1: Fit of the baseline Hamiltonian at $d = 600$ nm. Open circles: TMM eigenfrequencies. Lines: eigenvalues of the fitted model. Left: real parts; right: imaginary parts. The model contains only the constant coherent coupling g_0. The normalized RMS residual is $\chi = 0.217$.

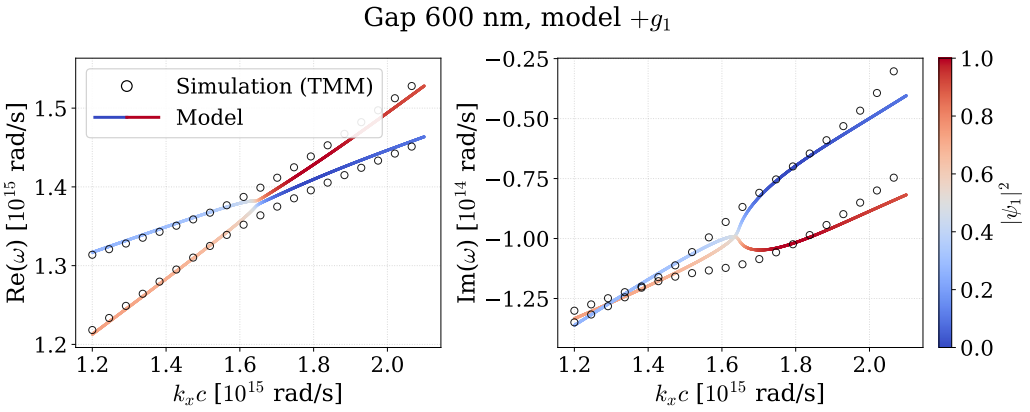


Figure C.2: Fit of the Hamiltonian with wavevector-dependent coherent coupling ($+g_1$) at $d = 600$ nm. The normalized RMS residual is $\chi = 0.195$.

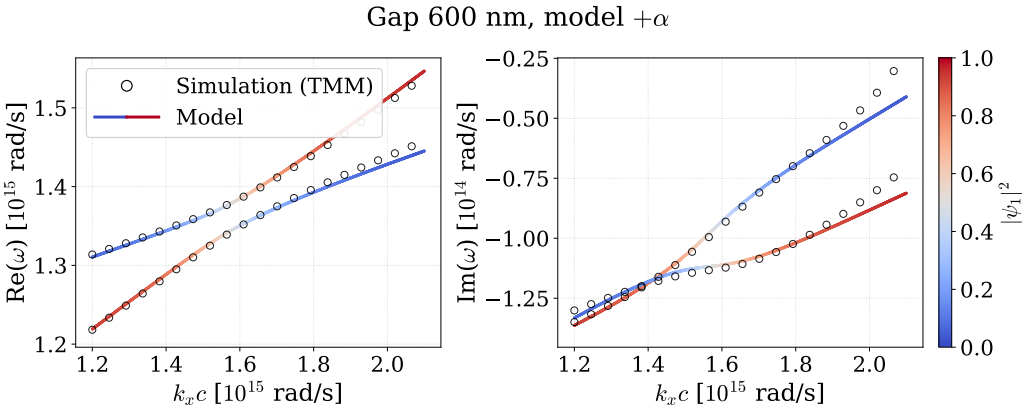


Figure C.3: Fit of the Hamiltonian with dissipative coupling ($+\alpha$) at d = 600 nm. The normalized RMS residual is $\chi = 0.060$.

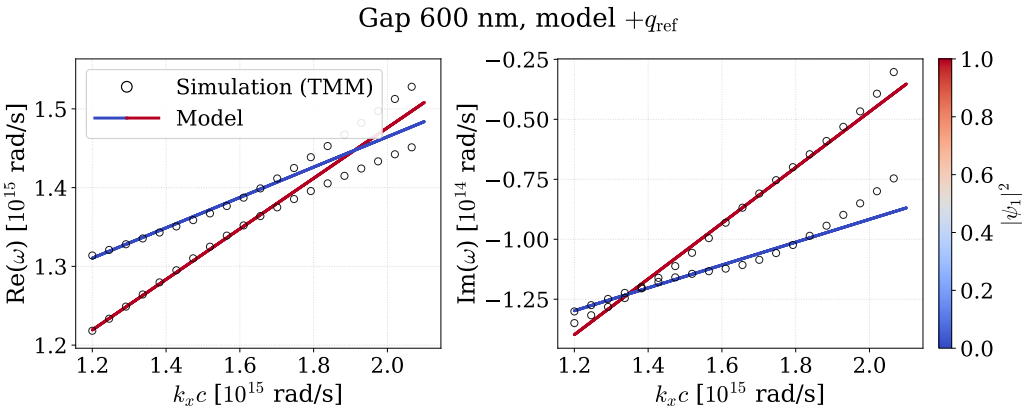


Figure C.4: Fit of the Hamiltonian with free reference wavevector ($+q_{\mathrm{ref}}$) at $d = 600$ nm. The normalized RMS residual is $\chi = 0.090$.

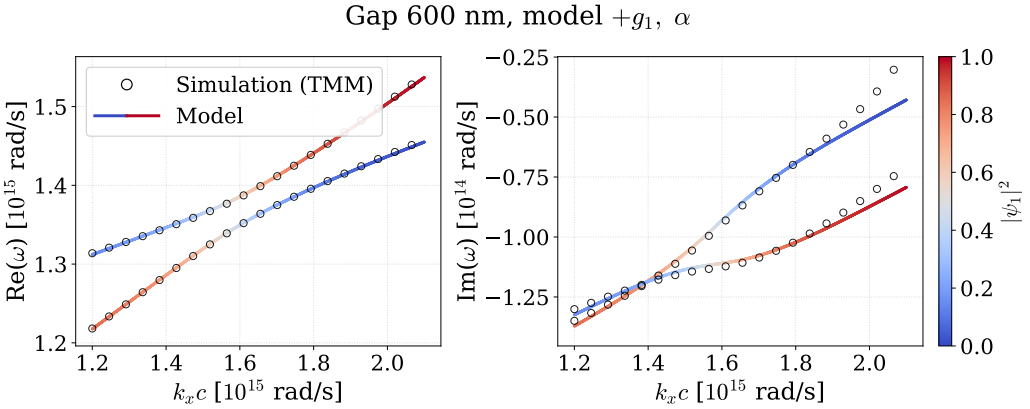


Figure C.5: Fit of the adopted ten-parameter Hamiltonian with wavevector-dependent coherent coupling and dissipative coupling ($+g_1,\ \alpha$) at $d = 600$ nm. The normalized RMS residual is $\chi = 0.047$.

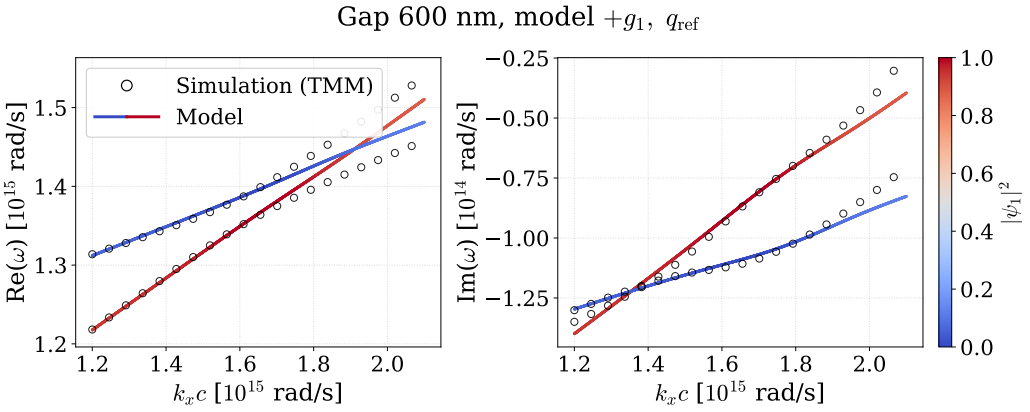


Figure C.6: Fit of the Hamiltonian with wavevector-dependent coherent coupling and free reference wavevector ($+g_1,\ q_{\mathrm{ref}}$) at $d = 600$ nm. The normalized RMS residual is $\chi = 0.047$.

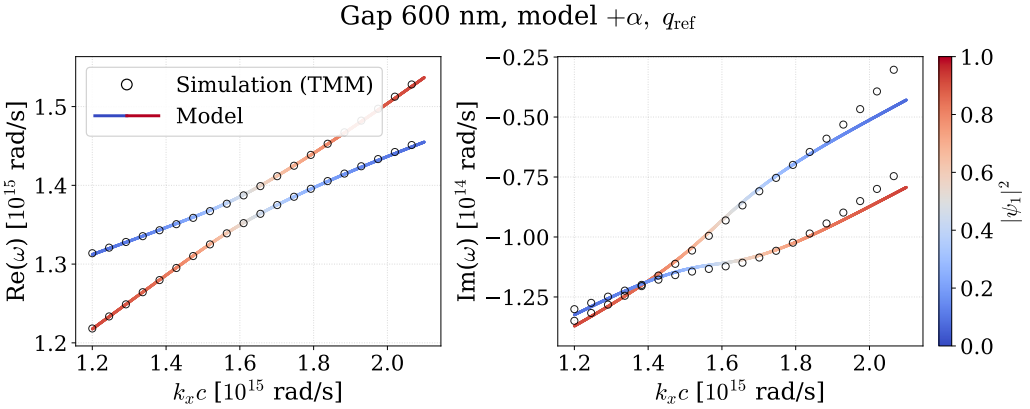


Figure C.7: Fit of the Hamiltonian with dissipative coupling and free reference wavevector ($+\alpha,\ q_{\mathrm{ref}}$) at $d = 600$ nm. The normalized RMS residual is $\chi = 0.047$.

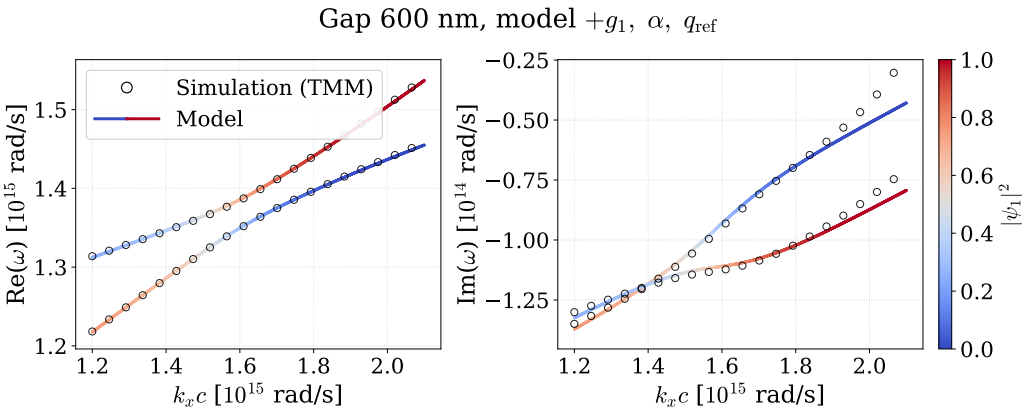


Figure C.8: Fit of the Hamiltonian with wavevector-dependent coherent coupling, dissipative coupling, and free reference wavevector ($+g_1,\ \alpha,\ q_{\mathrm{ref}}$) at $d = 600$ nm. The normalized RMS residual is $\chi = 0.047$.

Bibliography

[1] Ramy El-Ganainy, Konstantinos G. Makris, Mercedeh Khajavikhan, Ziad H. Musslimani, Stefan Rotter, and Demetrios N. Christodoulides. Non-Hermitian physics and $\mathscr{P}\mathscr{T}$ symmetry. *Nature Physics*, 14(1):11–19, 2018.

[2] Liang Feng, Ramy El-Ganainy, and Li Ge. Non-Hermitian photonics based on parity–time symmetry. *Nature Photonics*, 11(12):752–762, 2017.

[3] Ş. K. Özdemir, S. Rotter, F. Nori, and L. Yang. Parity–time symmetry and exceptional points in photonics. *Nature Materials*, 18(8):783–798, 2019.

[4] Carl M. Bender and Stefan Boettcher. Real spectra in non-Hermitian Hamiltonians having $\mathscr{P}\mathscr{T}$ symmetry. *Physical Review Letters*, 80(24):5243–5246, 1998.

[5] K. G. Makris, R. El-Ganainy, D. N. Christodoulides, and Z. H. Musslimani. Beam dynamics in $\mathscr{P}\mathscr{T}$ symmetric optical lattices. *Physical Review Letters*, 100(10):103904, 2008.

[6] A. Guo, G. J. Salamo, D. Duchesne, R. Morandotti, M. Volatier-Ravat, V. Aimez, G. A. Siviloglou, and D. N. Christodoulides. Observation of $\mathscr{P}\mathscr{T}$-symmetry breaking in complex optical potentials. *Physical Review Letters*, 103(9):093902, 2009.

[7] Christian E. Rüter, Konstantinos G. Makris, Ramy El-Ganainy, Demetrios N. Christodoulides, Mordechai Segev, and Detlef Kip. Observation of parity–time symmetry in optics. *Nature Physics*, 6(3):192–195, 2010.

[8] Zin Lin, Hamidreza Ramezani, Toni Eichelkraut, Tsampikos Kottos, Hui Cao, and Demetrios N. Christodoulides. Unidirectional invisibility induced by $\mathscr{P}\mathscr{T}$-symmetric periodic structures. *Physical Review Letters*, 106(21):213901, 2011.

[9] Liang Feng, Zi Jing Wong, Ren-Min Ma, Yuan Wang, and Xiang Zhang. Single-mode laser by parity-time symmetry breaking. *Science*, 346(6212):972–975, 2014.

[10] Hossein Hodaei, Mohammad-Ali Miri, Matthias Heinrich, Demetrios N. Christodoulides, and Mercedeh Khajavikhan. Parity-time–symmetric microring lasers. *Science*, 346(6212):975–978, 2014.

[11] Bo Peng, Şahin Kaya Özdemir, Fuchuan Lei, Faraz Monifi, Mariagiovanna Gianfreda, Gui Lu Long, Shanhui Fan, Franco Nori, Carl M. Bender, and Lan Yang. Parity–time-symmetric whispering-gallery microcavities. *Nature Physics*, 10(5):394–398, 2014.

[12] Tosio Kato. *Perturbation Theory for Linear Operators*. Springer-Verlag, Berlin, 1966.

[13] M. V. Berry. Physics of nonhermitian degeneracies. *Czechoslovak Journal of Physics*, 54(10):1039–1047, 2004.

[14] W. D. Heiss. The physics of exceptional points. *Journal of Physics A: Mathematical and Theoretical*, 45(44):444016, 2012.

[15] Jan Wiersig. Enhancing the sensitivity of frequency and energy splitting detection by using exceptional points: Application to microcavity sensors for single-particle detection. *Physical Review Letters*, 112(20):203901, 2014.

[16] Hossein Hodaei, Absar U. Hassan, Steffen Wittek, Hipolito Garcia-Gracia, Ramy El-Ganainy, Demetrios N. Christodoulides, and Mercedeh Khajavikhan. Enhanced sensitivity at higher-order exceptional points. *Nature*, 548(7666):187–191, 2017.

[17] Weijian Chen, Şahin Kaya Özdemir, Guangming Zhao, Jan Wiersig, and Lan Yang. Exceptional points enhance sensing in an optical microcavity. *Nature*, 548(7666):192–196, 2017.

[18] C. Dembowski, H.-D. Gräf, H. L. Harney, A. Heine, W. D. Heiss, H. Rehfeld, and A. Richter. Experimental observation of the topological structure of exceptional points. *Physical Review Letters*, 86(5):787–790, 2001.

[19] Jörg Doppler, Alexei A. Mailybaev, Julian Böhm, Ulrich Kuhl, Adrian Girschik, Florian Libisch, Thomas J. Milburn, Peter Rabl, Nimrod Moiseyev, and Stefan Rotter. Dynamically encircling an exceptional point for asymmetric mode switching. *Nature*, 537(7618):76–79, 2016.

[20] H. Xu, D. Mason, Luyao Jiang, and J. G. E. Harris. Topological energy transfer in an optomechanical system with exceptional points. *Nature*, 537(7618):80–83, 2016.

[21] Mohammad-Ali Miri and Andrea Alù. Exceptional points in optics and photonics. *Science*, 363(6422):eaar7709, 2019.

[22] Midya Parto, Yuzhou G. N. Liu, Babak Bahari, Mercedeh Khajavikhan, and Demetrios N. Christodoulides. Non-Hermitian and topological photonics: optics at an exceptional point. *Nanophotonics*, 10(1):403–423, 2021.

[23] Philippe Lalanne, Wei Yan, Kevin Vynck, Christophe Sauvan, and Jean-Paul Hugonin. Light interaction with photonic and plasmonic resonances. *Laser & Photonics Reviews*, 12(5):1700113, 2018.

[24] C. Sauvan, J. P. Hugonin, I. S. Maksymov, and P. Lalanne. Theory of the spontaneous optical emission of nanosize photonic and plasmon resonators. *Physical Review Letters*, 110(23):237401, 2013.

[25] H. Friedrich and D. Wintgen. Interfering resonances and bound states in the continuum. *Physical Review A*, 32(6):3231–3242, 1985.

[26] Chia Wei Hsu, Bo Zhen, A. Douglas Stone, John D. Joannopoulos, and Marin Soljačić. Bound states in the continuum. *Nature Reviews Materials*, 1:16048, 2016.

[27] Bo Zhen, Chia Wei Hsu, Yuichi Igarashi, Ling Lu, Ido Kaminer, Adi Pick, Song-Liang Chua, John D. Joannopoulos, and Marin Soljačić. Spawning rings of exceptional points out of Dirac cones. *Nature*, 525(7569):354–358, 2015.

[28] S. N. Ghosh and Y. D. Chong. Exceptional points and asymmetric mode conversion in quasi-guided dual-mode optical waveguides. *Scientific Reports*, 6:19837, 2016.

[29] Shamkhal Hasanli, Mehedi Hasan, Hyejin Yoon, Seungyong Lee, and Sangsik Kim. Exceptional points in a passive strip waveguide. *Nanophotonics*, 14(8):1301–1309, 2025.

[30] Bahaa E. A. Saleh and Malvin Carl Teich. *Fundamentals of Photonics*. John Wiley & Sons, 3rd edition, 2019.

[31] Amnon Yariv and Pochi Yeh. *Photonics: Optical Electronics in Modern Communications*. Oxford University Press, 6th edition, 2007.

[32] Allan W. Snyder and John D. Love. *Optical Waveguide Theory*. Chapman and Hall, 1983.

[33] Wonjoo Suh, Zheng Wang, and Shanhui Fan. Temporal coupled-mode theory and the presence of non-orthogonal modes in lossless multimode cavities. *IEEE Journal of Quantum Electronics*, 40(10):1511–1518, 2004.

[34] P. Hu, J. Wang, Q. Jiang, J. Wang, L. Shi, D. Han, Z. Q. Zhang, C. T. Chan, and J. Zi. Global phase diagram of bound states in the continuum. *Optica*, 9(12):1353–1361, 2022.

[35] Lucio Claudio Andreani, Giovanna Panzarini, and Jean-Michel Gérard. Strong-coupling regime for quantum boxes in pillar microcavities: Theory. *Physical Review B*, 60(19):13276–13279, 1999.

[36] Jonathan Hu and Curtis R. Menyuk. Understanding leaky modes: slab waveguide revisited. *Advances in Optics and Photonics*, 1(1):58–106, 2009.

[37] Ingrid Rotter. A non-Hermitian Hamilton operator and the physics of open quantum systems. *Journal of Physics A: Mathematical and Theoretical*, 42(15):153001, 2009.

[38] Jan Wiersig. Petermann factors and phase rigidities near exceptional points. *Physical Review Research*, 5(3):033042, 2023.

[39] Benoit Nennig and Emmanuel Perrey-Debain. A high order continuation method to locate exceptional points and to compute Puiseux series with applications to acoustic waveguides. *Journal of Computational Physics*, 412:109425, 2020.

[40] C. R. Harris et al. Array programming with NumPy. *Nature*, 585:357–362, 2020.

[41] P. Virtanen et al. SciPy 1.0: fundamental algorithms for scientific computing in Python. *Nature Methods*, 17:261–272, 2020.

[42] J. D. Hunter. Matplotlib: A 2D graphics environment. *Computing in Science & Engineering*, 9(3):90–95, 2007.

Ringraziamenti

Desidero ringraziare il mio relatore, Prof. Lucio Andreani, per la disponibilità e per l'attenzione con cui mi ha guidata in questo periodo di ricerca. I suoi suggerimenti e il suo metodo di lavoro sono stati fondamentali per la realizzazione di questa tesi.

Grazie alla mia famiglia, in particolare a mia mamma, a mio fratello e a mia nonna, per avermi permesso di arrivare fin qui e per avermi sostenuta in questi anni di studio.

Grazie a chi ha condiviso con me questi anni: ai miei amici, ai compagni di corso e a tutti coloro che ho incontrato durante questo percorso.